Fall 2019

Electrohydrodynamic Simulations of the Deformation of Liquid-Filled Capsules

Pai Song
Old Dominion University, psong002@odu.edu

Recommended Citation

Song, Pai. "Electrohydrodynamic Simulations of the Deformation of Liquid-Filled Capsules" (2019). Doctor of Philosophy (PhD), Dissertation, Mathematics and Statistics, Old Dominion University, DOI: 10.25777/86e9-4q47
https://digitalcommons.odu.edu/mathstat_etds/112

ELECTROHYDRODYNAMIC SIMULATIONS OF THE DEFORMATION OF LIQUID-FILLED CAPSULES

by

Pai Song
B.E. July 2006, Beihang University, China
M.A. May 2011, Marshall University

A Dissertation Submitted to the Faculty of
Old Dominion University in Partial Fulfillment of the
Requirements for the Degree of

DOCTOR OF PHILOSOPHY

COMPUTATIONAL AND APPLIED MATHEMATICS

OLD DOMINION UNIVERSITY
December 2019

Approved by:

Yan Peng (Director)

Richard D. Noren (Member)

Ruhai Zhou (Member)

Xiaoyu Zhang (Member)

ABSTRACT

ELECTROHYDRODYNAMIC SIMULATIONS OF THE DEFORMATION OF LIQUID-FILLED CAPSULES

Pai Song
Old Dominion University, 2019
Director: Dr. Yan Peng

A comprehensive two- and three- dimensional framework for the electrohydrodynamic simulation of deformable capsules is provided. The role of a direct current (DC) electric field on the deformation and orientation of a liquid-filled capsule is thoroughly considered numerically. This framework is based on lattice Boltzmann method for the fluid, finite element method for the membrane structure of the capsule, fast immersed interface method for the electric field and immersed boundary method being used to consider the fluid-structure-electric interaction. Under the effect of electric field, two different types of equilibrium states, prolate or oblate are obtained. The numerical algorithm is also applied to study the interfacial tension droplet and red blood cell under shear flow. The capsules are more deformed and arrive at equilibrium status more quickly under stronger electric field. Bending stiffness will suppress the deformation and cause transition from tank-treading to tumbling for the red blood cell. However, the applied electric field will slow down the transition from tank-treading to the tumbling motion or even stay in the tank-treading motion with stronger electric field.

ACKNOWLEDGEMENTS

I wish to express my sincere gratitude and appreciation to my advisor Dr. Yan Peng for her constant encouragement, immense knowledge, invaluable guidance and advice throughout my Ph.D. study and research work. She was available promptly and gave great suggestions whenever I struggled in my projects. I am also very much obliged to my committee members, Dr. Richard D. Noren, Dr. Ruhai Zhou and Dr. Shizhi Qian for their support, guidance and helpful suggestions. Many sincere thanks also go to Dr. John Adam for his help and encouragement during my job hunting, and being my mentor and guiding me on the right path. I also owe particular debts of gratitude to Dr. Hideaki Kaneko, for his valuable time and helpful suggestions on my learning, teaching and job searching. I would also like to thank our former Graduate Program Director Dr. Raymond Cheng for his always helpful advises and support over the course of years; to Dr. Yaohang Li, his concern and support on my study and my family; to Dr. Zhilin Li, from North Carolina State University, his significant help and advises on my research.

I appreciate the assistance and kindness from my classmates and from many ohter faculty and staff members of our Department. I am thankful to the Department of Mathematics and Statistics for providing me with resources to succeed in my academic pursuit of excellence. I would like to thank our department and the Modeling and Simulation Program from MSVE department for their financial support.

My special thanks goes to my loving wife Yuan Liu for her constant support and encouragement during the years. This dissertation would not have been possible without her support; to my kids, Leroy, Anna and Logan, I wish to be a good model for them. Special thanks also go to my best friends Dr. Wei Li, Dr. Weidong Li, their numerous suggestions and help during the time we've been together at ODU; to Dr. Jiacheng Cai, his helpful suggestion and assistant on my job hunting.

TABLE OF CONTENTS

LIST OF TABLES

LIST OF FIGURES

CHAPTER 1

INTRODUCTION AND BACKGROUND

1.1 INTRODUCTION

The study of the shape deformation of viscoelastic, fluid-filled capsules has many industrial applications in hydrodynamics. In particular, it has been known that the deformability of red blood cell is associated with its health status [1]. The membrane of a red blood cell has two components, the cytoskeleton on the cytosolic side (internal) and a lipid bilayer on the external side [2]. Small capillaries requires significant deformation by red blood cells, from the normal biconcave discoid to a bullet-like shape [3]. Some blood diseases are related to the ability of red blood cells to deform or recover their shapes, such as sickle-cell anemia. For health red blood cells, the cytoskeleton is closely attached to the lipid bilayer; while detached from lipid bilayer, it maybe a signal of sickle-cell anemia. The dissociated membrane may result in less deformation. But when red blood cell pass through which requires it to deform to a bullet-like shape, it undergoes significant deformation. Better knowledge of the mechanics underlying red blood cell shape deformation would be of use in understanding how they are distorted by sickle cell anemia and how this distortion might be counted by treatment [4].

To aid the development of diagnosis and treatments for the blood diseases, such as develop a practical lab-on-a-chip device capable of red blood cell diagnosis in clinical applications, it is important to understand the mechanical structure of red blood cell and study the manner in which their shape is deformed. Extensive theoretical analysis [5, 6, 7] and experimental studies [8, 9, 10] has been recently complemented by significant computational simulations [3, 11, 12]. Up till now, very few attentions have been paid to the red blood cell deformation in electrokinetic based microfluidic environment. A blood cell type-membrane is elastic, area preserved; a complete understanding of such membrane behaviour involves fluid-structure interaction under the influence of electric field is still lacking.

In this thesis, to better understand the mechanism of deformation of red blood cell type capsule, we also consider the simulation of a droplet, which would be used to validate our numerical method and compared with red blood cell deformation. Depending on the assumptions pertaining to the physical properties of the membrane, a capsule may serve as a model for various types of particles. For example, the capsule is considered to be an interfacial- tension drop if the membrane is a simple liquid-liquid interface, and the membrane may be also a thin deformable solid. G.I. Taylor [13] studied a weakly conducting drop suspended in another leaky dielectric fluid under an electric field, and concluded that the equilibrium drop shape can be explained by balancing the viscous stress with the electric stress on the drop interface, in which electric conductivity and permittivity between the two fluids were considered. Jong-Wook Ha [14] analyzed the effect of uniform electric field on the orientation and deformation of the a red blood cell-type capsule with a viscoelastic membrane theoretically in the small deformation limit. It shows when the capsule immersed in a simple shear flow, the surface viscosity affects the degree of deformation. The effect of electric field on the orientation angle of the capsule is considerable.

There has been quite a few effort in using numerical methods to simulate the electrohydrodynamics of a viscous capsule under an DC electric field. Numerous extensive studies have been published on the simulation of capsule deformation under leaky dielectric theory. Those works, based on how the interface is treated, can be categorized into the front tracking method [15], level set method [16, 17], lattice Boltzmann method [18] and the volume-of-fluid method [19], etc... In [20], a hybrid immersed boundary and immersed interface method is developed to simulate the dynamics of a leaky dielectric drop under an DC electric field in Navier-Stocks fluids.

In present work, we investigate the eletrohydrodynamics of interfacial-tension drop, viscoelastic circular membrane and red blood cell shape capsule under electric field. A lattice Boltzmann method is used to solve the fluid flow, while the immersed boundary method is chosen to simulate the fluid-structure interaction which take into account various type of capsule's properties. In addition, the electric field is solved by fast immersed interface method. As in [20], the resulting Maxwell stress tensor due to applied electric field is cast as an interfacial electric force, so the fluid force and electric interfacial force can be formulated in a unified immersed boundary framework.

1.2 SCOPE AND OUTLINE

This thesis has four principal aims. First, it will develop a comprehensive, extensible computational model of electrohydrodynamic simulation for interfacial-tension droplet and viscoelastic capsules. Second, it will show how the capsule deform in electric field induced flow or under both shear flow and electric field. It would be observed the role that the capsule's shape and parameters play in these processes. This will help to reconcile work that largely focused on experimental investigations. Third, it will consider the potential mechanical causes of a red blood cells' biconcave shape. Biological and theoretical studies have proposed several ideas, and the perspective of a computational study would be of interest.

In Chapter 2, a numerical method for modeling and simulation of leaky dielectric model is outlined. A comparison was made between Correction Function Method [21] and Fast Immersed Interface Method [22] when choose the algorithm for the computation of electric potential. The Fast Immersed Interface Method is selected due to the advantage to impose the jump conditions at the interface and the ability to deal with three dimensional computation.

In Chapter 3, a complete methodology for modeling and simulation of electrohydrodynamics is presented in two and three dimensional settings. Both the two and three dimensional versions of the structural model include the capsule's shear elasticity, bending stiffness, and membrane viscosity. The electric stress is cast as an interfacial electric force in which the shear force and electric interfacial tension can be formulated in a unified immersed boundary framework. It is significant important since the tensor is discontinuous across the interface due to different permittivities and conductivities in two different fluids.

In Chapter 4, a two dimensional validation of electrohydrodynamics for interfacial-tension drop is presented and the comparison with Taylor's small deformation theory is made. Numerical results are demonstrated by considering the combination of pemittivities and conductivities for three different cases. The results agree well with Taylor's theory. Numerical simulation is also performed when both shear flow and electric field are applied to the interfacial-tension drop. The results confirm deformation behaviors with other publications.

In Chapter 5, the electric effect on the deformation of immersed capsules is studied for two dimensional viscoelastic circular and biconcave (red blood cell) capsules in shear flow. Bending stiffness is considered and comparison is made for different bending modulus. Under electric effect, the capsule shows larger deformation. As electric field strength increases, slower tank-treading phenomenon is observed. The electric field could also slow or dump tumbling motion on a biconcave red blood cell in shear flow, numerical results are demonstrated.

In Chapter 6, the electric effect on the deformation of three-dimensional circular capsules is proposed. Some features of three dimensional simulation are similar to two dimensional results.

CHAPTER 2

ELECTRIC FIELD

2.1 GOVERNING EQUATIONS FOR ELECTRIC FIELD

In electrohydrodynamics, electric and magnetic phenomena are independent since their fields are uncoupled (Feynman et al 1964). Insofar as the characteristic time for electrostatic processes is large compared to that for magnetic phenomenon, the induced magnetic effect can be neglected. When external magnetic fields are absent, magnetic effects can be ignored completely. Thus, the electric field intensity $\mathbf{E}$ is irrotational which results in $\nabla \times \mathbf{E} = 0$. By Gauss law in a dielectric material with permittivity ε, the volume charge density q_v can be written as

$$q_v = \nabla \cdot (\varepsilon \mathbf{E}) \tag{1}$$

The conservation of free charge density in electrohydrodynamics can be expressed as

$$\frac{Dq_v}{Dt} + \nabla \cdot (\sigma \mathbf{E}) = 0 \tag{2}$$

where $\frac{D}{Dt} = \frac{\partial}{\partial t} + \mathbf{u} \cdot \nabla$ is the material derivative, σ is the electric conductivity of the medium and $\mathbf{u}$ is the velocity of the fluid. In a homogeneous incompressible fluid where the permittivity ε and conductivity σ are both constant and $\nabla \cdot \mathbf{u} = 0$. Plugging (1) into (2), and simplify we can have the differential equation for q_v

$$\frac{Dq_v}{Dt} + \frac{\sigma}{\varepsilon} q_v = 0 \tag{3}$$

The solution of (3) is simply $q_v = q_v^0 e^{-\sigma/\varepsilon \cdot t}$ with initial condition $q_v(0) = q_v^0$. We immediately find that the free charge density decays from the initial charge density with the relaxation time scale $t_E = \varepsilon/\sigma$. The viscous time scale of the fluid motion is defined by $t_F = \rho L^2/\mu$, where ρ and μ are fluid density and viscosity, and L is the characteristic length scale.

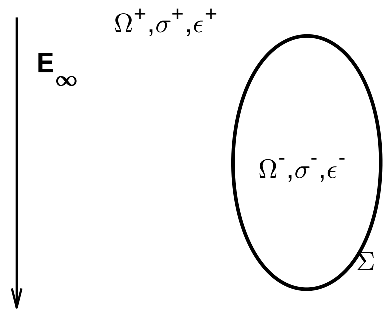

Figure. 1: A capsule suspended in a fluid subject to a uniform DC electric field $\mathbf{E}_\infty = (0, -E_\infty)$

For electrically conductive fluid satisfying the relation $t_E \ll t_F$, the charge accumulates at interface almost instantaneously as compared to the time scale of fluid motion. On the other hand, for the weakly conducting fluid, it may behave as a leaky dielectric material when $t_E \gg t_F$. There is no free electric charge in the leaky dielectric fluid system.

2.2 LEAKY DIELECTRIC MODEL

In a leaky dielectric model, both liquids in a two-fluid system with different electric properties are electrically conductive and satisfy the condition $t^E \ll t^v$, The governing equation of electric field can be simplified into

$$\nabla \cdot (\sigma \mathbf{E}) = 0 \quad \text{in} \quad \Omega \setminus \Sigma \tag{4}$$

We consider a capsule containing a leaky dielectric fluid suspended in another leaky dielectric fluid under a uniform DC electric field $\mathbf{E}_\infty$ as illustrated in Figure 1. The whole computational domain is separated by the elastic membrane Σ and the fluids are characterized by the piecewise constant of the electric conductivity σ and permittivity ε, where $-$ indicates quantities inside capsule and $+$ indicates quantities outside capsule.

By neglecting the induced magnetic effect, the electric field is irrotational. The electric field can be expressed in terms of electric potential ϕ by $\mathbf{E} = -\nabla\phi$. Then the governing equation of electric potential described by a Poisson equation can be written as

$$\nabla \cdot (\sigma \nabla \phi) = 0 \quad \text{in} \quad \Omega \backslash \Sigma \tag{5}$$

The boundary conditions along the interface separating Ω^- and Ω^+ are based on the continuity of the electric potential and the normal component of the electric flux density across the interface. The continuities of electric potential and electric current are preserved

$$[\phi] = 0 \quad \text{and} \quad [\sigma \nabla \phi \cdot \mathbf{n}] = 0 \quad \text{on} \quad \Sigma \tag{6}$$

where $[\cdot]$ indicates a jump of the quantity from the Ω^+ side minus the one of Ω^- side, and the normal vector $\mathbf{n}$ is pointing outward from Ω^- to Ω^+ side. The electric potential from (5) can be solved using the boundary conditions (6) on Σ and other boundary conditions on $\partial\Omega$ determined by suitable physical model. The electric field strength is computed by $\mathbf{E} = -\nabla\phi$. We can obtain the distribution of volume charge density $q_v = \nabla \cdot (\varepsilon \mathbf{E})$.

2.3 THE CORRECTION FUNCTION METHOD FOR SOLVING ELLIPTIC INTERFACE PROBLEM

This method is presented in two versions: 4^{th} order accuracy and 2^{nd} order accuracy [21]. To be consistent with fluid and structure solver, 2^{nd} order accuracy is adequate for current numerical simulation. In the case where conductivity is constant through the whole computational domain, $\sigma^+ = \sigma^- = \sigma$, without loss of generality, we consider the following elliptic interface problem with jumps as

$$\nabla^2 \phi^+ = \frac{f^+}{\sigma} \quad \text{in} \quad \Omega^+ \tag{7}$$

$$\nabla^2 \phi^- = \frac{f^-}{\sigma} \quad \text{in} \quad \Omega^- \tag{8}$$

$$[\phi] = a \quad \text{on} \quad \Sigma \tag{9}$$

$$[\nabla \phi \cdot \mathbf{n}] = \frac{b}{\sigma} \quad \text{on} \quad \Sigma \tag{10}$$

The interface Σ divides the domain into the subdomains Ω^+ and Ω^-, ϕ^+ and ϕ^- are used to denote the solution in each of the subdomains.

Define function $D(\vec{x})$ by $D(\vec{x}) = \phi^+(\vec{x}) - \phi^-(\vec{x})$ and $b(\vec{x}) = b/\sigma$. The governing equation for the resulting "ill-posed" Cauchy problem follows:

$$\nabla^2 D(\vec{x}) = \frac{f^+}{\sigma} - \frac{f^-}{\sigma} = f_D(\vec{x}) \quad \text{in} \quad \Omega \tag{11}$$

$$D(\vec{x}) = a(\vec{x}) \quad \text{on} \quad \Sigma \tag{12}$$

$$\nabla D(\vec{x}) \cdot \mathbf{n} = b(\vec{x}) \quad \text{on} \quad \Sigma \tag{13}$$

The correction term, $D(\vec{x}) = \phi^+(\vec{x}) - \phi^-(\vec{x})$, is a solution of the PDE (11-13). This PDE will be solved over a band across the interface. The Poisson's equation is discretized using the standard 5-point stencil, which is generally used to solve Poisson's equation with appropriate boundary conditions and achieve 2^{nd} order accuracy. We approximate $D(\vec{x})$ using modified bilinear (see details in 2.3.4) interpolant in each Ω_Σ^{ij}, where Ω_Σ^{ij} corresponds to a grid point at which the standard discretization of Poisson's equation involves a stencil that across the interface Σ. The definition of Ω_Σ^{ij} is given in 2.3.2. However, the Laplacian of a standard bilinear interpolant vanishes, Thus, a modified linear will be used to take full advantage of the fact that $D(\vec{x})$ is the solution to the Cauchy problem.

2.3.1 NUMERICAL METHOD FOR SOLVING CAUCHY PROBLEM

The standard second order accurate 5-point finite difference scheme is used to solve Poisson equation in two dimensions:

$$\frac{\left(\frac{u_{i+1,j}-u_{i,j}}{\triangle x}\right) - \left(\frac{u_{i,j}-u_{i-1,j}}{\triangle x}\right)}{\triangle x} + \frac{\left(\frac{u_{i,j+1}-u_{i,j}}{\triangle y}\right) - \left(\frac{u_{i,j}-u_{i,j-1}}{\triangle y}\right)}{\triangle y} = f_{i,j} \tag{14}$$

where $\triangle x = x_{i+1} - x_i$ and $\triangle y = y_{j+1} - y_j$ are the grid spacing in the horizontal and vertical directions, respectively.

If the 5-point Laplacian does not cut through the interface, we do not have to modify equation (14); On the other hand, if the 5-point Laplacian of a grid point involves using both inside and outside point(s), a correction of will be needed to ensure that the solution is smooth.

In the vicinity of the discontinuities at the interface, proper correction terms will be added to RHS of Poisson equation. In the case of Figure 2, where the node (i,j), $(i,j-1)$, $(i-1,j)$ lie in Ω^+ while the nodes $(i+1,j)$ and $(i,j+1)$ are in Ω^-, ideally, we would like to use equation (14) as follows:

$$\frac{(\frac{u^+_{i+1,j}-u^+_{i,j}}{\triangle x})-(\frac{u^+_{i,j}-u^+_{i-1,j}}{\triangle x})}{\triangle x}+\frac{(\frac{u^+_{i,j+1}-u^+_{i,j}}{\triangle y})-(\frac{u^+_{i,j}-u^+_{i,j-1}}{\triangle y})}{\triangle y}=f_{i,j} \tag{15}$$

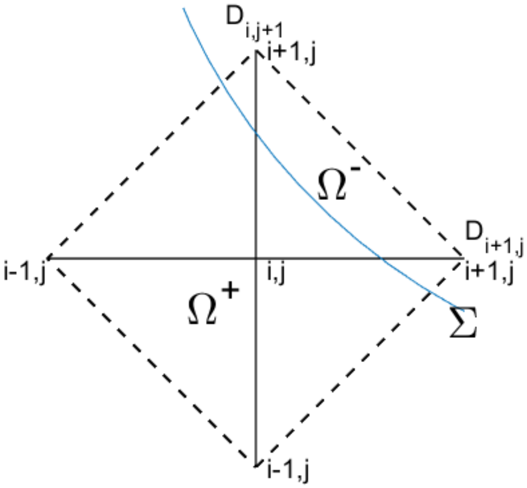

Figure. 2: A 5-point stencil enclose the interface Σ and separated into Ω^+ and Ω^-.

We do not have any information about $u_{i+1,j}$ and $u_{i,j+1}$, instead, $D_{i+1,j}=u^+_{i+1,j}-u^-_{i+1,j}$ and $D_{i,j+1}=u^+_{i,j+1}-u^-_{i,j+1}$ can be computed by using above numerical scheme.

Now, eqn. (15) becomes:

$$\frac{(\frac{u^-_{i+1,j}+D_{i+1,j}-u^+_{i,j}}{\triangle x})-(\frac{u^+_{i,j}-u^+_{i-1,j}}{\triangle x})}{\triangle x}+\frac{(\frac{u^-_{i,j+1}+D_{i,j+1}-u^+_{i,j}}{\triangle y})-(\frac{u^+_{i,j}-u^+_{i,j-1}}{\triangle y})}{\triangle y}=f_{i,j} \tag{16}$$

$D_{i+1,j}$ and $D_{i,j+1}$ are independent of solution u, we can move them to the right hand side of equation (16), that is

$$\frac{(\frac{u^-_{i+1,j}-u^+_{i,j}}{\triangle x})-(\frac{u^+_{i,j}-u^+_{i-1,j}}{\triangle x})}{\triangle x}+\frac{(\frac{u^-_{i,j+1}-u^+_{i,j}}{\triangle y})-(\frac{u^+_{i,j}-u^+_{i,j-1}}{\triangle y})}{\triangle y}=f_{i,j}+C_{i,j} \tag{17}$$

where $C_{i,j} = -\frac{1}{(\triangle x)^2} D_{i+1,j} - \frac{1}{(\triangle y)^2} D_{i,j+1}$

There are up to 12 different cases when the 5-point stencil across the interface, we apply the similar formulas for other cases than above.

2.3.2 DEFINITION OF INTEGRATION AREA Ω_{Σ}^{IJ}

In the Figure 2 of a 5-point stencil , the interface Σ across the dashed square box connecting four grid nodes $(i-1,j),(i,j-1),(i+1,j)$ and $(i,j+1)$.

In correction function method, we construct the a rectangular integration area Ω_{Σ}^{ij} such that Ω_{Σ}^{ij} contains all the nodes where D is needed. As mentioned previously in Figure 2, $D_{i,j+1}$ and $D_{i+1,j}$ are needed, and hence, the integration region should include nodes $(i+1,j)$ and $(i,j+1)$. In [21], the author introduced a method to determine the integration area that guarantee the stability and accuracy which take full advantage of 5-point stencil scheme for Poisson Equation. The strategy is briefly stated as follows.

1. Find the angle θ_{Σ} between the tangent vector $\vec{t}$ at the mid-point of interface enclosed, and the x-axis. Build a new $p-q$ coordinate system by rotating $x-y$ an angle $\theta_r = \theta_{\Sigma} - \pi/4$, as shown in Figure 3.

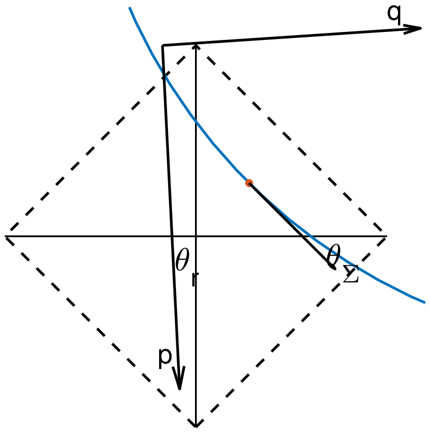

Figure. 3: A illustration of coordinate rotation.

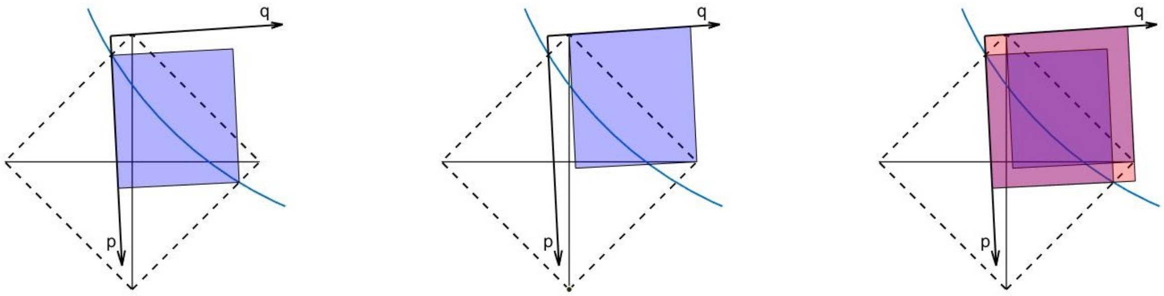

(a) Rectangle enclosing the interface within the stencil.

(b) Rectangle enclosing the all nodes need correction.

(c) Rectangle enclosing the interface and nodes.

Figure. 4: The integration region Ω_{Σ}^{ij}.

2. Find the rectangle enclosing the interface within the stencil. The rectangle is aligned with respect to the $p-$ and $q-$ directions, see Figure 4a.
3. Find the rectangle enclosing all nodes at which the computation of D is needed. The rectangle is aligned with respect to the $p-$ and $q-$ directions, see Figure 4b.
4. Ω_{Σ}^{ij} is the smallest rectangle enclosing the two previous rectangles, see Figure 4c.

2.3.3 NUMERICAL SCHEME FOR SOLVING POISSON EQUATION

We will solve the local Cauchy problem in a least square sense, using a minimization procedure. Since we don't have boundary conditions, but interface conditions, we must resort to a minimization functional that is different from the standard one associated with the Poisson equation. Thus, we impose the Cauchy interface conditions by using a penalization method. The functional to be minimized is then:

$$\begin{aligned} J_p =& (l_c^{ij})^3 \int_{\Omega_{\Sigma}^{ij}} \left(\nabla^2 D(\vec{x}) - f_D(\vec{x})\right)^2 dV + c_p \int_{\Sigma\bigcap\Omega_{\Sigma}^{ij}} \left(D(\vec{x}) - a(\vec{x})\right)^2 dS \\ &+ c_p (l_c^{ij})^2 \int_{\Sigma\bigcap\Omega_{\Sigma}^{ij}} \left(D_n(\vec{x}) - b(\vec{x})\right)^2 dS \end{aligned} \tag{18}$$

where $c_p > 0$ is the penalization coefficient used to enforce the interface conditions, and $l_c^{ij} > 0$ is a characteristic length associated with Ω_{Σ}^{ij}, the shortest side length(width). J_p is a quadratic

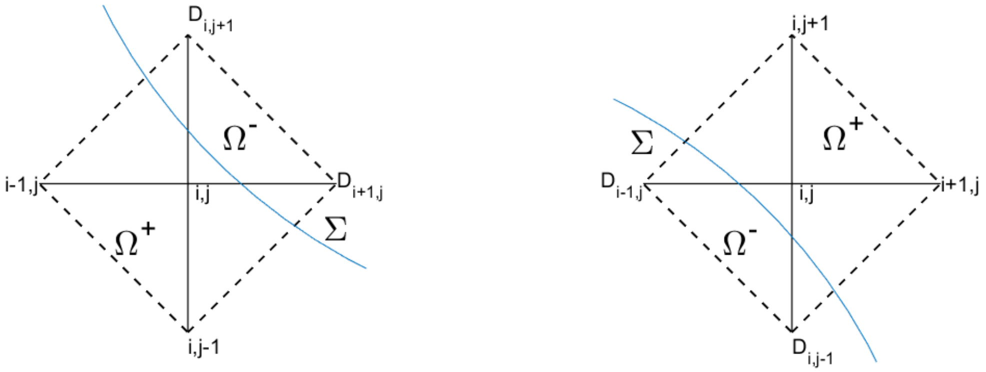

(a) Two correction terms needed at $(i+1, j)$ and $(i, j+1)$.

(b) Two correction terms needed at $(i-1, j)$ and $(i, j-1)$.

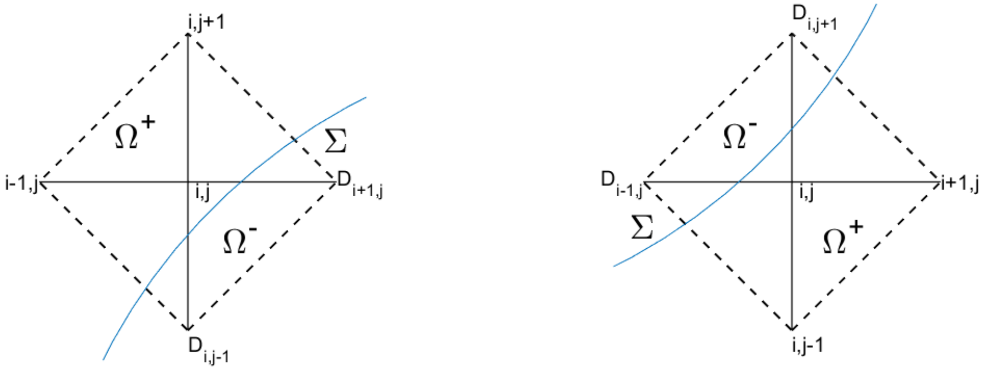

(c) Two correction terms needed at $(i+1, j)$ and $(i, j-1)$.

(d) Two correction terms needed at $(i-1, j)$ and $(i, j+1)$.

Figure. 5: Four cases of two correction terms needed in a 5-point stencil.

functional whose minimum (zero) occurs at the solution to Cauchy problem. c_p can be determined empirically from a low resolution calculation.

We use 4 Gaussian quadrature points for the 1D line integrals, and 16 points for the 2d area integrals. The modified bilinear representation for D involves 5 basis polynomials, the minimization problem produces a 5×5 linear system. Here we let $D(\vec{x}) = \sum_{i=1}^{5} D(\vec{x}_i) N_i(\xi, \eta)$ to take full advantage of the modified bilinear scheme (see 2.3.4), where $N_i (i = 1, 4)$ are standard bilinear quadrilateral element basis function in $\xi - \eta$ plane, N_5 is an quadratic term.

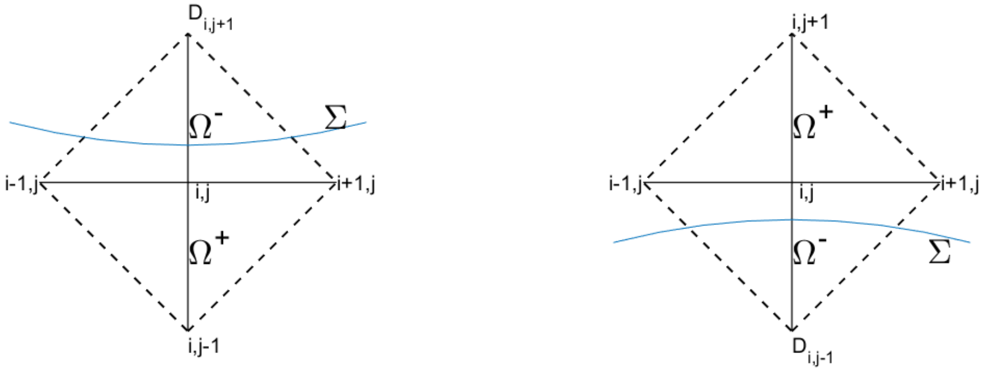

(a) One correction terms needed at $(i, j+1)$.

(b) Two correction terms needed at $(i, j-1)$.

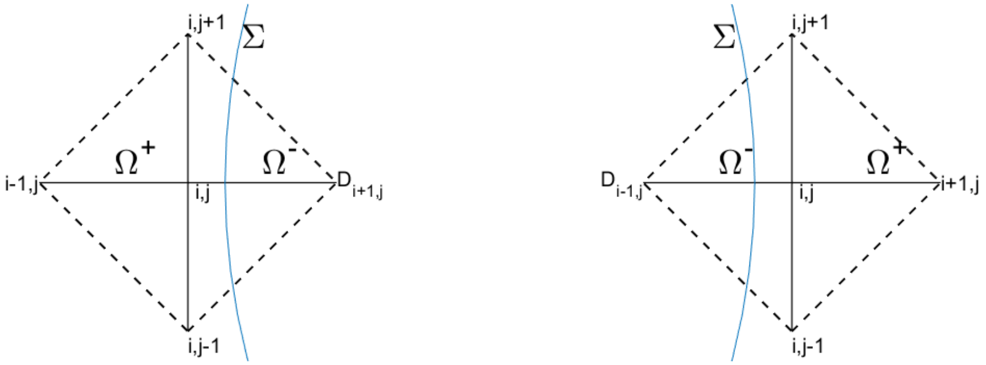

(c) Two correction terms needed at $(i+1, j)$.

(d) Two correction terms needed at $(i-1, j)$.

Figure. 6: Four cases of one correction terms needed in a 5-point stencil.

To solve $D_i(i=1,5)$, we will take partial derivative of (18) with respect to $D_i(i=1,5)$ and five equations will be obtained. For the integration

$$\int_{\Gamma\bigcap\Omega_\Gamma^{ij}} \left(D(\vec{x})-a(\vec{x})\right)^2 dS = \int_{\Gamma\bigcap\Omega_\Gamma^{ij}} \Big(\sum_{i=1}^{5} D(\vec{x}_i)N_i(\xi,\eta)-a(\vec{x})\Big)^2 dS \tag{19}$$

Take partial derivative of right hand side of (19) with respect to $D(\vec{x}_j)$ we obtain:

$$\begin{aligned}
&\frac{\partial}{\partial D_j}\int_{\Gamma\bigcap\Omega_\Gamma^{ij}}\big(\sum_{i=1}^{5}D(\vec{x}_i)N_i(\xi,\eta)-a(\vec{x})\big)^2 dS\\
=&\int_{\Gamma\bigcap\Omega_\Gamma^{ij}}2\big(\sum_{i=1}^{5}D(\vec{x}_i)N_i(\xi,\eta)-a(\vec{x})\big)N_j(\xi,\eta)dS\\
=&2\int_{\Gamma\bigcap\Omega_\Gamma^{ij}}\sum_{i=1}^{5}D(\vec{x}_i)N_i(\xi,\eta)N_j(\xi,\eta)dS-2\int_{\Gamma\bigcap\Omega_\Gamma^{ij}}a(\vec{x})N_j(\xi,\eta)dS \qquad (20)
\end{aligned}$$

Similarly, for the integration

$$\int_{\Gamma\bigcap\Omega_\Gamma^{ij}}\big(D_n(\vec{x})-b(\vec{x})\big)^2 dS \qquad (21)$$

where

$$D_n(\vec{x})=\sum_{i=1}^{5}D(\vec{x}_i)\nabla N_i(\xi,\eta)\cdot\vec{n}$$

Take partial derivative of eqn. (21) with respect to $D(\vec{x}_j)$ we obtain:

$$\begin{aligned}
&\frac{\partial}{\partial D_j}\int_{\Gamma\bigcap\Omega_\Gamma^{ij}}\big(D_n(\vec{x})-b(\vec{x})\big)^2 dS\\
=&\frac{\partial}{\partial D_j}\int_{\Gamma\bigcap\Omega_\Gamma^{ij}}\big(\sum_{i=1}^{5}D(\vec{x}_i)\nabla N_i(\xi,\eta)\cdot\vec{n}-b(\vec{x})\big)^2 dS\\
=&\int_{\Gamma\bigcap\Omega_\Gamma^{ij}}2\big(\sum_{i=1}^{5}D(\vec{x}_i)\nabla N_i(\xi,\eta)\cdot\vec{n}-b(\vec{x})\big)\nabla N_j(\xi,\eta)\cdot\vec{n}dS\\
=&2\int_{\Gamma\bigcap\Omega_\Gamma^{ij}}\sum_{i=1}^{5}D(\vec{x}_i)(\nabla N_i(\xi,\eta)\cdot\vec{n})(\nabla N_j(\xi,\eta)\cdot\vec{n})dS-2\int_{\Gamma\bigcap\Omega_\Gamma^{ij}}b(\vec{x})(\nabla N_j(\xi,\eta)\cdot\vec{n})dS \qquad (22)
\end{aligned}$$

Finally, for the integration

$$\int_{\Omega_\Gamma^{ij}}\big(\nabla^2 D(\vec{x})-f_D(\vec{x})\big)^2 dV \qquad (23)$$

where

$$\nabla^2 D(\vec{x})=\sum_{i=1}^{5}D(\vec{x}_i)\nabla^2 N_i(\xi,\eta)$$

Take partial derivative of eqn. (23) with respect to $D(\vec{x}_j)$ we obtain:

$$\begin{aligned}
&\frac{\partial}{\partial D_j}\int_{\Omega_\Gamma^{ij}}\big(\nabla^2 D(\vec{x})-f_D(\vec{x})\big)^2 dV\\
=&\frac{\partial}{\partial D_j}\int_{\Omega_\Gamma^{ij}}\big(\sum_{i=1}^{5} D(\vec{x}_i)\nabla^2 N_i(\xi,\eta)-f_D(\vec{x})\big)^2 dV\\
=&\int_{\Omega_\Gamma^{ij}} 2\big(\sum_{i=1}^{5} D(\vec{x}_i)\nabla^2 N_i(\xi,\eta)-f_D(\vec{x})\big)\nabla^2 N_j(\xi,\eta)dV\\
=&2\int_{\Omega_\Gamma^{ij}}\sum_{i=1}^{5} D(\vec{x}_i)\nabla^2 N_i(\xi,\eta)\nabla^2 N_j(\xi,\eta)dV-2\int_{\Omega_\Gamma^{ij}} f_D(\vec{x})\nabla^2 N_j(\xi,\eta)dV
\end{aligned}\tag{24}$$

Take partial derivative of (18) with respect to $D(\vec{x}_j)$ and (20), (22) and (24) are substituted into to get:

$$\begin{aligned}
0=&\frac{\partial}{\partial D_j}\Big\{(l_c^{ij})^3\int_{\Omega_\Gamma^{ij}}\big(\nabla^2 D(\vec{x})-f_D(\vec{x})\big)^2 dV+c_p\int_{\Gamma\bigcap\Omega_\Gamma^{ij}}\big(D(\vec{x})-a(\vec{x})\big)^2 dS\\
&+c_p(l_c^{ij})^2\int_{\Gamma\bigcap\Omega_\Gamma^{ij}}\big(D_n(\vec{x})-b(\vec{x})\big)^2 dS\Big\}\\
=&(l_c^{ij})^3\int_{\Omega_\Gamma^{ij}}\sum_{i=1}^{5} D(\vec{x}_i)\nabla^2 N_i(\xi,\eta)\nabla^2 N_j(\xi,\eta)dV-(l_c^{ij})^3\int_{\Omega_\Gamma^{ij}} f_D(\vec{x})\nabla^2 N_j(\xi,\eta)dV\\
&+c_p\int_{\Gamma\bigcap\Omega_\Gamma^{ij}}\sum_{i=1}^{5} D(\vec{x}_i)N_i(\xi,\eta)N_j(\xi,\eta)dS-c_p\int_{\Gamma\bigcap\Omega_\Gamma^{ij}} a(\vec{x})N_j(\xi,\eta)dS\\
&+c_p(l_c^{ij})^2\int_{\Gamma\bigcap\Omega_\Gamma^{ij}}\sum_{i=1}^{5} D(\vec{x}_i)(\nabla N_i(\xi,\eta)\cdot\vec{n})(\nabla N_j(\xi,\eta)\cdot\vec{n})dS\\
&-c_p(l_c^{ij})^2\int_{\Gamma\bigcap\Omega_\Gamma^{ij}} b(\vec{x})(\nabla N_j(\xi,\eta)\cdot\vec{n})dS
\end{aligned}\tag{25}$$

Or, equivalently, we can rewrite (25) as

$$\begin{aligned}
&\sum_{i=1}^{5} D(\vec{x}_i)\bigg((l_c^{ij})^3\int_{\Omega_\Gamma^{ij}}\nabla^2 N_i(\xi,\eta)\nabla^2 N_j(\xi,\eta)dV+c_p\int_{\Gamma\bigcap\Omega_\Gamma^{ij}} N_i(\xi,\eta)N_j(\xi,\eta)dS\\
&+c_p(l_c^{ij})^2\int_{\Gamma\bigcap\Omega_\Gamma^{ij}}(\nabla N_i(\xi,\eta)\cdot\vec{n})(\nabla N_j(\xi,\eta)\cdot\vec{n})dS\bigg)\\
=&(l_c^{ij})^3\int_{\Omega_\Gamma^{ij}} f_D(\vec{x})\nabla^2 N_j(\xi,\eta)dV+c_p\int_{\Gamma\bigcap\Omega_\Gamma^{ij}} a(\vec{x})N_j(\xi,\eta)dS\\
&+c_p(l_c^{ij})^2\int_{\Gamma\bigcap\Omega_\Gamma^{ij}} b(\vec{x})(\nabla N_j(\xi,\eta)\cdot\vec{n})dS
\end{aligned}\tag{26}$$

To evaluate the integration $\int_{\Omega_\Gamma^{ij}} \nabla^2 N_i(\xi,\eta)\nabla^2 N_j(\xi,\eta)dV$, we first calculate the Jacobian of the transformation which is defined by

$$J(\xi,\eta) = \left|\frac{\partial(x,y)}{\partial(\xi,\eta)}\right| = \begin{vmatrix} \dfrac{\partial x}{\partial \xi} & \dfrac{\partial y}{\partial \xi} \\ \dfrac{\partial x}{\partial \eta} & \dfrac{\partial y}{\partial \eta} \end{vmatrix}, \tag{27}$$

Then we have

$$\begin{aligned} &\int_{\Omega_{\Gamma}^{ij}(x,y)} \nabla^2 N_i(\xi(x,y),\eta(x,y))\nabla^2 N_j(\xi(x,y),\eta(x,y))dxdy \\ =&\int_{\Omega_{\Gamma}^{ij}(\xi,\eta)} \nabla^2 N_i(\xi,\eta)\nabla^2 N_j(\xi,\eta)|J(\xi,\eta)|d\xi d\eta \end{aligned} \tag{28}$$

where

$$\begin{aligned} &\nabla^2 N_i(\xi(x,y),\eta(x,y)) \\ =&(\frac{\partial}{\partial x},\frac{\partial}{\partial y})\cdot(\frac{\partial N_i(\xi(x,y),\eta(x,y))}{\partial x},\frac{\partial N_i(\xi(x,y),\eta(x,y))}{\partial y}) \\ =&(\frac{\partial}{\partial x},\frac{\partial}{\partial y})\cdot(\frac{\partial N_i(\xi,\eta)}{\partial \xi}\frac{\partial \xi}{\partial x}+\frac{\partial N_i(\xi,\eta)}{\partial \eta}\frac{\partial \eta}{\partial x},\frac{\partial N_i(\xi,\eta)}{\partial \xi}\frac{\partial \xi}{\partial y}+\frac{\partial N_i(\xi,\eta)}{\partial \eta}\frac{\partial \eta}{\partial y}) \end{aligned}$$

From (1) and using the definition of $N_i(\xi,\eta)$, we have

$$\begin{aligned} \frac{\partial N_1}{\partial \xi} &= -\frac{1}{4}(1-\eta) & \frac{\partial N_1}{\partial \eta} &= -\frac{1}{4}(1-\xi) \\ \frac{\partial N_2}{\partial \xi} &= \frac{1}{4}(1-\eta) & \frac{\partial N_2}{\partial \eta} &= -\frac{1}{4}(1+\xi) \\ \frac{\partial N_3}{\partial \xi} &= \frac{1}{4}(1+\eta) & \frac{\partial N_3}{\partial \eta} &= \frac{1}{4}(1+\xi) \\ \frac{\partial N_4}{\partial \xi} &= -\frac{1}{4}(1+\eta) & \frac{\partial N_4}{\partial \eta} &= \frac{1}{4}(1-\xi) \\ \frac{\partial N_5}{\partial \xi} &= -\frac{\xi}{2} & \frac{\partial N_5}{\partial \eta} &= -\frac{\eta}{2} \end{aligned} \tag{29}$$

Finally, we derive the following expressions for $\nabla^2 N_i(\xi,\eta)$:

$$\begin{aligned}
\nabla^2 N_1(\xi,\eta) &= \frac{1}{2}\Big((\frac{\partial \xi}{\partial x})(\frac{\partial \eta}{\partial x}) + (\frac{\partial \xi}{\partial y})(\frac{\partial \eta}{\partial y})\Big)\\
\nabla^2 N_2(\xi,\eta) &= -\frac{1}{2}\Big((\frac{\partial \xi}{\partial x})(\frac{\partial \eta}{\partial x}) + (\frac{\partial \xi}{\partial y})(\frac{\partial \eta}{\partial y})\Big)\\
\nabla^2 N_3(\xi,\eta) &= \frac{1}{2}\Big((\frac{\partial \xi}{\partial x})(\frac{\partial \eta}{\partial x}) + (\frac{\partial \xi}{\partial y})(\frac{\partial \eta}{\partial y})\Big)\\
\nabla^2 N_4(\xi,\eta) &= -\frac{1}{2}\Big((\frac{\partial \xi}{\partial x})(\frac{\partial \eta}{\partial x}) + (\frac{\partial \xi}{\partial y})(\frac{\partial \eta}{\partial y})\Big)\\
\nabla^2 N_5(\xi,\eta) &= \frac{1}{2}\Big((\frac{\partial \xi}{\partial x})^2 + (\frac{\partial \eta}{\partial x})^2 + (\frac{\partial \xi}{\partial y})^2 + (\frac{\partial \eta}{\partial y})^2\Big)
\end{aligned}$$

$\nabla^2 N_i(\xi(x,y),\eta(x,y)) = 0$ for $i = 1,2,3,4$ since they are bilinear quadrilateral basis functions.

To evaluate $\int_{\Gamma\bigcap\Omega_\Gamma^{ij}}(\nabla N_i(\xi,\eta)\cdot\vec{n})(\nabla N_j(\xi,\eta)\cdot\vec{n})dS$, where $\vec{n} = (n_x,n_y)$, by the definition of $N_i(\xi,\eta)$, we have

$$\begin{aligned}
\nabla N_i(\xi(x,y),\eta(x,y)) &= \Big(\frac{\partial N_i(\xi(x,y),\eta(x,y))}{\partial x}, \frac{\partial N_i(\xi(x,y),\eta(x,y))}{\partial y}\Big)\\
&= \Big(\frac{\partial N_i(\xi,\eta)}{\partial \xi}\frac{\partial \xi}{\partial x} + \frac{\partial N_i(\xi,\eta)}{\partial \eta}\frac{\partial \eta}{\partial x}, \frac{\partial N_i(\xi,\eta)}{\partial \xi}\frac{\partial \xi}{\partial y} + \frac{\partial N_i(\xi,\eta)}{\partial \eta}\frac{\partial \eta}{\partial y}\Big)
\end{aligned}$$

The (i,j) entry is

$$\begin{aligned}
&\int_{\Gamma\bigcap\Omega_\Gamma^{ij}}(\nabla N_i(\xi,\eta)\cdot\vec{n})(\nabla N_j(\xi,\eta)\cdot\vec{n})dS\\
=&\int_{\Gamma\bigcap\Omega_\Gamma^{ij}}\Big[(\frac{\partial N_i(\xi,\eta)}{\partial \xi}\frac{\partial \xi}{\partial x} + \frac{\partial N_i(\xi,\eta)}{\partial \eta}\frac{\partial \eta}{\partial x})n_x + (\frac{\partial N_i(\xi,\eta)}{\partial \xi}\frac{\partial \xi}{\partial y} + \frac{\partial N_i(\xi,\eta)}{\partial \eta}\frac{\partial \eta}{\partial y})n_y\Big]\\
&\Big[(\frac{\partial N_j(\xi,\eta)}{\partial \xi}\frac{\partial \xi}{\partial x} + \frac{\partial N_j(\xi,\eta)}{\partial \eta}\frac{\partial \eta}{\partial x})n_x + (\frac{\partial N_j(\xi,\eta)}{\partial \xi}\frac{\partial \xi}{\partial y} + \frac{\partial N_j(\xi,\eta)}{\partial \eta}\frac{\partial \eta}{\partial y})n_y\Big]dS
\end{aligned}$$

where $\vec{n} = (n_x,n_y)$. Now we are ready to compute $D(\vec{x})$ in different cases, depending on the way how the interface intersect the stencil.

2.3.4 MODIFIED BILINEAR INTERPOLATION

Since each cell Ω_Σ^{ij} is arbitrary rectangle, in order to use Gaussian Quadrature, we will map this rectangle from $x-y$ plane to $\xi-\eta$ plane.

The standard bilinear quadrilateral element basis function in (ξ,η) plane:

$$N_1(\xi,\eta) = \frac{1}{4}(1-\xi)(1-\eta) \tag{30}$$

$$N_2(\xi,\eta) = \frac{1}{4}(1+\xi)(1-\eta) \tag{31}$$

$$N_3(\xi,\eta) = \frac{1}{4}(1+\xi)(1+\eta) \tag{32}$$

$$N_4(\xi,\eta) = \frac{1}{4}(1-\xi)(1+\eta) \tag{33}$$

The standard bilinear interpolation of a scalar function ϕ is given by

$$\phi(\vec{x}) = \sum_{i=1}^{4} \phi_i N_i(\xi,\eta)$$

where ϕ_i represents the function value of ϕ at point i.

Now, we add a quadratic term proportional to $\xi^2+\eta^2$, so that the Laplacian of the modified bilinear is no longer identically zero.

The coefficient of the quadratic term can be written in terms of the average value of the Laplacian over the domain, $\overline{\nabla^2\phi}$. We obtain the following formula for the modified bilinear interpolant:

$$\phi(\vec{x}) = \sum_{i=1}^{4} \phi_i N_i(\xi,\eta) - \frac{1}{4}\big((1-\xi)(1+\xi)+(1-\eta)(1+\eta)\big)\overline{\nabla^2\phi}$$

In addition to the standard basis function, for convenience, we define $N_5(\xi,\eta)$ and $\phi_5(\vec{x})$ as follows:

$$\begin{aligned} N_5(\xi,\eta) &= \frac{1}{4}\big((1-\xi)(1+\xi)+(1-\eta)(1+\eta)\big) \\ \phi_5(\vec{x}) &= \overline{\nabla^2\phi(\vec{x})} \end{aligned}$$

This yields the compact form of modified bilinear interpolant:

$$\phi(\vec{x}) = \sum_{i=1}^{5} \phi_i N_i(\xi,\eta)$$

To solve ξ and η, we use the following relationship between the four vertices: (x_i, y_i) and

(ξ_i, η_i) as follows:

$$x_i = a_1 + a_2\xi_i + a_3\eta_i + a_4\xi_i\eta_i$$

$$y_i = b_1 + b_2\xi_i + b_3\eta_i + b_4\xi_i\eta_i$$

We next use these expressions to solve for the four coefficients:

$$\begin{pmatrix} x_1 \\ x_2 \\ x_3 \\ x_4 \end{pmatrix} = \begin{pmatrix} 1 & -1 & -1 & 1 \\ 1 & 1 & -1 & -1 \\ 1 & 1 & 1 & 1 \\ 1 & -1 & 1 & -1 \end{pmatrix} \begin{pmatrix} a_1 \\ a_2 \\ a_3 \\ a_4 \end{pmatrix} \tag{34}$$

This can be easily done by inverting the matrix:

$$\begin{pmatrix} a_1 \\ a_2 \\ a_3 \\ a_4 \end{pmatrix} = \begin{pmatrix} 1 & -1 & -1 & 1 \\ 1 & 1 & -1 & -1 \\ 1 & 1 & 1 & 1 \\ 1 & -1 & 1 & -1 \end{pmatrix}^{-1} \begin{pmatrix} x_1 \\ x_2 \\ x_3 \\ x_4 \end{pmatrix} \tag{35}$$

To obtain the reverse mapping, we need to solve

$$x = a_1 + a_2\xi + a_3\eta + a_4\xi\eta$$

$$y = b_1 + b_2\xi + b_3\eta + b_4\xi\eta$$

Note this system is no longer linear, however it can be solved quite easily analytically. We first obtain

$$\xi = \frac{x - a_1 - a_3\eta}{a_2 + a_4\eta}$$

Which can be substitute into the second expression to obtain:

$$\begin{aligned} & a_4b_3 - a_3b_4)\eta^2 + (a_4b_1 - a_1b_4 + a_2b_3 - a_3b_2 + xb_4 - ya_4)\eta \\ & + (a_2b_1 - a_1b_2 + xb_2 - ya_2) = 0 \end{aligned}$$

This is a quadratic equation can be solved by using quadratic formula.

For our problem, the transformation of arbitrary rectangle is always linear, this implies that $a_4 = b_4 = 0$, we calculated other coefficients as follows:

$$
\begin{aligned}
a_1 &= \frac{1}{4}(x_1 + x_2 + x_3 + x_4) \qquad & b_1 &= \frac{1}{4}(y_1 + y_2 + y_3 + y_4) \\
a_2 &= \frac{1}{4}(x_2 - x_1 + x_3 - x_4) \qquad & b_2 &= \frac{1}{4}(y_2 - y_1 + y_3 - y_4) \\
a_3 &= \frac{1}{4}(x_3 + x_4 - x_1 - x_2) \qquad & b_3 &= \frac{1}{4}(y_3 + y_4 - y_1 - y_2)
\end{aligned}
$$

Solve for ξ and η, we obtain:

$$\xi = \frac{-a_1 b_3 + b_1 a_3 - a_3 y + b_3 x}{a_2 b_3 - b_2 a_3} \tag{36}$$

$$\eta = -\left(\frac{-a_1 b_2 + b_1 a_2 - a_2 y + b_2 x}{a_2 b_3 - b_2 a_3}\right) \tag{37}$$

2.3.5 NUMERICAL EXAMPLES

In this section, we shall demonstrate some examples widely used in other literatures. The maximum norm L^∞ is used to measure the errors in the computed solution u. Let u_e be the exact solution, the L^∞ error in u is defined as $L^\infty_{error} = \|u - u_e\|_\infty$. The convergence rate is related to the number of grid points N and grid spacing parameter h. A practical method to calculate the order of convergence for a discretization method is to implement the following formula

$$p \approx \frac{\log(error_{new}/error_{old})}{\log(h_{new}/h_{old})}$$

The ratio is defined as

$$\text{Ratio} = \frac{error_{old}}{error_{new}}$$

For a second order accurate method, the ratio approaches to 4 in each step of mesh refinement. An average ratio of 4 indicates second order convergence. We use the same notation for all examples in this thesis.

Example 1

Consider $\nabla\cdot(\sigma u)=0$ in two dimensions on $[-1,1]\times[-1,1]$ with the interface defined by the circle $x^2+y^2=0.5^2$. In this example, $\sigma^+=\sigma^-=1$. The jump conditions on the interface is $[u]=0$ and $[u_n]=2$, with Dirichlet boundary conditions $1+\log(2\sqrt{X^2+Y^2})$, $(X,Y)\in\partial\Omega$ at boundary, directly computed from the exact solution. The Lagrangian control points are 140 on the immersed interface. The exact solution is

$$u(x,y)=\begin{cases}1+\log(2\sqrt{x^2+y^2}), & (x,y)\in\Omega^+\\ 1, & (x,y)\in\Omega^-\end{cases}$$

Table 1 shows the numerical accuracy and convergence tests.

TABLE 1: Accuracy and convergence test for Example 1

N	L^∞ error in u	Ratio	Order
21	2.07059e-03	-	-
41	2.29257e-04	9.0317	3.28936
81	9.10811e-05	2.5171	1.35574
161	1.84140e-05	4.9463	2.32714
321	4.91145e-06	3.7492	1.91517
641	1.35885e-06	3.6144	1.85795

Figure 7 shows the convergence results for the errors in the L_∞ norms.

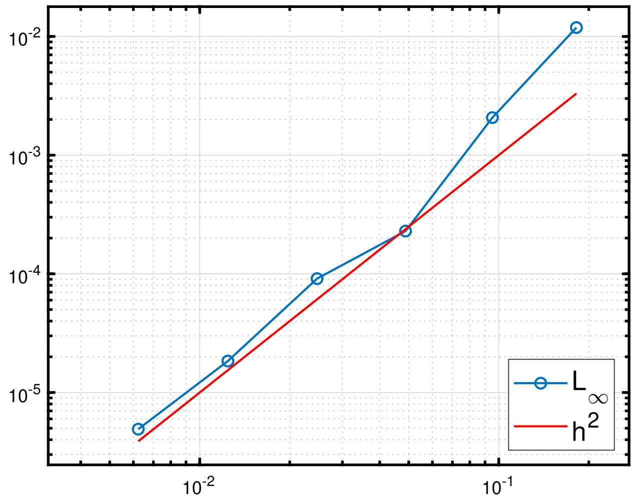

Figure. 7: error behaviour of the solution

Figure 8 shows the plots of numerical solutions with grids 21, 41, 81, 161, 321 and 641, from top to bottom, left to right, respectively.

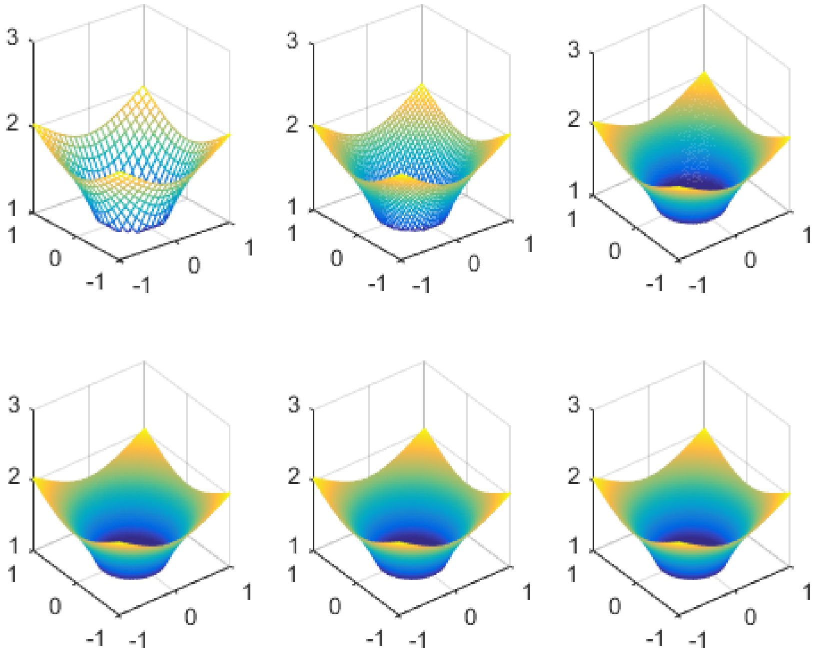

Figure. 8: Numerical solutions

Example 2

This is an **example** taken from [23]. (Example 7). Consider $\nabla^2 u = 0$ in two spatial dimensions on $[-1,1]\times[-1,1]$ with the interface defined by the circle $x^2+y^2=0.5^2$ with an outward pointing normal vector, $\vec{n}=(2x,2y)$.

The jump conditions are:

$$[u]_\Sigma = y^2 - x^2$$

$$[u_n]_\Sigma = 4(y^2 - x^2)$$

The exact solution is

$$u(x,y) = \begin{cases} x^2 - y^2 & (x,y)\in\Omega^- \\ 0 & (x,y)\in\Omega^+ \end{cases}$$

Table 2 shows the results of numerical accuracy.

TABLE 2: Accuracy and convergence test for Example 1

N	L^∞ error in u	Ratio	Order
11	8.19894e-03	-	-
21	2.28310e-03	3.5911	1.97714
41	6.24386e-04	3.6566	1.93785
81	2.33045e-04	2.6793	1.44745
161	5.25309e-05	4.4363	2.16874
321	1.41005e-05	3.7255	1.90598

Figure 9 shows the convergence results for the errors in the L_∞ norms.

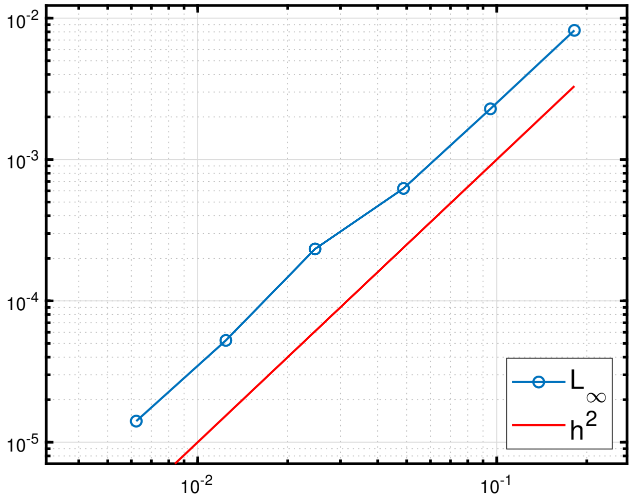

Figure. 9: error behaviour of the solution

Figure 10 shows the numerical solution with 11, 21, 41, 81, 161 and 321 grid points in each direction, from top to bottom, left to right, respectively.

The Correction Function Method (CFM) is a robust scheme that can deal with the complicated interface geometry, and can even be developed to 4th order scheme based on the compact 9-point stencil discretization of the Poisson equation, see details in [21]. We are able to use this method to solve electric potential under the assumption that the conductivity σ is constant through the entire computational domain. Unfortunately, the Correction Function Method cannot applied to the situation where σ^+ and σ^- are unequal. The explanation is given in [21]. Due to the drawback of correction function method, we move forward on the fast immersed interface method which can deal with discontinuity in σ.

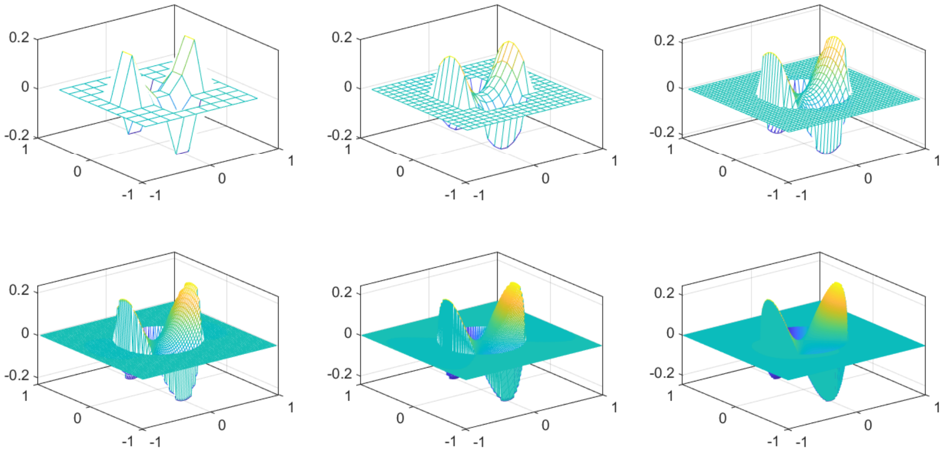

Figure. 10: Plots of Numerical Solutions

2.4 FAST IMMERSED INTERFACE METHOD FOR SOLVING ELLIPTIC INTERFACE PROBLEM

The fast immersed interface method is employed to impose the jump conditions at the interface. This method is originally developed by Z. Li in [22] used to solve elliptic interface problems.

We consider the problem on a computational domain Ω with an immersed interface Σ. The interface Σ divides the domain Ω into two regions; namely inside (Ω^-) and outside (Ω^+) of the interface. Without loss of generality, we consider the following elliptic interface problem with inhomogeneous jumps as

$$\nabla \cdot (\sigma \nabla \phi) = f \text{ in } \Omega \backslash \Sigma \tag{38}$$

$$[\phi] = w \text{ on } \Sigma \tag{39}$$

$$[\sigma \nabla \phi \cdot \mathbf{n}] = v \text{ on } \Sigma \tag{40}$$

The above equation should be accompanied with some suitable boundary condition (Dirichlet or Neumann condition) along the computational domain $\partial\Omega$. Other boundary conditions will not change the main ingredients presented here. Note that, the jumps $v(s)$ and $w(s)$ are both functions defined on the interface Σ. Since σ is piecewise constant, we can rewrite the above equation in the form of Poisson equation $\Delta\phi = \dfrac{f}{\sigma}$ in different domains Ω^+ and Ω^- with the same jump conditions. In the following, we use the shorthand ϕ_n to represent the normal derivative $\nabla\phi \cdot \mathbf{n}$.

We consider the following alternate problem using a unknown jump condition $\phi_n = g(s)$:

$$\Delta\phi^+ = \frac{f^+}{\sigma^+} \quad \text{in} \quad \Omega^+ \tag{41}$$

$$\Delta\phi^- = \frac{f^-}{\sigma^-} \quad \text{in} \quad \Omega^- \tag{42}$$

$$[\phi] = w, \quad [\sigma\phi_n] = v, \quad [\phi_n] = g, \quad \text{on} \quad \Sigma. \tag{43}$$

Solving alternate problem (41)–(43) is equivalent to solve original problem. Consider the problem on a rectangular domain $[a,b] \times [c,d]$ with a uniform grid

$$x_i = a + ih, \quad y_j = a + jh, \quad 0 \le i \le m, 0 \le j \le n$$

The immersed interface $\Sigma : \{\mathbf{X}(s) = (X(s), Y(s)), 0 \le s < 2\pi\}$ is presented as a cubic spline passing through a set of Lagrangian points (X_k, Y_k) on Σ, where $k = 1, 2, ..., N$. The grid points (x_i, y_j) are defined at the cell center where discrete solution ϕ_{ij} are located. The grid point is identified as either a regular or irregular point. If the 5-point Laplacian stencil of a grid point does not cut through the interface, then that grid point is labelled as regular point; otherwise, the grid point is irregular point, no matter it's in Ω^+ or Ω^-. When (x_i, y_j) is an irregular point, a correction term C_{ij} is required to add to the standard 5-point Laplacian stencil which incorporate the boundary condition on the interface Σ. Thus, the discretization of equation: in a uniform Cartesian grid with equal mesh size is as follows

$$\frac{\phi_{i+1,j} - 2\phi_{i,j} + \phi_{i-1,j}}{h^2} + \frac{\phi_{i,j+1} - 2\phi_{i,j} + \phi_{i,j-1}}{h^2} = \bar{f}_{ij} + c_{ij} \tag{44}$$

The correction term c_{ij} is zero unless (x_i, y_j) is irregular grid point, $\bar{f}_{ij} = \dfrac{f^+_{ij}}{\sigma^+}$ if (x_i, y_j) is in Ω^+ and $\bar{f}_{ij} = \dfrac{f^-_{ij}}{\sigma^-}$ if (x_i, y_j) is in Ω^-.

Now we describe the fast immersed interface method in details. We shall use lower-case letters and upper-case letters to distinguish continuous format and discrete format. See the following correspondences

Φ : ϕ in equation (44)
F : $\bar{f}$ in equation (44)
C : c in equation (44)
G : the unknown interface jump condition g in (43)
W : the interface jump condition w in (43)
V : the interface jump condition v in (43)
L : standard five points discrete Laplacian operator

The discrete form of (44) becomes

$$L\Phi = F + C \tag{45}$$

The correction term, C, has been proved in [24, 25], is a linear combination of W and G

$$C = AW - BG \tag{46}$$

where A and B are two matrices with real entries correspond to the correction terms in the immersed interface method implemented from their positions around the vicinity of the interface. The equation (45) becomes

$$L\Phi + BG = F + AW = F_1 \tag{47}$$

The discrete form of boundary condition $[\sigma\phi_n] = v$ is

$$\sigma^+\Phi_n^+ - \sigma^-\Phi_n^- - V = 0 \tag{48}$$

The unknown boundary condition $[\phi_n] = g$, is fully connected with the boundary condition $[\sigma\phi_n] =$

v, σ^+ and σ^- through an interpolation scheme, which is proposed by Xu [23] as follows

$$\phi_n^+ + \frac{\sigma^-}{[\sigma]}[\phi_n] = \frac{[\sigma\phi_n]}{[\sigma]}, \quad \text{if} \quad \sigma^- > \sigma^+ \tag{49}$$

$$\phi_n^- + \frac{\sigma^+}{[\sigma]}[\phi_n] = \frac{[\sigma\phi_n]}{[\sigma]}, \quad \text{if} \quad \sigma^+ > \sigma^- \tag{50}$$

At each Lagrangian point $\mathbf{X_c} = (x_c, y_c)$ on the interface Σ, We use the weighted least squares (see details in 2.4.2) to approximate $\phi_n^+(\mathbf{X_c})$ and $\phi_n^-(\mathbf{X_c})$. This approach has second-order of accuracy for the derivatives. With this approximation, we can rewrite (49)-(50) in matrix form linearly as

$$D\Phi + EG = PV \tag{51}$$

where D denote the matrices resulting from the weighted least square approximation, E is the constant matrix, $\frac{\sigma^-}{[\sigma]}I$ or $\frac{\sigma^+}{[\sigma]}I$, determined by (49) or (50); and $P = \frac{1}{[\sigma]}I$. As proved in [26], Φ_n^+ and Φ_n^- depend on D, G and V linearly and given by the following equation

$$\sigma^+\Phi_n^+ - \sigma^-\Phi_n^- - V = D\Phi + EG - PV \tag{52}$$

The proof of (52) is straight forward. Multiply (49) by $[\sigma]$, we have

$$[\sigma]\phi_n^+ + \sigma^-[\phi_n] = [\sigma\phi_n] \tag{53}$$

By applying the jump conditions, we can perform the following operations

$$\begin{aligned} 0 &= [\sigma]\phi_n^+ + \sigma^-[\phi_n] - [\sigma\phi_n] \\ &= \sigma^+\phi_n^+ - \sigma^-\phi_n^+ + \sigma^-\phi_n^+ - \sigma^-\phi_n^- - [\sigma\phi_n] \\ &= \sigma^+\phi_n^+ - \sigma^-\phi_n^- - [\sigma\phi_n] \end{aligned}$$

Thus we can obtain the following expression of the continuous form of (52)

$$\phi_n^+ + \frac{\sigma^-}{[\sigma]}[\phi_n] - \frac{[\sigma\phi_n]}{[\sigma]} = \sigma^+\phi_n^+ - \sigma^-\phi_n^+ - [\sigma\phi_n] \tag{54}$$

and the same operation can be done in a similar manner for (50)

$$\phi_n^- + \frac{\sigma^+}{[\sigma]}[\phi_n] = \frac{[\sigma\phi_n]}{[\sigma]} = \sigma^+\phi_n^+ - \sigma^-\phi_n^+ - [\sigma\phi_n] \tag{55}$$

Now we are ready to solve following the system of equations (47) and (51) using immersed interface method.

$$\begin{bmatrix} L & B \\ D & E \end{bmatrix} \begin{bmatrix} \Phi \\ G \end{bmatrix} = \begin{bmatrix} F_1 \\ PV \end{bmatrix} \tag{56}$$

First, we eliminate Φ to obtain system for G. The dimension of G is the same as the number of Lagrangian points on the interface, and is much smaller than the dimension of Φ, which is defined at all grid points. We obtain the system with G:

$$\begin{aligned} (E - DL^{-1}B)G &= PV - DL^{-1}F_1 \\ &= \bar{V} \end{aligned} \tag{57}$$

This is an $n_b \times n_b$ system for G, a much smaller linear system compared to the one for Φ, n_b is the number of control points used on the interface. An iterative method, such as GMRES (see 2.4.1) iteration, is preferred to solve (57). To compute $\bar{V}$ in (57), we first set $G = 0$ in (47) and apply one step of the immersed interface method (see [24]) to solve (47) to get $\Phi(0) = L^{-1}F_1$. Next, compute the normal derivatives on each side of the interface to get $\Phi_n^{\pm}(0)$ (see details in 2.4.2). Thus the right-hand side of equation (57) is

$$\begin{aligned} \bar{V} &= PV - DL^{-1}F_1 \\ &= PV - D\Phi(0) \\ &= -(D\Phi(0) + EG - PV) \quad (\text{ because } G = 0) \\ &= -(\sigma^+\Phi_n^+(0) - \sigma^-\Phi_n^-(0) - V) \end{aligned} \tag{58}$$

Consider the matrix-vector multiplication $(E - DL^{-1}B)G$ in (57), which will be used in GMRES iteration. This can be done by avoiding the matrix-vector multiplication involves two steps in practice as follows [26].

1. Set $G = G^*$ initially and apply a fast Poisson solver to compute Φ^* in (47)

$$\Phi^* = L^{-1}(F_1 - BG^*) \tag{59}$$

2. Apply weighted least square interpolation to compute $(\Phi_n^+)^*$ and $(\Phi_n^-)^*$, and the residual vector in the flux jump condition is

$$R^* = V - (\sigma^+(\Phi_n^+)^* - \sigma^-(\Phi_n^-)^*) \tag{60}$$

or according to (52),

$$R^* = PV - (D\Phi^* + EG^*) \tag{61}$$

The matrix-vector multiplication $(E - DL^{-1}B)G^* = EG^* - DL^{-1}BG^*$, where $L^{-1}BG^* = L^{-1}F_1 - \Phi^*$. Now we have

$$\begin{aligned}
(E - DL^{-1}B)G^* &= EG^* - DL^{-1}BG^* \\
&= EG^* - D(L^{-1}F_1 - \Phi^*) \\
&= EG^* + D\Phi^* - DL^{-1}F_1 \\
&= EG^* + D\Phi^* - PV + \bar{V} \\
&= -(PV - (EG^* + D\Phi^*)) + \bar{V} \\
&= -R^* + \bar{V}
\end{aligned}$$

Now we are able to apply GMRES iterative method to solve G until it converges in (57). Finally, solve Φ using G from previous step with a fast Poisson solver in (47)

$$L\Phi = F_1 - BG$$

2.4.1 GENERALIZED MINIMAL RESIDUAL METHOD (GMRES)

The generalized minimal residual method (GMRES) is an iterative method for the numerical solution of a non-symmetric system of linear equations. The method approximates the solution by the vector in a Krylov subspace with minimal residual. The Arnoldi iteration is used to find this vector.

The GMRES method was developed by Yousef Saad and Martin H. Schultz in 1986 [27]. GMRES is a generalization of the minimal residual method (MINRES) developed by Chris Paige and Michael Saunders in 1975 [28]. GMRES also is a special case of the Direct Inversion of Iterative Space method (DIIS) developed by Peter Pulay in 1980 [29]. DIIS is also applicable to non-linear systems.

The system of equations to solved is

$$A\vec{x} = \vec{b} \tag{62}$$

where matrix A is assumed to be invertible of size m by m. Vector $\vec{b}$ is normalized with $||b|| = 1$.

The n-th Krylov subspace for above problem is

$$\mathbf{K_n} = \mathbf{K_n}(A,\vec{b}) = span\{\vec{b},A\vec{b},A^2\vec{b},...,A^{n-1}\vec{b}\} \tag{63}$$

GMRES approximate the exact solution of $Ax = b$ by the vector $\vec{x}_n \in \mathbf{K_n}$ that minimizes the Euclidean norm of the residual $\vec{r}_n = A\vec{x}_n - \vec{b}$, where the Euclidean norm of vector $\vec{r}_n$ is denoted by $||\vec{r}_n||$.

The vectors $\vec{b},A\vec{b},...,A^{n-1}\vec{b}$ might be close to linearly dependent. To avoid this situation, the Arnoldi iteration [30] is used to find orthonormal vectors $\vec{q}_1,\vec{q}_2,...,\vec{q}_n$ which form a basis for $\mathbf{K_n}$. Hence, the vector $\vec{x}_n \in \mathbf{K_n}$ can be written as $\vec{x}_n = Q_n\vec{y}_n$ with $\vec{y}_n \in \mathbb{R}_n$, where Q_n is the m-by-n matrix formed by $\vec{q}_1,\vec{q}_2,...,\vec{q}_n$.

The Arnoldi process also produces an $(n+1)$-by-n upper Hessenberg matrix H_n with

$$AQ_n = Q_{n+1}H_n \tag{64}$$

Because columns of Q_n are orthonormal, we have

$$||A\vec{x}_n - b|| = ||H_n\vec{y}_n - Q_{n+1}^T b|| = ||H_n\vec{y}_n - \beta e_1|| \tag{65}$$

where $e_1 = (1,0,0,...,0)^T$ is the first vector in the standard basis of $\mathbb{R}^{n+1}$ and $\beta = ||b - A\vec{x}_0||$. $\vec{x}_0$

is the first trial vector (usually zero). Hence $\vec{x}_n$ can be found by minimizing the Euclidean norm of the residual $\vec{r}_n = H_n\vec{y}_n - \beta_1$. This is a linear least squares problem of size n.

On the n-th iteration, the GMRES method is performed through the following steps

1. Calculate $\vec{q}_n$ by using Arnoldi method.
2. Find the $\vec{y}_n$ that minimizes $\|\vec{r}_n\|$.
3. Compute $\vec{x}_n = Q_n y_n$.
4. Repeat if the residual is not yet small enough.

2.4.2 WEIGHTED LEAST SQUARES APPROACH FOR COMPUTING UNKNOWN JUMP CONDITION IN TWO DIMENSIONAL

The crucial step in immersed interface method is to compute Φ_n^+ and Φ_n^- with the knowledge of Φ and the jump condition G. A weighted least squares approach was used in [26], the idea is to approximate quantities on the interface from a grid function. In current case, interpolate Φ_{ij} to the interface to get $\Phi_n^+(\mathbf{X_c})$ and $\Phi_n^-(\mathbf{X_c})$, where $\mathbf{X_c}$ is a Lagrangian point on the interface. The original approach was developed by Peskin's immersed interface method in [31]. However, his method is only first-order accurate and may smear out the solution near the interface.

Consider the continuous situation, let $\phi(x,y)$ be a piecewise smooth function, with discontinuities only along the interface. We wish to interpolate ϕ_{ij} to the interface to get approximations of the normal derivatives of $\phi_n^-(\mathbf{X_c})$ and $\phi_n^+(\mathbf{X_c})$ with second order accuracy.

The interpolation scheme for ϕ_n^- at the point $\mathbf{X_c}$ on the interface can be written as

$$\phi_n^-(\mathbf{X_c}) \approx \sum_{i,j} = \gamma_{ij}\phi(i,j)d_\alpha(|\mathbf{X_c} - \vec{\mathbf{x}}_{ij}|) - C \tag{66}$$

where N denotes a set of neighboring grid points near $\mathbf{X_c}$, and C is a correction term which can be determined once γ_{ij} are known. The distance function $d_\alpha(r)$ is defined as

$$d_\alpha(r) = \begin{cases} \frac{1}{2}(1+\cos(\pi r/\alpha)) & \text{if } r < \alpha \\ 0 & \text{if } r \geq \alpha \end{cases} \tag{67}$$

The coefficients γ_{ij} and correction term C can be computed based on immersed interface method in [24].

In immersed interface method, since the jump condition is given in the normal derivative of the solution, a local coordinates is used at the point $\mathbf{X_c} = (x_c, y_c)$

$$\begin{aligned} \xi &= (x-x_c)\cos(\theta)+(y-y_c)\sin(\theta) \\ \eta &= -(x-x_c)\sin(\theta)+(y-y_c)\cos(\theta) \end{aligned} \tag{68}$$

where θ is the angle between the x-axis and the normal direction. Under such new coordinate, the interface can be parameterized by

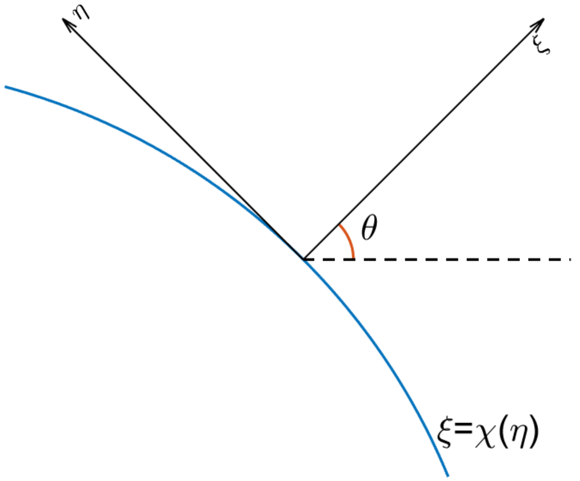

Figure. 11: Local $\eta - \xi$ coordinates transformation at the interface node.

$$\xi = \chi(\eta), \eta = \eta \text{ with } \chi(0) = 0, \chi'(0) = 0 \tag{69}$$

The interface jump conditions $[\phi] = w$ and $[\sigma\nabla\phi \cdot \mathbf{n}] = v$ are locally defined by

$$\phi^+ - \phi^- = w(\eta) \tag{70}$$

$$\sigma^+\frac{\partial\phi^+}{\partial n} - \sigma^-\frac{\partial\phi^-}{\partial n} = v(\eta) \tag{71}$$

Differentiate (70) with respect to η along the interface to get

$$[\phi_\xi]\chi' + [\phi_\eta] = w'(\eta) \tag{72}$$

Differentiate (72) with respect to η we obtain

$$[\phi_\xi]\chi'' + \chi'\frac{d}{d\eta}[\phi_\xi] + [\phi_{\xi\eta}]\chi' + [\phi_{\eta\eta}] = w''(\eta) \tag{73}$$

Another interface jump condition, $[\phi_n] = g$ is locally defined by

$$\phi_n^+ = \phi_n^- + g \tag{74}$$

At a point $(\eta, \chi(\eta)) \in \Gamma$, the normal derivative in terms of the derivatives of ξ- and η- is given by

$$\frac{\partial \phi}{\partial n} = \frac{1}{\sqrt{1+\chi'^2}}(\phi_\xi - \phi_\eta \chi') \tag{75}$$

And in the local coordinate system $\eta - \xi$, (74) can be written as

$$\phi_\xi^+ - \phi_\eta^+ \chi' = \phi_\xi^- - \phi_\eta^- \chi' + g\sqrt{1+(\chi')^2} \tag{76}$$

Differentiate (76) with respect to η along the interface we have the following relation

$$\begin{aligned}\phi_{\xi\xi}\chi' + \phi_{\xi\eta}^+ - \frac{d}{d\eta}(\phi_\eta^+)\chi' - \phi_\eta^+\chi'' =& \phi_{\xi\xi}^-\chi' + \phi_{\xi\eta}^- - \frac{d}{d\eta}(\phi_\eta^-)\chi' - \phi_\eta^-\chi'' \\ &+ g'(\eta)\Big(\sqrt{1+(\chi')^2} + \frac{g(\eta)\chi'\chi''}{\sqrt{1+(\chi')^2}}\Big)\end{aligned} \tag{77}$$

The Poisson equation $\nabla \cdot (\sigma \nabla \phi) = f$ remains unchanged if the coordinate transformation is composed of a shift and rotation as in (68), that is,

$$\phi_{xx} + \phi_{yy} = \frac{d}{d\eta}\Big(\frac{d\phi}{d\eta}\Big) + \frac{d}{d\xi}\Big(\frac{d\phi}{d\xi}\Big) = \frac{f}{\sigma} \quad \text{for constant } \sigma \tag{78}$$

We obtain the following **PDE** in Ω^+ and Ω^-, respectively

$$\phi^+_{\eta\eta} + \phi^+_{\xi\xi} = \frac{f^+}{\sigma^+} \tag{79}$$

$$\phi^-_{\eta\eta} + \phi^-_{\xi\xi} = \frac{f^-}{\sigma^-} \tag{80}$$

With $\chi(0) = 0$ and $\chi'(0) = 0$ at a fix point corresponding to $\xi = \eta = 0$ on the interface Σ, the solution of the equation (41) and (42) satisfy the following interface relations

$$\begin{array}{rcll} \phi^+ &=& \phi^- + w & \text{from (70)} \\ \phi^+_\xi &=& \phi^-_\xi + g & \text{from (74)} \\ \phi^+_\eta &=& \phi^-_\eta + w' & \text{from (72)} \\ \phi^+_{\xi\xi} &=& \phi^-_{\xi\xi} + g\chi'' - w'' + \left[\dfrac{f}{\sigma}\right] & \\ \phi^+_{\eta\eta} &=& \phi^-_{\eta\eta} - g\chi'' + w'' & \text{from (73)} \\ \phi^+_{\xi\eta} &=& \phi^-_{\xi\eta} + v'\chi'' + g' & \text{from (77)} \end{array} \tag{81}$$

where $w' = w_\eta$, $g' = g_\eta$, $\chi' = \chi_\eta$, $w'' = w_{\eta\eta}$ and $\chi'' = \chi_{\eta\eta}$. Let ξ_i, η_j be the $\xi - \eta$ coordinates of (x_i, y_j), then apply Taylor series to have

$$\phi(x_i, y_j) = \phi^\pm + \phi^\pm_\xi \xi_i + \phi^\pm_\eta \eta_j + \frac{1}{2}\phi^\pm_{\xi\xi}\xi_i^2 + \frac{1}{2}\phi^\pm_{\eta\eta}\eta_j^2 + \phi^\pm_{\xi\eta}\xi_i\eta_j + O(h^3) \tag{82}$$

where $+$ and $-$ sign depends on whether(ξ_i, η_j) lies on the $+$ or $-$ side of the interface Σ.

The Taylor expansion of (66) about $\mathbf{X_c}$ in the $\xi - \eta$ coordinate system is

$$\begin{aligned} \phi^-_n =& a_1\phi^- + a_2\phi^+ + a_3\phi^-_\xi + a_4\phi^+_\xi + a_5\phi^-_\eta + a_6\phi^+_\eta + a_7\phi^-_{\xi\xi} + a_8\phi^+_{\xi\xi} \\ &+ a_9\phi^-_{\eta\eta} + a_{10}\phi^+_{\eta\eta} + a_{11}\phi^-_{\xi\eta} + a_{12}\phi^-_{\xi\eta} - C + O(h^3\max|\gamma_{ij}|) \\ =& (a_1 + a_2)\phi^- + (a_3 + a_4)\phi^-_\xi + (a_5 + a_6)\phi^-_\eta + (a_7 + a_8)\phi^-_{\xi\xi} \\ &+ (a_9 + a_{10})\phi^-_{\eta\eta} + (a_{11} + a_{12})\phi^-_{\xi\eta} - C + O(h^3\max|\gamma_{ij}|) \end{aligned} \tag{83}$$

Define the index sets K^- and K^+ by $K^\pm = \{k : (\xi_k, \eta_k)$ is on the $\pm$ side of $\Gamma\}$, wthen the coefficients $a_k{}'s$ are given by

$$
\begin{aligned}
a_1 &= \sum_{(x_i,y_j)\in\Omega^-} \gamma_{ij} d_\alpha(|\mathbf{X_c} - \vec{\mathbf{x}}_{ij}|) & a_2 &= \sum_{(x_i,y_j)\in\Omega^+} \gamma_{ij} d_\alpha(|\mathbf{X_c} - \vec{\mathbf{x}}_{ij}|) \\
a_3 &= \sum_{(x_i,y_j)\in\Omega^-} \xi_k \gamma_{ij} d_\alpha(|\mathbf{X_c} - \vec{\mathbf{x}}_{ij}|) & a_4 &= \sum_{(x_i,y_j)\in\Omega^+} \xi_k \gamma_{ij} d_\alpha(|\mathbf{X_c} - \vec{\mathbf{x}}_{ij}|) \\
a_5 &= \sum_{(x_i,y_j)\in\Omega^-} \eta_k \gamma_{ij} d_\alpha(|\mathbf{X_c} - \vec{\mathbf{x}}_{ij}|) & a_6 &= \sum_{(x_i,y_j)\in\Omega^+} \eta_k \gamma_{ij} d_\alpha(|\mathbf{X_c} - \vec{\mathbf{x}}_{ij}|) \\
a_7 &= \sum_{(x_i,y_j)\in\Omega^-} \frac{1}{2}\xi_k^2 \gamma_{ij} d_\alpha(|\mathbf{X_c} - \vec{\mathbf{x}}_{ij}|) & a_8 &= \sum_{(x_i,y_j)\in\Omega^+} \frac{1}{2}\xi_k^2 \gamma_{ij} d_\alpha(|\mathbf{X_c} - \vec{\mathbf{x}}_{ij}|) \\
a_9 &= \sum_{(x_i,y_j)\in\Omega^-} \frac{1}{2}\eta_k^2 \gamma_{ij} d_\alpha(|\mathbf{X_c} - \vec{\mathbf{x}}_{ij}|) & a_{10} &= \sum_{(x_i,y_j)\in\Omega^+} \frac{1}{2}\eta_k^2 \gamma_{ij} d_\alpha(|\mathbf{X_c} - \vec{\mathbf{x}}_{ij}|) \\
a_{11} &= \sum_{(x_i,y_j)\in\Omega^-} \xi_k \eta_k \gamma_{ij} d_\alpha(|\mathbf{X_c} - \vec{\mathbf{x}}_{ij}|) & a_{12} &= \sum_{(x_i,y_j)\in\Omega^+} \xi_k \eta_k \gamma_{ij} d_\alpha(|\mathbf{X_c} - \vec{\mathbf{x}}_{ij}|)
\end{aligned}
\tag{84}
$$

From the interface relations (69), the algorithm requires the coefficients of ϕ^-, ϕ^-_η, $\phi^-_{\xi\xi}$, $\phi^-_{\eta\eta}$ and $\phi^-_{\xi\eta}$ to vanish, and $\phi^-_n = \phi^-_\xi$, we obtain the linear system of equations for the coefficients γ_{ij}

$$
\begin{aligned}
a_1 + a_2 &= 0 \\
a_3 + a_4 &= 1 \\
a_5 + a_6 &= 0 \\
a_7 + a_8 &= 0 \\
a_9 + a_{10} &= 0 \\
a_{11} + a_{12} &= 0
\end{aligned}
\tag{85}
$$

A second order approximate to the normal derivative ϕ^-_n at $\mathbf{X_c}$ can be achieved by choosing an appropriate correction term C, and the discontinuities across the interface only contribute to the correction term C. The detailed analysis can be found in [24, 25] for Poisson equations with discontinuous, where the five points stencil is used by adding a correction term to the source term at irregular grid point.

The $a_k{}'s$ are obtained once the coefficients $\gamma_{ij}{}'s$ are computed, and the correction term C is determined by

$$\begin{aligned} C =& a_2 w + a_4 g + a_6 w' + a_8 \left(g\chi'' - w'' + \left[\frac{f}{\sigma} \right] \right) \\ & + a_{10}(w'' - g\chi'') + a_{12}(w'\chi'' + g') \end{aligned} \tag{86}$$

which guarantee the computation of ϕ_n^- to the second order accuracy. With the relation $\phi_n^+ = \phi_n^- + g$, we can get a second order accuracy interpolation scheme for ϕ_n^+ immediately

$$\phi_n^+(\mathbf{X_c}) \approx \sum_{i,j} = \gamma_{ij}\phi(i,j) d_\alpha(|\mathbf{X_c} - \vec{\mathbf{x}}_{ij}|) - C + g \tag{87}$$

where $\gamma_{ij}{}'s$ are the solutions we computed for ϕ_n^-.

2.4.3 WEIGHTED LEAST SQUARES APPROACH FOR COMPUTING UNKOWN JUMP CONDITION IN THREE DIMENSIONAL

The interpolation scheme for ϕ_n^- at the point $\mathbf{X_c}$ on the interface can be written as

$$\phi_n^-(\mathbf{X_c}) \approx \sum_{i,j,K} = \gamma_{ijk}\phi(i,j,k) d_\alpha(|\mathbf{X_c} - \vec{\mathbf{x}}_{ijk}|) - C \tag{88}$$

where N denotes a set of neighboring grid points near $\mathbf{X_c}$, and C is a correction term which can be determined once γ_{ijk} are known. A local coordinates is used at the point $\mathbf{X_c} = (x_c, y_c, z_c)$

$$\begin{aligned} \xi &= (x - x_c)\alpha_{x\xi} + (y - y_c)\alpha_{y\xi} + (z - z_c)\alpha_{z\xi} \\ \eta &= (x - x_c)\alpha_{x\eta} + (y - y_c)\alpha_{y\eta} + (z - z_c)\alpha_{z\eta} \\ \tau &= (x - x_c)\alpha_{x\tau} + (y - y_c)\alpha_{y\tau} + (z - z_c)\alpha_{z\tau} \end{aligned} \tag{89}$$

where $\alpha_{x\xi}$ represents the directional cosine between the x-axis and ξ, and so forth. The three-dimensional coordinate transformation above can also be written in matrix-vector form. Define the local transformation matrix as

$$A = \begin{bmatrix} \alpha_{x\xi} & \alpha_{y\xi} & \alpha_{z\xi} \\ \alpha_{x\eta} & \alpha_{y\eta} & \alpha_{z\eta} \\ \alpha_{x\tau} & \alpha_{y\tau} & \alpha_{z\tau} \end{bmatrix}$$

and the local coordinates transformation becomes

$$\begin{bmatrix} \xi \\ \eta \\ \tau \end{bmatrix} = A \begin{bmatrix} (x - x*) \\ (y - y*) \\ (z - z*) \end{bmatrix}$$

Also, for any differentiable function $p(x,y,z)$, we have

$$\begin{bmatrix} \hat{p}_\xi \\ \hat{p}_\eta \\ \hat{p}_\tau \end{bmatrix} = A \begin{bmatrix} p_x \\ p_y \\ p_z \end{bmatrix}$$

$$\begin{bmatrix} \hat{p}_{\xi\xi} & \hat{p}_{\xi\eta} & \hat{p}_{\xi\tau} \\ \hat{p}_{\eta\xi} & \hat{p}_{\eta\eta} & \hat{p}_{\eta\tau} \\ \hat{p}_{\tau\xi} & \hat{p}_{\tau\eta} & \hat{p}_{\tau\tau} \end{bmatrix} = A \begin{bmatrix} p_{xx} & p_{xy} & p_{xz} \\ p_{yx} & p_{yy} & p_{yz} \\ p_{zx} & p_{zy} & p_{zz} \end{bmatrix} A^T$$

where $\hat{p}(\xi,\eta,\tau) = p(x,y,z)$ and A^T is the transpose of A. It can proved that $A^T A = I$, and under the local coordinates transformation, the PDE (5) is invariant. Hence the hat in difference vector and matrix can be dropped for simplicity. Under the local $\xi - \eta - \tau$ coordinate system, the interface can be parameterized by

$$\xi = \chi(\eta,\tau) \text{ with } \chi(0,0) = 0, \chi_\eta(0,0) = 0, \chi_\tau(0,0) = 0 \tag{90}$$

The solution of the equation (41) and (42) satisfy the following interface relations

$$
\begin{aligned}
\phi^{+} &= \phi^{-} + w \\
\phi^{+}_{\xi} &= \phi^{-}_{\xi} + g \\
\phi^{+}_{\eta} &= \phi^{-}_{\eta} + w_{\eta} \\
\phi^{+}_{\tau} &= \phi^{-}_{\tau} + w_{\tau} \\
\phi^{+}_{\eta\tau} &= \phi^{-}_{\eta\tau} - g\chi_{\eta\tau} + w_{\eta\tau} \\
\phi^{+}_{\eta\eta} &= \phi^{-}_{\tau\tau} - g\chi_{\eta\eta} + w_{\eta\eta} \\
\phi^{+}_{\eta\tau} &= \phi^{-}_{\eta\tau} - g\chi_{\tau\tau} + w_{\tau\tau} \\
\phi^{+}_{\xi\eta} &= \phi^{-}_{\xi\eta} + w_{\eta}\chi_{\eta\eta} + w_{\tau}\chi_{\eta\tau} + g_{\eta} \\
\phi^{+}_{\xi\tau} &= \phi^{-}_{\xi\tau} + w_{\eta}\chi_{\eta\tau} + w_{\tau}\chi_{\tau\tau} + g_{\tau} \\
\phi^{+}_{\xi\xi} &= \phi^{-}_{\xi\xi} + g(\chi_{\eta\eta} + \chi_{\tau\tau}) + \left[\frac{f}{\beta}\right] - w_{\eta\eta} - w_{\tau\tau}
\end{aligned}
\tag{91}
$$

Let ξ_i, η_j, τ_k be the $\xi - \eta - \tau$ coordinates of (x_i, y_j, z_k), then apply Taylor series to have

$$
\begin{aligned}
\phi(x_i, y_j, z_k) = & \phi^{\pm} + \phi^{\pm}_{\xi}\xi_i + \phi^{\pm}_{\eta}\eta_j + \phi^{\pm}_{\tau}\tau_j + \frac{1}{2}\phi^{\pm}_{\xi\xi}\xi_i^2 + \frac{1}{2}\phi^{\pm}_{\eta\eta}\eta_j^2 + \frac{1}{2}\phi^{\pm}_{\tau\tau}\tau_k^2 \\
& + \phi^{\pm}_{\xi\eta}\xi_i\eta_j + \phi^{\pm}_{\xi\tau}\xi_i\tau_k + \phi^{\pm}_{\eta\tau}\eta_i\tau_k + O(h^3)
\end{aligned}
$$

where $+$ and $-$ sign depends on whether(ξ_i, η_j) lies on the $+$ or $-$ side of the interface Σ.

The Taylor expansion of (88) about $\mathbf{X_c}$ in the $\xi-\eta-\tau$ coordinate system is

$$\begin{aligned}\phi_n^- =& a_1\phi^- + a_2\phi^+ + a_3\phi_\xi^- + a_4\phi_\xi^+ + a_5\phi_\eta^- + a_6\phi_\eta^+ + a_7\phi_\tau^- + a_8\phi_\tau^+ \\ & + a_9\phi_{\xi\xi}^- + a_{10}\phi_{\xi\xi}^+ + a_{11}\phi_{\eta\eta}^- + a_{12}\phi_{\eta\eta}^+ + a_{13}\phi_{\tau\tau}^- + a_{14}\phi_{\tau\tau}^+ \\ & + a_{15}\phi_{\xi\eta}^- + a_{16}\phi_{\xi\eta}^+ + a_{17}\phi_{\xi\tau}^- + a_{18}\phi_{\xi\tau}^+ + a_{19}\phi_{\eta\tau}^- + a_{20}\phi_{\eta\tau}^+ \\ & - C + O(h^3\max|\gamma_{ijk}|) \\ =&(a_1+a_2)\phi^- + (a_3+a_4)\phi_\xi^- + (a_5+a_6)\phi_\eta^- + (a_7+a_8)\phi_\tau^- \\ & + (a_9+a_{10})\phi_{\xi\xi}^- + (a_{11}+a_{12})\phi_{\eta\eta}^- + (a_{13}+a_{14})\phi_{\tau\tau}^- \\ & + (a_{15}+a_{16})\phi_{\xi\eta}^- + (a_{17}+a_{18})\phi_{\xi\tau}^- + (a_{19}+a_{20})\phi_{\eta\tau}^- \\ & + a_2[\phi] + a_4[\phi_\xi] + a_6[\phi_\eta] + a_8[\phi_\tau] + a_{10}[\phi_{\xi\xi}] + a_{12}[\phi_{\eta\eta}] + a_{14}[\phi_{\tau\tau}] \\ & + a_{16}[\phi_{\xi\eta}] + a_{18}[\phi_{\xi\tau}] + a_{20}[\phi_{\eta\tau}] - C + O(h^3\max|\gamma_{ijk}|) \end{aligned} \tag{92}$$

Define the index sets K^- and K^+ by $K^{\pm} = \{k : (\xi_k, \eta_k, \tau_k)$ is on the $\pm$ side of $\Gamma\}$, where the coefficients $a_k's$ are given by

$$\begin{aligned}
a_1 &= \sum_{k\in K^-} \gamma_{ijk} d_\alpha(|\mathbf{X_c} - \vec{\mathbf{x}}_{ijk}|) & a_2 &= \sum_{k\in K^+} \gamma_{ijk} d_\alpha(|\mathbf{X_c} - \vec{\mathbf{x}}_{ijk}|) \\
a_3 &= \sum_{k\in K^-} \xi_k \gamma_{ijk} d_\alpha(|\mathbf{X_c} - \vec{\mathbf{x}}_{ijk}|) & a_4 &= \sum_{k\in K^+} \xi_k \gamma_{ijk} d_\alpha(|\mathbf{X_c} - \vec{\mathbf{x}}_{ijk}|) \\
a_5 &= \sum_{k\in K^-} \eta_k \gamma_{ijk} d_\alpha(|\mathbf{X_c} - \vec{\mathbf{x}}_{ijk}|) & a_6 &= \sum_{k\in K^+} \eta_k \gamma_{ijk} d_\alpha(|\mathbf{X_c} - \vec{\mathbf{x}}_{ijk}|) \\
a_7 &= \sum_{k\in K^-} \tau_k \gamma_{ijk} d_\alpha(|\mathbf{X_c} - \vec{\mathbf{x}}_{ijk}|) & a_8 &= \sum_{k\in K^+} \tau_k \gamma_{ijk} d_\alpha(|\mathbf{X_c} - \vec{\mathbf{x}}_{ijk}|) \\
a_9 &= \sum_{k\in K^-} \frac{1}{2}\xi_k^2 \gamma_{ijk} d_\alpha(|\mathbf{X_c} - \vec{\mathbf{x}}_{ijk}|) & a_{10} &= \sum_{k\in K^+} \frac{1}{2}\xi_k^2 \gamma_{ijk} d_\alpha(|\mathbf{X_c} - \vec{\mathbf{x}}_{ijk}|) \\
a_{11} &= \sum_{k\in K^-} \frac{1}{2}\eta_k^2 \gamma_{ijk} d_\alpha(|\mathbf{X_c} - \vec{\mathbf{x}}_{ijk}|) & a_{12} &= \sum_{k\in K^+} \frac{1}{2}\eta_k^2 \gamma_{ijk} d_\alpha(|\mathbf{X_c} - \vec{\mathbf{x}}_{ijk}|) \\
a_{13} &= \sum_{k\in K^-} \frac{1}{2}\tau_k^2 \gamma_{ijk} d_\alpha(|\mathbf{X_c} - \vec{\mathbf{x}}_{ijk}|) & a_{14} &= \sum_{k\in K^+} \frac{1}{2}\tau_k^2 \gamma_{ijk} d_\alpha(|\mathbf{X_c} - \vec{\mathbf{x}}_{ijk}|) \\
a_{15} &= \sum_{k\in K^-} \xi_k \eta_k \gamma_{ijk} d_\alpha(|\mathbf{X_c} - \vec{\mathbf{x}}_{ijk}|) & a_{16} &= \sum_{k\in K^+} \xi_k \eta_k \gamma_{ijk} d_\alpha(|\mathbf{X_c} - \vec{\mathbf{x}}_{ijk}|) \\
a_{17} &= \sum_{k\in K^-} \xi_k \tau_k \gamma_{ijk} d_\alpha(|\mathbf{X_c} - \vec{\mathbf{x}}_{ijk}|) & a_{18} &= \sum_{k\in K^+} \xi_k \tau_k \gamma_{ijk} d_\alpha(|\mathbf{X_c} - \vec{\mathbf{x}}_{ijk}|) \\
a_{19} &= \sum_{k\in K^-} \eta_k \tau_k \gamma_{ijk} d_\alpha(|\mathbf{X_c} - \vec{\mathbf{x}}_{ijk}|) & a_{20} &= \sum_{k\in K^+} \eta_k \tau_k \gamma_{ijk} d_\alpha(|\mathbf{X_c} - \vec{\mathbf{x}}_{ijk}|)
\end{aligned} \tag{93}$$

From the interface relations (90), the algorithm requires the coefficients of ϕ^-, ϕ_η^-, ϕ_τ^-, $\phi_{\xi\xi}^-$, $\phi_{\eta\eta}^-$, $\phi_{\tau\tau}^-$, $\phi_{\xi\eta}^-$, $\phi_{\xi\tau}^-$ and $\phi_{\eta\tau}^-$ to vanish, and $\phi_n^- = \phi_\xi^-$, we obtain the linear system of equations for the coefficients γ_{ijk}

$$\begin{aligned}
a_1 + a_2 &= 0 \\
a_3 + a_4 &= 1 \\
a_5 + a_6 &= 0 \\
a_7 + a_8 &= 0 \\
a_9 + a_{10} &= 0 \\
a_{11} + a_{12} &= 0 \\
a_{13} + a_{14} &= 0 \\
a_{15} + a_{16} &= 0 \\
a_{17} + a_{18} &= 0 \\
a_{19} + a_{20} &= 0
\end{aligned} \tag{94}$$

A second order approximate to the normal derivative ϕ_n^- at $\mathbf{X_c}$ can be achieved by choosing an appropriate correction term C, and the discontinuities across the interface only contribute to the correction term C. The detailed analysis can be found in [32] for Poisson equations with discontinuous, where the 27 grid points stencil is used for three dimensions unless otherwise specified. The system is under-determined and in general there are infinite many solutions. A SVD subroutine is used to solve such a system. The $a_k{}'s$ are obtained once the coefficients $\gamma_{ijk}{}'s$ are computed, and the correction term C is determined by

$$\begin{aligned}
C =& a_2[\phi] + a_4[\phi_\xi] + a_6[\phi_\eta] + a_8[\phi_\tau] + a_{10}[\phi_{\xi\xi}] \\
&+ a_{12}[\phi_{\eta\eta}] + a_{14}[\phi_{\tau\tau}] + a_{16}[\phi_{\xi\eta}] + a_{18}[\phi_{\xi\tau}] + a_{20}[\phi_{\eta\tau}] \\
=& a_2 w + a_4 g + a_6 w_\eta + a_8 w_\tau + a_{10}\left\{ g(\chi_{\eta\eta} + \chi_{\tau\tau}) + \left[\frac{f}{\sigma}\right] - w_{\eta\eta} - w_{\tau\tau} \right\} \\
&+ a_{12}(w_{\eta\eta} - g\chi_{\eta\eta}) + a_{14}(w_{\tau\tau} - g\chi_{\tau\tau}) + a_{16}(w_\tau \chi_{\eta\eta} + w_\tau \chi_{\eta\tau} + g_\eta) \\
&+ a_{18}(w_\eta \chi_{\eta\tau} + w_\tau \chi_{\tau\tau} + g_\tau) + a_{20}(w_{\eta\tau} - g\chi_{\eta\tau})
\end{aligned} \tag{95}$$

which guarantee the computation of ϕ_n^- to the second order accuracy. With the relation $\phi_n^+ =$

$u_n^- + g$, we can get a second order accuracy interpolation scheme for ϕ_n^+ immediately

$$\phi_n^+(\mathbf{X_c}) \approx \sum_{i,j,k} = \gamma_{ijk}\phi(i,j,k)d_\alpha(|\mathbf{X_c} - \vec{\mathbf{x}}_{ijk}|) - C + g \tag{96}$$

where $\gamma_{ijk}'s$ are the solutions we computed for ϕ_n^-.

2.4.4 COMPUTATION OF ELECTRIC FIELD

After calculating the scalar potential ϕ, the electric field $\mathbf{E} = (\phi_x, \phi_y)$ is computed through finite difference scheme. At a regular point, ϕ_x and ϕ_y are computed by the standard centered difference shceme as

$$\phi_x(i,j) = \frac{\phi(i+1,j) - \phi(i-1,j)}{2\Delta x}$$

and

$$\phi_y(i,j) = \frac{\phi(i,j+1) - \phi(i,j-1)}{2\Delta y}$$

For irregular point, ϕ_x and ϕ_y are computed by one-side difference interpolation. For example, when (x_i, y_j), $(x_{i-1}, y_j) \in \Omega^-$ and $(x_{i+1}, y_j) \in \Omega$,

$$\phi_x(i,j) = \frac{\phi(i,j) - \phi(i-1,j)}{\Delta x}$$

2.5 NUMERICAL EXAMPLES

Example 1

This is exactly same as 2.3.5, we can compare the results given by correction function method and immersed interface method.

Consider $\nabla \cdot (\sigma\phi) = 0$ in two dimensions on $[-1,1] \times [-1,1]$ with the interface defined by the circle $x^2 + y^2 = 0.5^2$. In this example, $\sigma^+ = \sigma^- = 1$. The jump conditions on the interface is $[\phi] = 0$ and $[\phi_n] = 2$, with Dirichlet boundary conditions $1 + \log(2\sqrt{X^2 + Y^2})$, $(X,Y) \in \partial\Omega$ at boundary, directly computed from the exact solution. The Lagrangian control points are 140 on the immersed interface. The exact solution is

$$u(x,y)=\begin{cases}1+\log(2\sqrt{x^2+y^2}), & (x,y)\in\Omega^+\\ 1, & (x,y)\in\Omega^-\end{cases}$$

Table 3 shows the numerical accuracy and convergence tests.

TABLE 3: Accuracy and convergence test for Example 3

N	L^∞ error in ϕ	ratio	order
20	$1.233E-03$		
40	$3.437E-04$	3.58743	1.84295
80	$1.070E-04$	3.21215	1.68354
160	$3.110E-05$	3.44051	1.78262
320	$6.560E-06$	4.74085	2.24515

The Figure 12 demonstrates the convergence rate of two methods, the Correction Function Method and Immersed Interface Method. The two methods are both 2nd order convergent and have quite closed numerical errors. In the following examples, we will examine the convergence rate of immersed interface method for different σ^+ and σ^-.

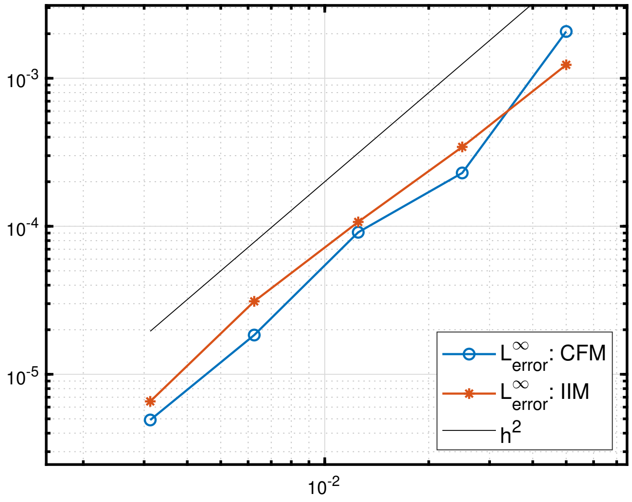

Figure. 12: comparison of correction function method and immersed interface method.

Example 2

This example is taken from [33]. Consider $\nabla \cdot (\sigma \nabla \phi) = f(x,y)$ in two dimensions on $[-1,1] \times [-1,1]$ with the interface defined by the circle $(x-0.5)^2 + (y-0.5)^2 = 0.25^2$. The exact solution are given as

$$\phi(x,y) = \begin{cases} e^{-x^2-y^2}, & \text{in } \Omega^- \text{ and } \sigma^- = 1 \\ 0, & \text{in } \Omega^+ \text{ and } \sigma^+ = 2 \end{cases}$$

and $f(x,y) = 8(x^2+y^2-1)e^{-x^2-y^2}$ in Ω^- and $f(x,y) = 0$ in Ω^+, respectively. The jump conditions across the interface Σ separating Ω^+ and Ω^- are $[\phi] = -e^{-x^2-y^2}$ and $[\sigma\phi_n] = 8(2x^2+2y^2-x-y)e^{-x^2-y^2}$. The Lagrangian control points are 140 on the immersed interface. The appropriate Dirichlet boundary conditions are specified at $\partial\Omega$. Table 4 shows the numerical accuracy and convergence tests.

TABLE 4: Accuracy and convergence test for Example 2

N	L^∞ error in ϕ	ratio	order	Iter.
20	$1.368E-03$			31
40	$3.075E-04$	4.44878	2.15341	17
80	$7.046E-05$	4.36418	2.12571	12
160	$1.644E-05$	4.28589	2.09959	8
320	$4.112E-06$	3.99805	1.99930	7

Example 3

This example is taken from [25]. Consider $\nabla \cdot (\sigma \nabla \phi) = f(x,y)$ in two dimensions on $[-1,1] \times [-1,1]$ with the interface defined by the circle $x^2 + y^2 = 0.5^2$. The exact solution are given as

$$\phi(x,y) = \begin{cases} \dfrac{x^2+y^2}{\sigma^-}, & \text{in } \Omega^- \\ \\ \dfrac{(x^2+y^2)^2 - 0.1\log(2\sqrt{x^2+y^2})}{\sigma^+} + \left(\dfrac{0.5^2}{\sigma^-} - \dfrac{0.5^4}{\sigma^+}\right), & \text{in } \Omega^+ \end{cases}$$

and the source term $f(x,y)$ is determined accordingly from exact solution

$$f(x,y) = \begin{cases} \dfrac{4}{\sigma^-}, & \text{in } \Omega^- \\ \\ \dfrac{16(x^2+y^2)}{\sigma^+}, & \text{in } \Omega^+ \end{cases}$$

One can determine that the solution is continuous everywhere which indicates that $[\phi] = 0$ across the interface Σ separating Ω^+ and Ω^-. The flux jump condition is $[\sigma\phi_n] = -0.7$. This can be verified from exact solution as well. The Lagrangian control points are 140 on the immersed interface. The appropriate Dirichlet boundary conditions are specified at $\partial\Omega$. We investigated the following two cases.

- Case A. The parameters are taken with $\sigma^- = 1$ and $\sigma^+ = 10$.Table 5 shows the numerical accuracy and convergence tests.

TABLE 5: Accuracy and convergence test for Example 3-A

N	L^∞ error in ϕ	ratio	order	Iter.
20	$7.079E-03$			59
40	$1.601E-03$	4.42161	2.14457	32
80	$3.681E-04$	4.34936	2.12080	17
160	$8.894E-05$	4.13875	2.04919	9
320	$2.053E-05$	4.33220	2.11510	7

- Case B. The parameters are taken with $\sigma^- = 1$ and $\sigma^+ = 100$. Table 6 shows the numerical accuracy and convergence tests.

TABLE 6: Accuracy and convergence test for Example 3-B

N	L^∞ error in ϕ	ratio	order	Iter.
20	$1.573E-03$			61
40	$3.553E-04$	4.42724	2.14641	38
80	$8.240E-05$	4.31189	2.10832	20
160	$1.949E-05$	4.22781	2.07991	10
320	$4.136E-06$	4.71228	2.23643	7

From example 3, we can observe that fast immersed interface method converges very well for small ratio of $\frac{\sigma^-}{\sigma^+}$. The error in the solution is even much smaller with small ratio. This phenomenon has

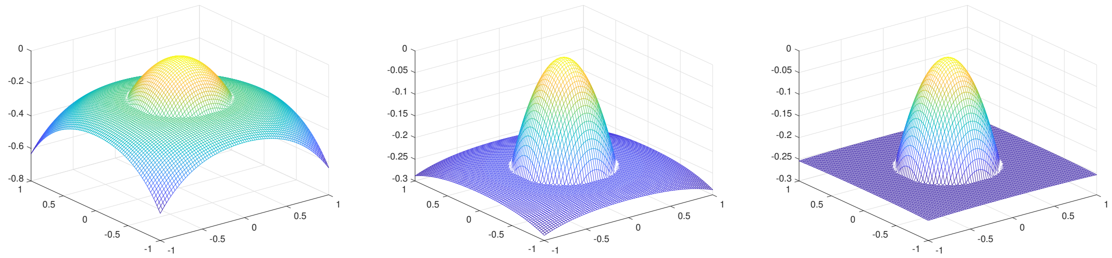

Figure. 13: The numerical solution ϕ of example 3 for grid size $N = 80$ with $\frac{\sigma^-}{\sigma^+} = \frac{1}{10}$, $\frac{\sigma^-}{\sigma^+} = \frac{1}{100}$ and $\frac{\sigma^-}{\sigma^+} = \frac{1}{1000}$, respectively.

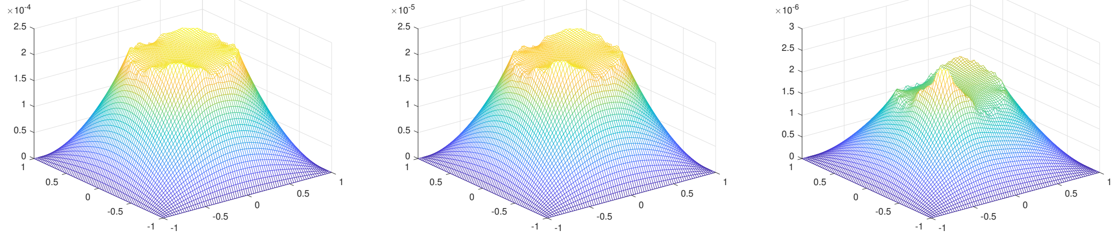

Figure. 14: The error distribution of example 3 for grid size $N = 80$ with $\frac{\sigma^-}{\sigma^+} = \frac{1}{10}$, $\frac{\sigma^-}{\sigma^+} = \frac{1}{100}$, and $\frac{\sigma^-}{\sigma^+} = \frac{1}{1000}$, respectively.

been addressed in [25]. Because the solution in Ω^+ approaches a constant as σ^+ becomes large and it's quadratic in Ω^-. A second order accurate method would give high accurate solution in both regions. See Figure 13 and Figure 14 for comparison results of numerical solutions and errors for the ratio of $\frac{\sigma^-}{\sigma^+} = \frac{1}{10}$, $\frac{\sigma^-}{\sigma^+} = \frac{1}{100}$, and $\frac{\sigma^-}{\sigma^+} = \frac{1}{1000}$.

Example 4

Consider $\nabla \cdot (\sigma \nabla \phi) = 0$ in two dimensions on $[-1,1] \times [-1,1]$ with the interface defined by the circle $x^2 + y^2 = 0.5^2$. The exact solution is

$$\phi(x,y) = \begin{cases} e^x \cos(y), & \text{for } (x,y) \in \Omega^- \\ 0, & \text{for } (x,y) \in \Omega^+ \end{cases}$$

The jump conditions are $[\phi] = -e^x\cos(y)$ and $[\phi_n] = 2e^x(y\sin(y) - x\cos(y))$. Table 7 shows the numerical accuracy and convergence tests.

TABLE 7: Accuracy and convergence test for Example 4

N	L^∞ error in ϕ	ratio	order
20	$3.170E-04$		
40	$7.386E-05$	4.29190	2.10162
80	$2.056E-05$	3.59241	1.84495
160	$5.564E-06$	3.69518	1.88565
320	$1.380E-06$	4.03188	2.01145

Example 5

We consider a problem with a piecewise constant coefficient σ and a discontinuous source term f in three dimensions. The interface is a sphere $x^2+y^2+z^2 = r_0^2$, where $r_0 = 0.5$. The differential equation is

$$(\sigma\phi_x)_x + (\sigma\phi_y)_y + (\sigma\phi_z)_z = f$$

with

$$\sigma(x,y,z) = \begin{cases} \sigma^-, & \text{if } r < \frac{1}{2} \\ \sigma^-, & \text{if } r \geq \frac{1}{2} \end{cases}$$

$$f(x,y,z) = \begin{cases} -200\sigma^- r^2, & \text{if } r < \frac{1}{2} \\ 20\sigma^+ r^2, & \text{if } r \geq \frac{1}{2} \end{cases}$$

Dirichlet boundary conditions and the jump conditions are determined from the exact solution

$$\phi(x,y,z) = \begin{cases} -10r^4, & \text{if } r < \frac{1}{2} \\ r^4, & \text{if } r \geq \frac{1}{2} \end{cases}$$

$$\|\phi\| = 11r_0^4 = \frac{11}{16}$$

$$\|\sigma\phi_n\| = 4(10\sigma^- + \sigma^+)r_0^3 = \frac{(10\sigma^- + \sigma^+)}{2}$$

where $r = \sqrt{x^2+y^2+z^2}$ and on the interface, $r = r_0 = 1/2$. Two cases are tested for different combinations of σ^- and σ^+.

TABLE 8: Accuracy and convergence test for $\sigma^- = 1$ and $\sigma^+ = 2$

N	L^∞ error in ϕ	ratio	order
26	$1.994E-02$		
52	$4.888E-03$	4.07938	2.02835
104	$1.230E-03$	3.97398	1.99058

TABLE 9: Accuracy and convergence test for $\sigma^- = 1$ and $\sigma^+ = 1000$

N	L^∞ error in ϕ	ratio	order
26	$3.283E-02$		
52	$9.604E-03$	3.41837	1.77331
104	$2.369E-03$	4.05403	2.01936

CHAPTER 3

NUMERICAL ALGORITHM FOR ELECTROHYDRODYNAMICS

3.1 FLUID FLOW

In present work, lattice Boltzmann method is used to model the fluid flow. The lattice Boltzmann method is a kinetic-based method and derived from the Boltzmann equation. Within the low Mach region, lattice Boltzmann method exhibits stability that exceeds many traditional methods [34]. The governing equation of lattice Boltzmann method in discrete form is as follows

$$\mathbf{f}(\mathbf{x}_j+\mathbf{c}\delta_t,t_n+\delta_t)-\mathbf{f}(\mathbf{x}_j,t_n)=-\mathbf{M}^{-1}\hat{S}[\mathbf{m}(\mathbf{x}_j,t_n)-\mathbf{m}^{(eq)}(\mathbf{x}_j,t_n)] \tag{97}$$

where $f_i(\mathbf{x}_j,t_n)$ represents the distribution of particles at $\mathbf{x}_j$ with velocity $\mathbf{c}_i$ at time t_n

$$\begin{aligned}&\mathbf{f}(\mathbf{x}_j+\mathbf{c}\delta_t,t_n+\delta_t)\\=&(\mathbf{f}_0(\mathbf{x}_j,t_n+\delta_t),\mathbf{f}_1(\mathbf{x}_j+\mathbf{c}_1\delta_t,t_n+\delta_t),...,\mathbf{f}_{Q-1}(\mathbf{x}_j+\mathbf{c}_{Q-1}\delta_t,t_n+\delta_t))^T\end{aligned}$$

and

$$\mathbf{f}(\mathbf{x}_j,t_n)=(\mathbf{f}_0(\mathbf{x}_j,t_n),\mathbf{f}_1(\mathbf{x}_j,t_n),...,\mathbf{f}_{Q-1}(\mathbf{x}_j,t_n))^T$$

$\mathbf{m}$ and $\mathbf{m}^{(eq)}$ represent the velocity moments, and the equilibrium moments, respectively [35]. The matrix $\mathbf{M}$ maps from probability distribution space into moment space

$$\mathbf{m}=\mathbf{M^{-1}}\cdot\mathbf{f}$$

and $\hat{S}$ is the diagonal matrix of relaxation rates $[s_0,s_1,...,s_{Q-1}]$.

The evolution of lattice Boltzmann method therefore consist of two steps: collision and streaming. With the multiple relaxation time (MRT) approximation, as represented on the right side of (97), probabilities $\mathbf{f}$ at each lattice node $\mathbf{x}_j$ are mapped to their moment space by the matrix $\mathbf{M}$. Within this moment space, the non-conserved moments $\mathbf{m}(\mathbf{x}_j,t_n)$ relax toward their equilibria

$\mathbf{m}^{(eq)}(\mathbf{x}_j, t_n)$, according to their specified relaxation parameters s_i on the diagonal of matrix $\mathbf{S}$. After this relaxation, the moments are mapped by the matrix $\mathbf{M}^{-\mathbf{1}}$ back to the probability distribution space.

In the two dimensional simulation, the D2Q9 model using a square lattice with nine velocities is employed. The D3Q19 model is one of the commonly used models in three-dimensional simulation. The integers 'D' and 'Q' denote the number of spatial dimensions and number of discrete velocities, respectively.

3.1.1 TWO DIMENSIONAL LATTICE BOLTZMANN MODEL

Followed by [36, 34], the discrete lattice velocities in D2Q9 model can be compactly formulated as

$$\mathbf{c}_i = \begin{cases} (0,0) & \text{for } i = 0 \\ \left(\cos\frac{(i-1)\pi}{2}, \sin\frac{(i-1)\pi}{2}\right) & \text{for } i = 1,4 \\ \sqrt{2}\left(\cos\frac{(2i-9)\pi}{4}, \sin\frac{(2i-9)\pi}{4}\right) & \text{for } i = 5,8 \end{cases} \tag{98}$$

There are nine moments $\mathbf{m} = (\delta\rho, e, \varepsilon, j_x, q_x, j_y, q_y, p_{xx}, p_{xy})^T$ corresponding to the nine discrete velocities $\mathbf{c}_i$. The density fluctuation $\delta\rho$ and the momentum $\mathbf{j} := (j_x, j_y)$ are conserved moments in our model; $e, \varepsilon, \mathbf{q} = (q_x, q_y), p_{xx}$ and p_{xy} are related to the energy, the energy square, the heat flux and the diagonal and off-diagonal components of the stress tensor, respectively. With the low Mach number approximation, the non-conserved moments are expressed in terms of conserved moments

$$\begin{aligned} e^{(eq)} &= -2\delta\rho + 3\mathbf{j}\cdot\mathbf{j} \\ \varepsilon^{(eq)} &= \delta\rho - 3\mathbf{j}\cdot\mathbf{j} \\ q_x^{(eq)} &= -j_x \\ q_y^{(eq)} &= -j_y \\ p_{xx}^{(eq)} &= j_x^2 - j_y^2 \\ p_{xy}^{(eq)} &= j_x j_y \end{aligned}$$

For D2Q9 model, the transformation matrix is

$$\mathbf{M} = \begin{pmatrix} 1 & 1 & 1 & 1 & 1 & 1 & 1 & 1 & 1 \\ -4 & -1 & -1 & -1 & -1 & 2 & 2 & 2 & 2 \\ 4 & -2 & -2 & -2 & -2 & 1 & 1 & 1 & 1 \\ 0 & 1 & 0 & -1 & 0 & 1 & -1 & -1 & 1 \\ 0 & -2 & 0 & 2 & 0 & 1 & -1 & -1 & 1 \\ 0 & 0 & 1 & 0 & -1 & 1 & 1 & -1 & -1 \\ 0 & 0 & -2 & 0 & 2 & 1 & 1 & -1 & -1 \\ 0 & 1 & -1 & 1 & -1 & 0 & 0 & 0 & 0 \\ 0 & 0 & 0 & 0 & 0 & 1 & -1 & 1 & -1 \end{pmatrix}$$

Multiple-relaxation-time scheme is optimized to ensure Galilean invariance and isotrophy, while minimizing dissipation and dispersion. Consequently, the s_7 and s_1 are determined by the shear viscosity μ and the bulk viscosity ξ through

$$\mu = \frac{1}{3}(\frac{1}{s_7} - \frac{1}{2})c\delta_x \text{ and } \xi = \frac{1}{6}(\frac{1}{s_1} - \frac{1}{2})c\delta_x \tag{99}$$

The relaxation rates s_0, s_3 and s_5 who correspond to the conserved moments ($\delta\rho$, j_x and j_y), have no effect on the model. The parameters s_2, s_4 and s_6 are for the moment ε, energy flux components q_x and q_y, and are only relevant to the higher-order hydrodynamic term. These values are determined by linear stability analysis and are set to $s_2 = 1.54$ and $s_4 = s_6 = 1.9$ in current study.

3.1.2 THREE DIMENSIONAL LATTICE BOLTZMANN MODEL

In D3Q19 model, the velocity discretization for the fluid particles is described as $(\mathbf{c_1}, \mathbf{c_2}, \mathbf{c_3}, \mathbf{c_4}, \mathbf{c_5}, \mathbf{c_6}, \mathbf{c_7}, \mathbf{c_8}, \mathbf{c_9}, \mathbf{c_{10}}, \mathbf{c_{11}}, \mathbf{c_{12}}, \mathbf{c_{13}}, \mathbf{c_{14}}, \mathbf{c_{15}}, \mathbf{c_{16}}, \mathbf{c_{17}}, \mathbf{c_{18}}, \mathbf{c_{19}}) =$

$$\begin{pmatrix} 0 & 1 & -1 & 0 & 0 & 0 & 0 & 1 & 1 & -1 & -1 & 1 & -1 & 1 & -1 & 0 & 0 & 0 & 0 \\ 0 & 0 & 0 & 1 & -1 & 0 & 0 & 1 & -1 & 1 & -1 & 0 & 0 & 0 & 0 & 1 & 1 & -1 & -1 \\ 0 & 0 & 0 & 0 & 0 & 1 & -1 & 0 & 0 & 0 & 0 & 1 & 1 & -1 & -1 & 1 & -1 & 1 & -1 \end{pmatrix}$$

The transformation matrix **M**, according to [37] and [36], is defined as

$$\begin{pmatrix}
1 & 1 & 1 & 1 & 1 & 1 & 1 & 1 & 1 & 1 & 1 & 1 & 1 & 1 & 1 & 1 & 1 & 1 & 1 \\
-30 & -11 & -11 & -11 & -11 & -11 & -11 & 8 & 8 & 8 & 8 & 8 & 8 & 8 & 8 & 8 & 8 & 8 & 8 \\
12 & -4 & -4 & -4 & -4 & -4 & -4 & 1 & 1 & 1 & 1 & 1 & 1 & 1 & 1 & 1 & 1 & 1 & 1 \\
0 & 1 & -1 & 0 & 0 & 0 & 0 & 1 & -1 & 1 & -1 & 1 & -1 & 1 & -1 & 0 & 0 & 0 & 0 \\
0 & -4 & 4 & 0 & 0 & 0 & 0 & 1 & -1 & 1 & -1 & 1 & -1 & 1 & -1 & 0 & 0 & 0 & 0 \\
0 & 0 & 0 & 1 & -1 & 0 & 0 & 1 & 1 & -1 & -1 & 0 & 0 & 0 & 0 & 1 & -1 & 1 & -1 \\
0 & 0 & 0 & -4 & 4 & 0 & 0 & 1 & 1 & -1 & -1 & 0 & 0 & 0 & 0 & 1 & -1 & 1 & -1 \\
0 & 0 & 0 & 0 & 0 & 1 & -1 & 0 & 0 & 0 & 0 & 1 & 1 & -1 & -1 & 1 & 1 & -1 & -1 \\
0 & 0 & 0 & 0 & 0 & -4 & 4 & 0 & 0 & 0 & 0 & 1 & 1 & -1 & -1 & 1 & 1 & -1 & -1 \\
0 & 2 & 2 & -1 & -1 & -1 & -1 & 1 & 1 & 1 & 1 & 1 & 1 & 1 & 1 & -2 & -2 & -2 & -2 \\
0 & -4 & -4 & 2 & 2 & 2 & 2 & 1 & 1 & 1 & 1 & 1 & 1 & 1 & 1 & -2 & -2 & -2 & -2 \\
0 & 0 & 0 & 1 & 1 & -1 & -1 & 1 & 1 & 1 & 1 & -1 & -1 & -1 & -1 & 0 & 0 & 0 & 0 \\
0 & 0 & 0 & -2 & -2 & 2 & 2 & 1 & 1 & 1 & 1 & -1 & -1 & -1 & -1 & 0 & 0 & 0 & 0 \\
0 & 0 & 0 & 0 & 0 & 0 & 0 & 1 & -1 & -1 & 1 & 0 & 0 & 0 & 0 & 0 & 0 & 0 & 0 \\
0 & 0 & 0 & 0 & 0 & 0 & 0 & 0 & 0 & 0 & 0 & 0 & 0 & 0 & 0 & 1 & -1 & -1 & 1 \\
0 & 0 & 0 & 0 & 0 & 0 & 0 & 0 & 0 & 0 & 0 & 1 & -1 & -1 & 1 & 0 & 0 & 0 & 0 \\
0 & 0 & 0 & 0 & 0 & 0 & 0 & 1 & -1 & 1 & -1 & -1 & 1 & -1 & 1 & 0 & 0 & 0 & 0 \\
0 & 0 & 0 & 0 & 0 & 0 & 0 & -1 & -1 & 1 & 1 & 0 & 0 & 0 & 0 & 1 & -1 & 1 & -1 \\
0 & 0 & 0 & 0 & 0 & 0 & 0 & 0 & 0 & 0 & 0 & 1 & 1 & -1 & -1 & -1 & -1 & 1 & 1
\end{pmatrix} \tag{100}$$

The diagonal matrix of 19 relaxation parameters is

$\mathbf{S} = \left(s_0, s_1, s_2, s_3, s_4, s_5, s_6, s_7, s_8, s_9, s_{10}, s_{11}, s_{12}, s_{13}, s_{14}, s_{15}, s_{16}, s_{17}, s_{18}\right)$ where s_0, s_3, s_5 and s_7 correspond to conserved density ρ and momenta j_x, j_y and j_z, and the choices of which do not alter the model. The relaxation parameters $s_9 = s_{11} = s_{13} = s_{14} = s_{15}$, for components of the pressure tensor $3p_{xx}$, p_{ww}, p_{xy}, p_{yz} and p_{xz}, are determined by kinematic viscosity μ by the equation

$$\mu = \frac{1}{3}\left(\frac{1}{s_9} - \frac{1}{2}\right) \tag{101}$$

The bulk parameters s_2, s_6 and s_8 for mass fluxes q_x, q_y and q_z are set equal to s_9 due to the sake of isotropy. The remaining parameters s_2 for energy square ε; s_{10} and s_{12} for $3\pi_{xx}$ and π_{ww}; s_{16}, s_{17} and s_{18} relating to m_x, m_y and m_z are high-order terms which do not alter the hydrodynamics and are set to 1.8 by linear stability analysis.

3.2 IMMERSED BOUNDARY METHOD

The primary advantage of immersed boundary method is associated with the fact that the grid generation is greatly simplified, compared to generate a body-conformal structured or unstructured grid. In the immersed boundary method, a Cartesian grid maybe employed for the fluid simulation and body immersed in the field is represented on a Lagrangian coordinates. The fluid velocity near the capsule boundary is used to determine the velocity of the capsule and is used to update the position of the capsule. The deformation of the capsule generates forces. The incompressible Navier-Stokes Equations are solved, using LBM, with the addition of these forces to determine the fluid velocity. A smoothed Dirac delta function is used to transfer the necessary data between the two grids. The smoothed Dirac delta function in d-dimensional space is defined by

$$\delta_h(\mathbf{x}) = \delta_h(x_1)\delta_h(x_2)\cdots\delta_h(x_d), \quad \mathbf{x} \in R^d \tag{102}$$

in which the one dimensional discrete delta function is given by

$$\delta_h(x) = \begin{cases} \frac{1}{4h}\left[1+\cos(\frac{\pi x \pi}{2h})\right] & |x| \leq 2h \\ 0 & |x| \geq 2h \end{cases} \tag{103}$$

The smoothed delta function is employed to determine the fluid velocity at capsule grid points, based on the local fluid velocity, and to spread the body forces created by capsule deformation to the nearby fluid. In our model, the membrane of immersed capsule is represented by a set of elastic fibers and the location of these fibers is tracked by a collection of mass-less points that move with the local fluid velocity, thus the capsule velocity $\mathbf{U}$ is determined at Lagrangian node $\mathbf{X}_c$ by

$$\mathbf{U}(\mathbf{X}_c) = \sum_j \delta(\mathbf{X}_c - \mathbf{x}_j)\mathbf{u}(\mathbf{x}_j)h^d \tag{104}$$

in which $\mathbf{x}_j$ and $\mathbf{u}$ denote Eulerian fluid node position and velocity, respectively. Subsequently, this velocity is used to update the position of the Lagrangian grid by the forward Euler method

$$\mathbf{X}_c(t_n + dt) = \mathbf{X}_c(t_n) + \mathbf{U}(\mathbf{X}_c)dt \tag{105}$$

The effect of the immersed boundary on the surrounding fluid is captured by distributing the fiber stress $\mathbf{P}$ to the fluid grid points through a localized forcing term in the momentum equation by

$$\mathbf{p}(\mathbf{x}_j) = \sum_c \delta(\mathbf{X}_c - \mathbf{x}_j)\mathbf{P}(\mathbf{X}_c) \tag{106}$$

as the area of the elements has already been incorporated into calculation of $\mathbf{P}$ at $\mathbf{X}_c$. Subsequently, the forces exerted on the fluid are incorporated into the fluid simulation according to the update method described in [38] and [35]. In the collision phase of LBM, after computing the hydrodynamic moments, momenta $\mathbf{j} = \left(j_x, j_y, j_z\right)$ at grid point $\mathbf{x}_j$ are updated to according to the forces $\mathbf{p}$, as

$$\mathbf{j}'(\mathbf{x}_j) = \mathbf{j}(\mathbf{x}_j) + \frac{dt}{2}\mathbf{p}(\mathbf{x}_j) \tag{107}$$

After using $\mathbf{j}'$ to find the equilibrium moments $\mathbf{m}^{(eq)}$, the momentum is updated again, as

$$\mathbf{j}''(\mathbf{x}_j) = \mathbf{j}'(\mathbf{x}_j) + \frac{dt}{2}\mathbf{p}(\mathbf{x}_j) \tag{108}$$

and $\mathbf{j}''$ is used to compute the probability distribution after the collision phase. The advection step of LBM is not altered by the addition of forces acting on the fluid.

3.3 STRUCTURAL ALGORITHM FOR TWO DIMENSIONS

Due to the immersed boundary method, velocity is continuous across the membrane. However, a jump in interfacial tension across the interface does exist. A red blood cell type capsule has shear and isotropic elasticity, bending stiffness and membrane viscosity [39, 40, 7]. Consequently, using Gauss's divergence theorem, Pozrikidis [41] derives the force equilibrium equation for complete tension $\mathbf{T} = \tau\hat{\mathbf{t}} + q\hat{\mathbf{n}}$ as

$$\mathbf{f} = -(\mathbf{P_{surf}} \cdot \nabla) \cdot (\tau\hat{\mathbf{t}} + q\hat{\mathbf{n}}) \tag{109}$$

for in-plane tension τ, transverse shear tension q, tangent vector $\hat{\mathbf{t}}$, and outward normal vector $\hat{\mathbf{n}}$. The projection matrix $\mathbf{P_{surf}} = \mathbf{I} - \mathbf{nn}$ projects the gradient to the capsule surface and hence $\mathbf{P_{surf}}$ is the surface gradient. In two dimensions, the equation is simplified by the Frenet-Serret formulae to

$$\mathbf{f} = -\frac{\partial}{\partial \ell}(\tau\hat{\mathbf{t}} + q\hat{\mathbf{n}}) = \left[\kappa\tau - \frac{\partial q}{\partial \ell}\right]\hat{\mathbf{n}} - \left[\frac{\partial \tau}{\partial \ell} + \kappa q\right]\hat{\mathbf{t}} \tag{110}$$

for capsule curvature κ and derivatives taken with respect to capsule arc length ℓ. Further, the transverse shear tension q is simply the derivative of bending moment m with respect to arc length, as $q = \dfrac{\partial m}{\partial \ell}$. The first and second derivatives with respect to arc length are computed by using five-point centered difference methods for arbitrarily spaced stencil.

The viscoelastic character of the capsule membrane is described by the Kelvin-Voigt viscoelastic model, where in-plane tension is simply the sum of the elastic and viscous contributions

$$\tau = \tau_e + \tau_v \tag{111}$$

Strain for each element of the capsule is given in terms of the stretch ratio λ, which is defined by the ratio of a line element's current length $\ell(t)$ and initial length ℓ_0, as

$$\lambda(t) = \frac{\ell(t)}{\ell_0} \tag{112}$$

For simplicity, Hooke's law is employed to describe the capsule's shear elasticity and determine the elastic tension τ_e. This model takes the form

$$\tau_e = E_s(\lambda - 1) \tag{113}$$

where E_s is the shear elasticity modulus. The tension due to membrane viscosity is defined by

$$\tau_v = \mu_s \frac{1}{\lambda}\frac{\partial \lambda}{\partial t} \tag{114}$$

in which μ_s is the membrane viscosity coefficient. The time derivative of λ is calculated by a one-sided second order finite difference method. The capsule's isotropic elasticity is not explicitly included in the two dimensional algorithm. Transverse shear tension is the result of bending stiffness and defined as

$$q = \frac{\partial m}{\partial \ell} = E_B \frac{\partial}{\partial \ell}(\kappa - \kappa_0) \tag{115}$$

in which E_B is the bending stiffness modulus, κ is the current curvature, and κ_0 is the initial shape configured curvature. Pozrikidis noted that, equation (115) is only correct for small deviations from the preferred curvature [42, 41], but is sufficient to account for the qualitative role of bending stiffness here [41]. For both circular and biconcave capsule, κ_0 is set equal to the initial curvature. Curvature κ is calculated with periodic cubic spline interpolation, if the capsule surface is parameterized by the function F, then

$$\kappa = \frac{\pm F''}{(1+F'^2)^{3/2}} \tag{116}$$

Thus, the two dimensional capsule is unstressed, by either viscoelastic tension or bending moments, at the initial shape configuration.

The heavy side function is used to deal with the non-dimensional fluid viscosity ratio V. Let d be the shortest distance from the fluid node to the capsule boundary. The sign of d for a fluid note is set to be positive if located outside the capsule and negative if in side the capsule. With the signed distance d having been determined, a smoothed Heaviside function of d from [3] is defined as

$$H(d) = \begin{cases} 0 & d \leq 2h \\ \frac{1}{2}(1+\frac{d}{2h}+\frac{1}{\pi}\sin\frac{\pi d}{2h}) & -2h \leq d \leq 2h \\ 1 & d \geq 2h \end{cases} \tag{117}$$

The viscosity μ, at the node, is determined using $H(d)$ by the equation

$$\mu(\mathbf{x}) = \mu_c + (\mu_a - \mu_c)H[d(\mathbf{x})] \tag{118}$$

in terms of viscosity μ_c inside the capsule and ambient viscosity μ_a.

In order to proceed, three additional structural non-dimensional parameters are defined. The capillary number for the fluid, Ca, is defined as

$$Ca = \frac{\mu_a k a}{E_s} \tag{119}$$

in terms of ambient fluid viscosity μ_a, shear rate k, equivalent capsule radius a, and shear elasticity modulus E_s. The capillary number Ca represents the ratio of viscous fluid shear to solid elastic force, and is also referred to as the dimensionless shear rate in the literature. The bending stiffness

E_b is defined as

$$E_b = \frac{E_B}{aE_s} \tag{120}$$

for bending stiffness modulus E_B and represents the ratio of bending to shear resistance. Finally, the membrane viscosity ratio η is defined as

$$\eta = \frac{\mu_s}{a\mu_a} \tag{121}$$

for membrane viscosity coefficient μ_s and equivalent radius a; thus, η is the ratio of membrane to ambient fluid viscosity.

3.4 THREE DIMENSIONAL ALGORITHM

In contrast to the discretization of a set of line segments in two dimensional, the three dimensional capsule surface is discretized into flat triangular elements. The mesh generation is similar to the approach as in [43] for an octaheron. To discretize the surface of spherical capsule, an icosahedron is placed in the circumscribed capsule, each triangular face of the icosaheran is subdivided into four equal triangles, the new bisect points on the edges are then projected onto the sphere. This process is repeated until the mesh is sufficiently fine. The discretization of biconcave surface can be done in the same manner. The discretization for sphere and biconcave shapes are shown in 15, a mesh with 2562 vertices and 5120 triangles is considered sufficient respectively, based on the fluid grid and convergence analysis.

3.4.1 FINITE ELEMENT MEMBRANE

As stated previously, in three dimensional algorithm, the capsule's elastic character is described by a finite element model, the forces are obtained at the discrete nodes of the membrane, only in-plane stresses and strains exist. The capsule itself is considered to be massless and composed of a set of zero-thickness triangles, surrounding the interior fluid. In three dimensional situation, a deformed triangle is often no longer in the plane of the undeformed triangle. The approach of Charrier $etal.$ is adopted, mapping the undeformed and deformed triangular elements to the common $z = 0$ plane. The undeformed flat triangular element $x_i x_j x_k$ is deformed into flat triangular element $X_i X_j X_k$, in the same plane $z = 0$, Figure 16. If a material point $\mathbf{x}$ undergoes a displacement

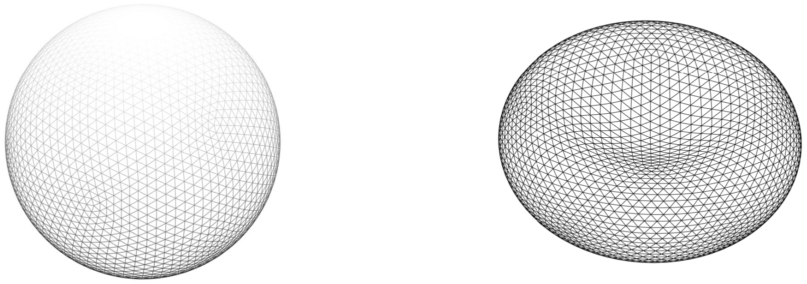

Figure. 15: Discretization of a sphere and a biconcave shape.

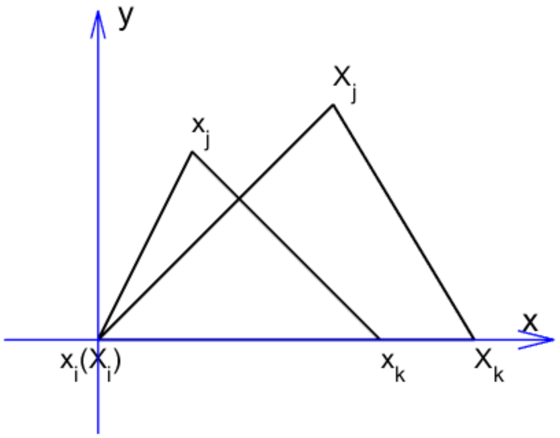

Figure. 16: Undeformed triangular patch $x_ix_jx_k$ and deformed triangular patch $X_iX_jX_k$.

u arriving the position **X**, it can be described by

$$\mathbf{X} = \mathbf{x} + \mathbf{u}(\mathbf{x}) \tag{122}$$

A neighboring point $\mathbf{x}+d\mathbf{x}$ arrives at $\mathbf{X}+d\mathbf{X}$, the relation between the two is given by

$$\mathbf{X}+d\mathbf{X}=\mathbf{x}+d\mathbf{x}+u(\mathbf{x}+d\mathbf{x}) \tag{123}$$

or, equivalently,

$$d\mathbf{X}=d\mathbf{x}+\mathbf{u}(\mathbf{x}+d\mathbf{x})-\mathbf{u}(\mathbf{x}) \tag{124}$$

Using the definition of gradient of a vector function, (124) becomes

$$d\mathbf{X}=d\mathbf{x}+(\nabla\mathbf{u})d\mathbf{x} \tag{125}$$

where $\nabla\mathbf{u}$ is a second-order displacement gradient. In current situation, the matrix of $\nabla\mathbf{u}$ with respect to rectangular Cartesian coordinates is

$$[\nabla\mathbf{u}]=\begin{pmatrix} \frac{\partial u_1}{\partial x_1} & \frac{\partial u_1}{\partial x_2} \\ \frac{\partial u_2}{\partial x_1} & \frac{\partial u_2}{\partial x_2} \end{pmatrix}$$

Then we write (125) as

$$d\mathbf{X}=\mathbf{F}d\mathbf{x} \tag{126}$$

where $\mathbf{F}$ is the deformation gradient matrix with $F_{ij}=\dfrac{\partial X_i}{\partial x_j}=\delta_{ij}+\dfrac{\partial u_i}{\partial x_j}$. The square of the displacement, is by taking the dot product of $d\mathbf{X}$ with itself

$$d\mathbf{X}\cdot d\mathbf{X}=\mathbf{F}d\mathbf{x}\cdot\mathbf{F}d\mathbf{x}=d\mathbf{X}\cdot(\mathbf{F}^T\mathbf{F})d\mathbf{X} \tag{127}$$

where $\mathbf{G}=\mathbf{F}^T\mathbf{F}$ is known as the right Cauchy-Green deformation tensor. It is the matrix of the metric tensor of the deformed element with components

$$G_{11}=\left(1+\frac{\partial u}{\partial x}\right)^2+\left(\frac{\partial v}{\partial x}\right)^2 \tag{128}$$

$$G_{22}=\left(\frac{\partial u}{\partial y}\right)^2+\left(1+\frac{\partial v}{\partial y}\right)^2 \tag{129}$$

$$G_{12}=G_{21}=\left(1+\frac{\partial u}{\partial x}\right)\left(\frac{\partial u}{\partial y}\right)+\left(1+\frac{\partial v}{\partial y}\right)\left(\frac{\partial v}{\partial x}\right) \tag{130}$$

The principle values λ_1 and λ_2 of the in-plane stretch ratios are

$$\lambda_1^2 = \frac{1}{2}\left[G_{11} + G_{22} + \sqrt{(G_{11} - G_{22})^2 + 4G_{12}^2}\right] \tag{131}$$

$$\lambda_1^2 = \frac{1}{2}\left[G_{11} + G_{22} - \sqrt{(G_{11} - G_{22})^2 + 4G_{12}^2}\right] \tag{132}$$

The principle of virtual work is used to calculate the forces at the three nodes of an element. For a finite element of an elastic material, in absence of body forces and acceleration, this principle may be written as

$$\delta W_e = \{\delta u\}^T \{F_x\} + \{\delta v\}^T \{F_y\} \tag{133}$$

where δW_e is a first order variation in the strain energy of the element due to the infinitesimal changes $\{\delta u\}$ and $\{\delta v\}$ in the nodal displacements. $\{F_x\}^T = (F_{xi}\, F_{xj}\, F_{xk})$ and $\{F_y\}^T = (F_{yi}\, F_{yj}\, F_{yk})$ are the nodal forces in the x and y directions corresponding to the current deformed state of the element. Under the assumption of homogeneous deformation, the stretch ratios are constant within the element, and we have

$$\delta W_e = V_e \delta W \tag{134}$$

where V_e is the original volume of the element and W is the strain energy density. Consider initially isotropic membrane material, W is a symmetric function of the principle stretch ratios, and W can be taken as an independent function of only the in-plane stretch ratios λ_1 and λ_2 with first order variation expressed as

$$\delta W = \{\delta u\}^T \left[\frac{\partial W}{\partial \lambda_1}\left\{\frac{\partial \lambda_1}{\partial u}\right\} + \frac{\partial W}{\partial \lambda_2}\left\{\frac{\partial \lambda_2}{\partial u}\right\}\right] + \{\delta v\}^T \left[\frac{\partial W}{\partial \lambda_1}\left\{\frac{\partial \lambda_1}{\partial v}\right\} + \frac{\partial W}{\partial \lambda_2}\left\{\frac{\partial \lambda_2}{\partial v}\right\}\right] \tag{135}$$

It follows that the nodal force-displacement relations for the element are finally of the form

$$\begin{aligned} \{F_x\} &= V_e \frac{\partial W}{\partial \lambda_1}\left\{\frac{\partial \lambda_1}{\partial u}\right\} + V_e \frac{\partial W}{\partial \lambda_2}\left\{\frac{\partial \lambda_2}{\partial u}\right\} \\ \{F_y\} &= V_e \frac{\partial W}{\partial \lambda_1}\left\{\frac{\partial \lambda_1}{\partial v}\right\} + V_e \frac{\partial W}{\partial \lambda_2}\left\{\frac{\partial \lambda_2}{\partial v}\right\} \end{aligned} \tag{136}$$

3.4.2 MEMBRANE CONSTITUTIVE LAW & ELASTIC STRESS

For such a purely elastic capsule, the Cauchy stress caused by deformation is determined using a two-dimensional constitutive law. The simplest approach, known as the neo-Hookean law, corresponds to membranes made of polymerized material. The neo-Hookean law does not restrict the area dilation and has purely shear elasticity. The energy strain relation for the neo-Hookean law has the form

$$W_{NH} = \frac{E_s}{6}(\lambda_1^2 + \lambda_2^2 + \lambda_1^{-2}\lambda_2^{-2} - 3) \tag{137}$$

for incompressible neo-Hookean material with shear elasticity modulus E_s. The principal stains, λ_1 and λ_2, are eigenvalues of the deformation tensor and represent the principle stretching ratios.

The zero-thickness (ZT) shell equation is another version of the neo-Hookean (NH) law, which has been used by Ramanujan and Pozrikidis in [43]

$$W_{ZT} = \frac{E_s}{6}\Big(\lambda_1^2 + \lambda_2^2 - 2 - 2\log(\lambda_1\lambda_2) + 2(\log\lambda_1\lambda_2)^2\Big) \tag{138}$$

The Skalak's constitutive law, proposed by Skalak, includes both shear elasticity and the local conservation of surface area, is used to model the membrane red blood cell in [7]. The energy strain relation is expressed as

$$W_{SK} = \frac{E_s}{4}\Big((\lambda_1 + \lambda_2 - 2)^2 + 2(\lambda_1 + \lambda_2 - 2)^2 - 2(\lambda_1^2\lambda_2^2 - 1) + C(\lambda_1^2\lambda_2^2 - 1)^2\Big) \tag{139}$$

The term $C(\lambda_1^2\lambda_2^2 - 1)^2$ accounts for the area dilation. The additional parameter C is the ratio between shear elasticity modulus and area dilation modulus, which is quite large for incompressible biological membranes. Measures of C for red blood cells are typically on the order of 10^5 for extremely small time step. For practical purpose, a preferable chosen of $C = 15$ permits some change in capsule surface area and prevent significant dilation or compression.

The neo-Hookean constitutive law is adequate to describe a spherical capsule. For biconcave capsules, however, the incompressibility of the membrane is a significant factor. Consequently, in subsequent results, spherical and biconcave capsules are described by noe-Hookean and Skalak constitutive law, respectively.

The principal stresses in neo-Hookean law can be expressed as

$$\sigma_1 = \frac{1}{\lambda_2}\frac{\partial W_{NH}}{\partial \lambda_1} = \frac{E_s}{\lambda_1\lambda_2}\Big(\lambda_1^2 - \frac{1}{\lambda_1^2\lambda_2^2}\Big) \tag{140}$$

$$\sigma_2 = \frac{1}{\lambda_1}\frac{\partial W_{NH}}{\partial \lambda_2} = \frac{E_s}{\lambda_1\lambda_2}\Big(\lambda_1^2 - \frac{1}{\lambda_1^2\lambda_2^2}\Big) \tag{141}$$

The principal stresses derived from Skalak law are

$$\sigma_1 = \frac{1}{\lambda_2}\frac{\partial W_{SK}}{\partial \lambda_1} = \frac{E_s}{\lambda_1\lambda_2}\Big(\lambda_1^2(\lambda_1^2-1) + C(\lambda_1\lambda_2)^2(\lambda_1^2\lambda_2^2)\Big) \tag{142}$$

$$\sigma_2 = \frac{1}{\lambda_1}\frac{\partial W_{SK}}{\partial \lambda_2} = \frac{E_s}{\lambda_1\lambda_2}\Big(\lambda_2^2(\lambda_2^2-1) + C(\lambda_1\lambda_2)^2(\lambda_1^2\lambda_2^2)\Big) \tag{143}$$

3.4.3 BENDING STIFFNESS

The biological capsule's membrane is known to be incompressible and exhibits a resistance against bending. Thus, in addition to tension energy, bending energy should be taken into account for present simulation. Namely, for a closed surface, the Helfrich-type energy of a zero-membrane is used to enforce the incompressibility constraint and given by

$$W_b = \frac{E_B}{2}\int_S (2\kappa - c_0)^2 dS \tag{144}$$

for the bending stiffness modulus E_B of mean curvature, capsule surface area S, mean curvature κ and spontaneous curvature c_0 [44]. By taking the variational derivative [45] to the surface, one can derive the bending force density $\mathbf{f}_b$ at a node as

$$\mathbf{f}_b = \frac{E_B}{2}\Big((2\kappa + c_0)(2\kappa^2 - 2\kappa_g - c_0\kappa) + 2\Delta_{LB}\kappa\Big)\mathbf{n} \tag{145}$$

in which κ_g is the Gaussian curvature of the membrane, $\mathbf{n}$ is the unit outward normal vector to the surface and Δ_{LB} is the surface Laplacian (or Laplace-Beltrami) operator. For spherical capsules, the choice of spontaneous curvature is $c_0 = 0$, which indicates that the membrane does not have an internal/external asymmetry and leads to $\mathbf{f}_b = 0$ for the undeformed capsules. However, spontaneous curvature c_0 is not simply the three dimensional analogue of the two dimensional preferred curvature k_0.

3.5 ELECTRIC FORCE

As described in [46] and [47], the stress induced in a dielectric medium under an electric field is given by the Maxwell stress tensor of the form

$$\mathbf{M_E} = \varepsilon\Big(\mathbf{EE} - \frac{1}{2}(\mathbf{E}\cdot\mathbf{E})\mathbf{I}\Big) \tag{146}$$

the volume force density $\mathbf{f_E}$ of the Maxwell stress induced in a dielectric medium, can be calculated by taking the divergence of the Maxwell stress tensor $\mathbf{M_E}$ while assuming that the fluid is incompressible of the form

$$\mathbf{f_E} = -\frac{1}{2}\mathbf{E}\cdot\mathbf{E}\nabla\varepsilon + \nabla\cdot(\varepsilon\mathbf{E})\mathbf{E} = \nabla\cdot\mathbf{M_E} = -\frac{1}{2}\mathbf{E}\cdot\mathbf{E}\nabla\varepsilon + q_v\mathbf{E} \tag{147}$$

where ρ is the density of fluid. The first term on the right hand side, $-\frac{1}{2}\mathbf{E}\cdot\mathbf{E}\nabla\varepsilon$, is due to the polarization stress and it acts along the normal direction of the interface as a result of the term $\nabla\varepsilon$. The second term is due to the interaction of the electric charges with the electric field acting along the direction of the electric field. Since both the permittivity and conductivity are piecewise constants, the volume force density $\mathbf{f_E}$ in (147) is none zero only in the vicinity of the interface due to the fact of $\nabla\cdot\mathbf{E} = 0$ in both Ω^+ and Ω^-. As the electric charges are on the interface, both the polarization electric stress and the charge-field interaction electric stress would thus be exerted as interfacial forces from the jump of Maxwell stress in the normal direction rather than applying the volume force as in (147) into fluid equation. The interfacial electric force is hence defined as

$$\mathbf{F_E} = \|\mathbf{M_E}\cdot\mathbf{n}\| = (\mathbf{M_E^+} - \mathbf{M_E^-})\cdot\mathbf{n} \tag{148}$$

where $\mathbf{M_E^+}$ and $\mathbf{M_E^-}$ refer to the exterior and interior Maxwell stress tensors, respectively. Thus, the electric volume force $\mathbf{f_E}$ can be alternatively represented by the electric interfacial force using the Dirac delta function (102) as

$$\mathbf{f_E}(\mathbf{x},t) = \int_\Sigma \mathbf{F_E}(s,t)\delta(\mathbf{x} - \mathbf{X}(s,t))|\mathbf{X}_s|ds \tag{149}$$

where $\mathbf{X}$ is the set of Langrangian nodes on the interface, s and t are the parameters describing the interface Σ, $\mathbf{X}_s$ denotes the partial derivative of $\mathbf{X}$ with respect to the s.

In two dimensions, the interfacial electric force can be explicitly expressed in term of computed results of $\mathbf{E} = (-\phi_x, -\phi_y)$, normal vector $\mathbf{n}$ and tangential vector τ. We rewrite $\mathbf{E} = E_n\mathbf{n} + E_\tau\tau$, where $E_n = (-\phi_x, -\phi_y)\cdot\mathbf{n}$ and $E_\tau = (-\phi_x, -\phi_y)\cdot\tau$. Substitute $\mathbf{E}$ into (146) and dot the normal vector $\mathbf{n}$, we can obtain the expression for Maxwell stress:

$$\begin{aligned}
\mathbf{M_E}\cdot\mathbf{n} &= \varepsilon\Big(\mathbf{EE} - \frac{1}{2}(\mathbf{E}\cdot\mathbf{E})\mathbf{I}\Big)\cdot\mathbf{n} \\
&= \varepsilon((E_n\mathbf{n} + E_\tau\tau)(E_n\mathbf{n} + E_\tau\tau))\cdot\mathbf{n} - \frac{\varepsilon}{2}(E_n^2 + E_\tau^2)\mathbf{I}\cdot\mathbf{n} \\
&= \varepsilon(E_n^2)\mathbf{n} + \varepsilon(E_\tau E_n\tau) - \frac{\varepsilon}{2}(E_n^2 + E_\tau^2)\mathbf{n} \\
&= \frac{\varepsilon}{2}(E_n^2 - E_\tau^2)\mathbf{n} + \varepsilon E_n E_\tau\tau
\end{aligned}$$

The interfacial electric force is in consequence written as

$$\begin{aligned}
\mathbf{F_E} &= (\mathbf{M_E^+} - \mathbf{M_E^-})\cdot\mathbf{n} \\
&= \frac{\varepsilon}{2}(E_n^{+2} - E_n^{-2} - E_\tau^{+2} + E_\tau^{-2})\mathbf{n} + \varepsilon(E_n^+E_\tau^+ - E_n^-E_\tau^-)\tau
\end{aligned}$$

Similarly, in three dimensions, the electric field is given by $\mathbf{E} = (-\phi_x, -\phi_y, -\phi_z)$, the normal vector is $\mathbf{n}$ and two orthogonal tangent vectors are denoted by τ_1 and τ_2. Now $\mathbf{E}$ can be written in terms of E_n, E_{τ_1} and E_{τ_2}

$$\mathbf{E} = E_n\mathbf{n} + E_{\tau_1}\tau_1 + E_{\tau_2}\tau_2 \tag{150}$$

where $E_n = (-\phi_x, -\phi_y, -\phi_z)\cdot\mathbf{n}$, $E_{\tau_1} = (-\phi_x, -\phi_y, -\phi_z)\cdot\tau_1$ and $E_{\tau_2} = (-\phi_x, -\phi_y, -\phi_z)\cdot\tau_2$. The three dimensional Maxwell Stress is

$$\begin{aligned}
&\mathbf{M_E}\cdot\mathbf{n} = \varepsilon\Big(\mathbf{EE} - \frac{1}{2}(\mathbf{E}\cdot\mathbf{E})\mathbf{I}\Big)\cdot\mathbf{n} \\
&= \varepsilon((E_n\mathbf{n} + E_{\tau_1}\tau_1 + E_{\tau_2}\tau_2)(E_n\mathbf{n} + E_{\tau_1}\tau_1 + E_{\tau_2}\tau_2))\cdot\mathbf{n} - \frac{\varepsilon}{2}(E_n^2 + E_{\tau_1}^2 + E_{\tau_2}^2)\mathbf{I}\cdot\mathbf{n} \\
&= \varepsilon(E_n^2)\mathbf{n} + \varepsilon(E_{\tau_1}E_n)\tau_1 + \varepsilon(E_{\tau_2}E_n)\tau_2 - \frac{\varepsilon}{2}(E_n^2 + E_{\tau_1}^2 + E_{\tau_2}^2)\mathbf{n} \\
&= \frac{\varepsilon}{2}(E_n^2 - E_{\tau_1}^2 - E_{\tau_2}^2)\mathbf{n} + \varepsilon E_n E_{\tau_1}\tau_1 + \varepsilon E_n E_{\tau_2}\tau_2
\end{aligned}$$

The interfacial electric force is in consequence written as

$$
\begin{aligned}
\mathbf{F_E} &= (\mathbf{M_E^+} - \mathbf{M_E^-}) \cdot \mathbf{n} \\
&= \frac{\varepsilon}{2}(E_n^{+2} - E_n^{-2} - E_{\tau_1}^{+2} + E_{\tau_1}^{-2} - E_{\tau_2}^{+2} + E_{\tau_2}^{-2})\mathbf{n} \\
&+ \varepsilon(E_n^+ E_{\tau_1}^+ - E_n^- E_{\tau_1}^-)\tau_1 + \varepsilon(E_n^+ E_{\tau_2}^+ - E_n^- E_{\tau_2}^-)\tau_2
\end{aligned}
$$

3.6 THE OUTLINE OF NUMERICAL ALGORITHM FOR ELECTROHYDRODYNAMICS

The numerical implementation of one step calculation at time t^n is as follows.

1. Compute the electric potential ϕ^n by the fast immersed interface method, and calculate the electric field $\mathbf{E} = (-\phi_x^n, -\phi_y^n)$ on the grid. Compute the interface electric force using Maxwell stresses tensor at Lagrangian points on the interface.

2. Calculate the interfacial tension (for droplet) or viscoelastic force and bending force (for blood cell membrane).

3. Distribute all forces from the Lagrangian points to the fluid points by using the discrete delta function as in immersed boundary method.

4. Solve the governing equation of lattice-Boltzmann method and update the velocity to $\mathbf{u}^{n+1}$.

5. Interpolate the new velocity on the fluid grid points to the Lagrangian points and drive the points to new positions $\mathbf{x}^{n+1}$.

CHAPTER 4

NUMERICAL VALIDATION

4.1 FLUID-STRUCTURE INTERACTION VALIDATION

The deformation of the capsule is described by the Taylor shape parameter, which is defined as

$$D_{xy} = \frac{L-B}{L+B} \tag{151}$$

where L is the end-to-end length of the drop measured along the axis of symmetry and B is the maximum breadth in the transverse direction. They are computed by the approach of Breyyiannis [48]. In his approach, a deformed capsule is mapped to an ellipse who shares the tensor of the moments of inertia. The principle direction of the tensor is identified as the capsule's inclination angle θ, measured with respect to the horizontal direction of flow.

The deformation of an elastic capsule is examined in the simulation. A square computational domain $\Omega = [-4,4] \times [-4,4]$, has 321 nodes in both the dimensions of the shear flow and the transverse direction. The uniform grid length was $h = 2.5\mu m$ and the timestep $\Delta t = 2.5\mu s$. The Reynolds number based on characteristic length and velocity is 0.05, where viscous forces are dominant, and is characterized by smooth, constant fluid motion. The capsule is placed at the center of the domain and its membrane is initially discretized into 140 Lagrangian nodes, such that each segment is of equal length. The initial shear flow, continuously enforced on the domain boundaries is $\vec{u} = (ky, 0)$ for shear rate $k = 10^{-4}s^{-1}$ and $y \in [-4,4]$. All variables are normalized by the characteristic length $2a$, velocity $2ka$, time $1/k$ and tension μka, where a is the radius of the capsule, μ is the viscosity of the ambient fluid. Capsule deformation is studied in terms of the Taylor deformation parameter.

The present results demonstrate that the capsule deforms to a steady shape and then the membrane rotates around the liquid inside which is so called tank-treading motion. We observed single eddy inside the capsule and recirculation external flows via the velocity field in Figure 18, at the time when the capsule achieved steady state with $Ca = 0.0125$.

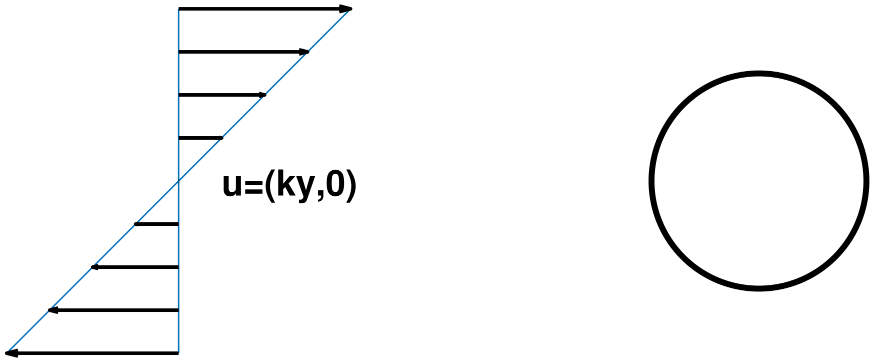

Figure. 17: Schematic illustration of a two-dimensional capsule in simple shear flow.

The results from the two dimensional algorithms are compared with previous of Breyiannis and Pozrikidis (2000) by boundary element method [48]. Figure 19 considers the deformation of an elastic capsule, with respect to the Taylor deformation parameter, for different capillary numbers Ca. The results agree very well, even for higher capillary number $Ca = 0.4$. The time taken to achieve steady state is shorter for lower capillary number, since lower rate indicate larger elastic modulus, so a small deformation can generate enough elastic force to balance the viscous shear-force.

4.2 NUMERICAL VALIDATION FOR ELECTROHYDRODYNAMIC SIMULATION

In present section, we will perform a series of numerical tests for practical purpose. The convergence of the electric potential and the interfacial electric force are investigated. Then the comparison with small deformation theory is performed through running a series of simulations with different permittivity ratios $\varepsilon_r = \frac{\varepsilon^-}{\varepsilon^+}$ and conductivity ratio $\sigma_r = \frac{\sigma^-}{\sigma^+}$.

The initial set-up of the simulation is the same as in [20]. An interfacial tension circular drop with radius $R = 1$ is placed at the center $(0,0)$ of the fluid domain $\Omega = [-4,4] \times [-4,4]$ and initial velocity of the fluid is set to be zero everywhere. The flow is completely driven by the electric field. The initial velocity field is zero. The electric field $\mathbf{E}_\infty$, far from the drop, is set to be $(0,-1)$. The

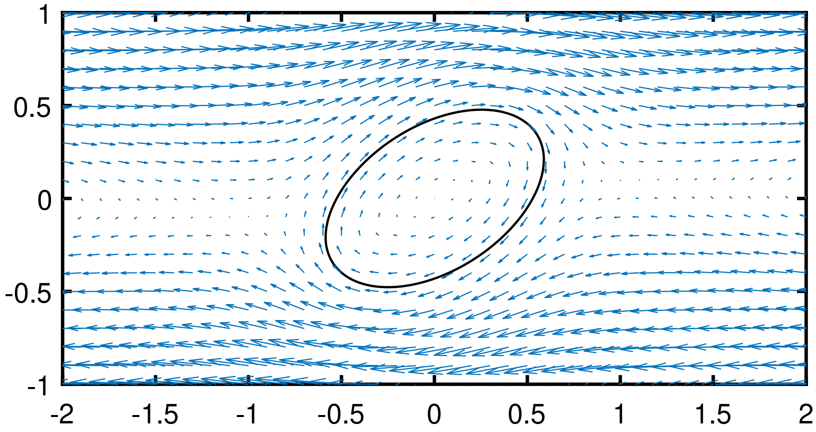

Figure. 18: Fluid field and the shape of deformed capsule with no bending at steady state , $Ca = 0.0125$.

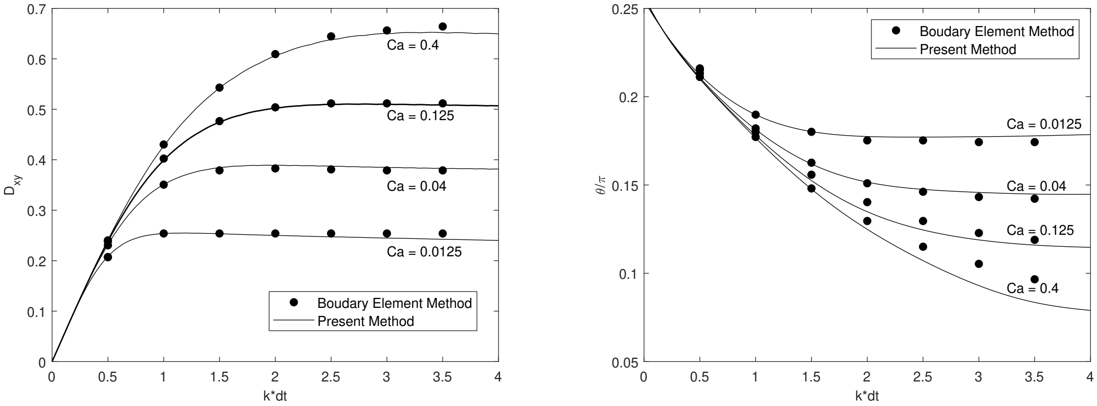

Figure. 19: Comparison with Boundary Element Method (Breyiannis and Pozrikidis, 2000)

boundary conditions for the potential ϕ are $\phi = y$ (Dirichlet) at $y = \pm 4$, and $\frac{\partial \phi}{\partial x} = 0$ (Neumann) at $x = \pm 4$. The number of Lagrangian control points is M on the immersed interface Σ. It has been

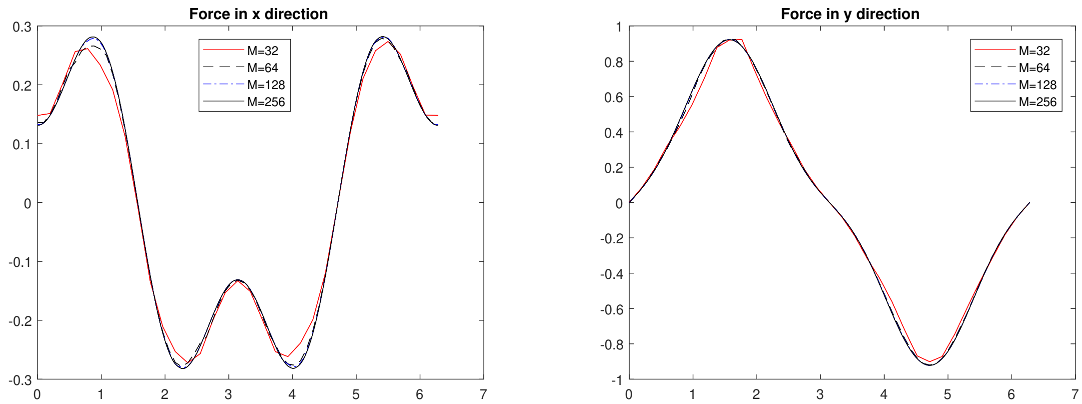

Figure. 20: Electric force $\mathbf{F}_e$ at different number of Lagrangian control points: $M = 32, 64, 128, 256$. To the left is $\mathbf{F}_x$, and to the right is $\mathbf{F}_y$.

addressed in [20] that the Lagrangian mesh Δs, should satisfy $\Delta s = 2\pi/M < h$, where $h = 8/N$ is the Cartesian grid mesh width. In our simulation, $N = 8/h < 8M/2\pi$ is guaranteed. Although the exact solution is unavailable for our simulation, the solution for 512 Lagrangian control points, $(\mathbf{F_E})_{512}$ is referred as analytic solution. Then we verify the order of convergence by computing successive errors defined by $||(\mathbf{F_E})_{2N} - (\mathbf{F_E})_{512}||_\infty$ versus the Cartesian mesh size N.

4.2.1 CONVERGENCE TEST FOR THE INTERFACIAL ELECTRIC FORCE

In present simulation, we chose $\sigma_r = 3$ and $\varepsilon_r = 2$ and plot $\mathbf{F}_E$ with different number of Lagrangian markers $M = 32, 64, 128$ and 256. One can see that the interfacial electric force tends to converge as the marker size M increases, roughly second order convergence observed. Table 10 shows the convergence test results of initial electric force.

TABLE 10: Convergence test for $\mathbf{F}_x$ and $\mathbf{F}_y$

N	$\|\|(\mathbf{F}_x)_N - (\mathbf{F}_x)_{512}\|\|_\infty$	Rate	Order	$\|\|(\mathbf{F}_y)_N - (\mathbf{F}_y)_{512}\|\|_\infty$	Rate	Order
32	$2.13141e-02$			$4.24485e-02$		
64	$5.12620e-03$	4.15788	2.05585	$8.45450e-03$	5.02081	2.32792
128	$2.22769e-03$	2.30113	1.20234	$3.47598e-03$	2.43226	1.28230
256	$6.91200e-04$	3.22293	1.68837	$9.08762e-04$	3.82497	1.93545

4.2.2 NUMERICAL VALIDATION

To validate our proposed model and numerical method, we compared our results with the theoretical analysis given by Feng [49], based on Taylor's small-deformation theory. In Feng's analysis, the capsule is considered as an interfacial tension drop. He develop a linear model to describe the steady equilibrium shape of a leaky dielectric drop immersed in a DC electric field. The characterized deformation parameter is defined as in (4.1).

In the first-order small-deformation analysis for a two-dimensional interfacial tension drop, the equilibrium drop deformation is approximated by

$$D = \frac{\sigma_r^2 + \sigma_r + 1 - 3\varepsilon_r}{3(1+\sigma_r)^2} Ca_E$$

Define $f_d(\sigma_r, \varepsilon_r) = \sigma_r^2 + \sigma_r + 1 - 3\varepsilon_r$, and f_d is called discriminating function, which was first found by Rhodes and Saville for electro-hydrodynamic distortion of a particulate stream in continuous flow electrophoresis. The equilibrium drop shape is related to the discriminating function. When $f_d > 0$, the drop turns into a prolate shape, while $f_d < 0$, the drop will deform into an oblate shape.

The initial velocity are set to be zero everywhere and the flow is completely driven by the electric field. We set the fluid viscosity $\mu = 1/240$, the surface tension $\gamma = 1/240^2$ and the density of fluid $\rho = 1$. Hence the dimensionless Ohnesorge number for the flow, $Oh = \mu/\sqrt{\gamma\rho R}$, which measures the ratio of inertial forces to viscous forces is simply computed as $Oh = 1$. For an interfacial tension capsule, the membrane surface energy is proportional to its area with the interfacial tension γ as the proportionality constant [14]. Therefore, the dimensionless capillary number is defined in terms of the interfacial tension. The electric capillary number $Ca_E = \varepsilon^+ R|E_\infty|^2/\gamma$, measures the strength of the electric field relative to the surface tension force. In latter sections, when considering capsules involving viscoelastic membrane (red blood cell), the electric capillary number is redefined in terms of elastic modulus, and the fluid capillary number is Ca in stead of Ohnesorge number.

To best understand the capsule deformation pattern with different combination of electric parameters σ_r and ε_r, a series of simulations have been performed for $Oh = 1$. They are labeled as Case A ($\sigma_r = 1.75, \varepsilon_r = 3.5$), Case B ($\sigma_r = 3.25, \varepsilon_r = 3.5$) and Case C ($\sigma_r = 4.75, \varepsilon_r = 3.5$). For these three cases, we conduct the simulations with different electric capillary number Ca_E. Figure

21a shows the deformation number D versus the electric capillary number Ca_E for three cases. Negative deformation number indicate that the capsule has an increased length in the radial direction (refer to case A), while positive deformation number reveal an increased length of the capsule in the axial direction (refer to case B and case C).

As illustrated in [13], the induced flow inside the capsule in the first quadrant is clockwise while the shape of capsule is elongated along the radial direction (case A). Figure 23 shows such a phenomenon with $Ca_E = 1$. However, we observed counterclockwise induced circulatory flow for case B and clockwise flow for case C, whereas the capsule is elongated along the axial direction in both case B and case C. The simulations confirm Taylor's theory in [13]. The flow pattern is related to the regions determined by f_d and $\sigma_r = \varepsilon_r$. In Figure 22, while in region A ($f_d > 0$, $\varepsilon_r > \sigma_r$), we observe prolate-type deformation (elongated along the radial direction) and clockwise flow; In both regions B and C (elongated along the axial direction), the capsule deforms to oblate-type shape, but the circulatory flow is clockwise for region B and counterclockwise for region C.

As shown in previous simulation, the axis of symmetry of the capsule is always parallel to the direction of the externally applied electric field when the capsule is driven by the electric field induced flow. In the following section, we consider the capsule immersed in the electric field and shear flow, the capsule deformation and orientation will be affected by the relative strength of the shear and electric stresses.

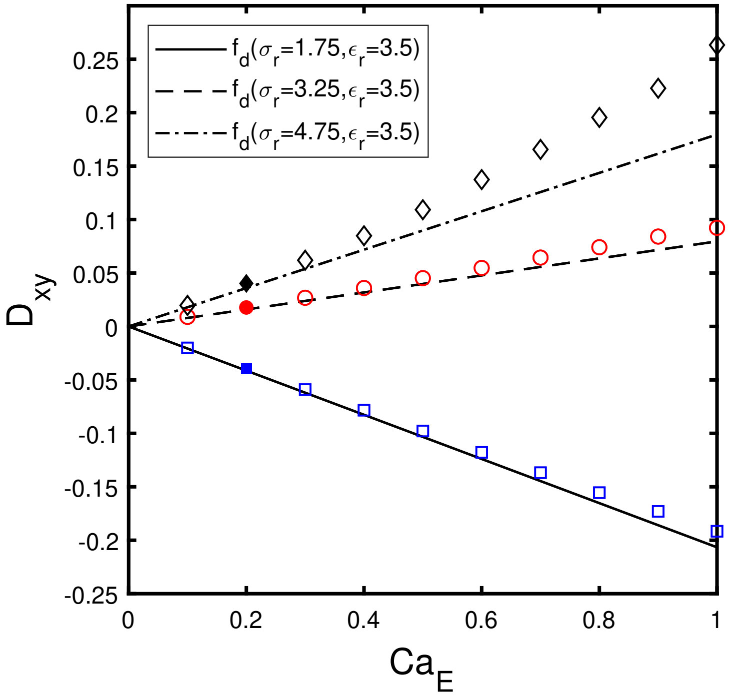

(a)

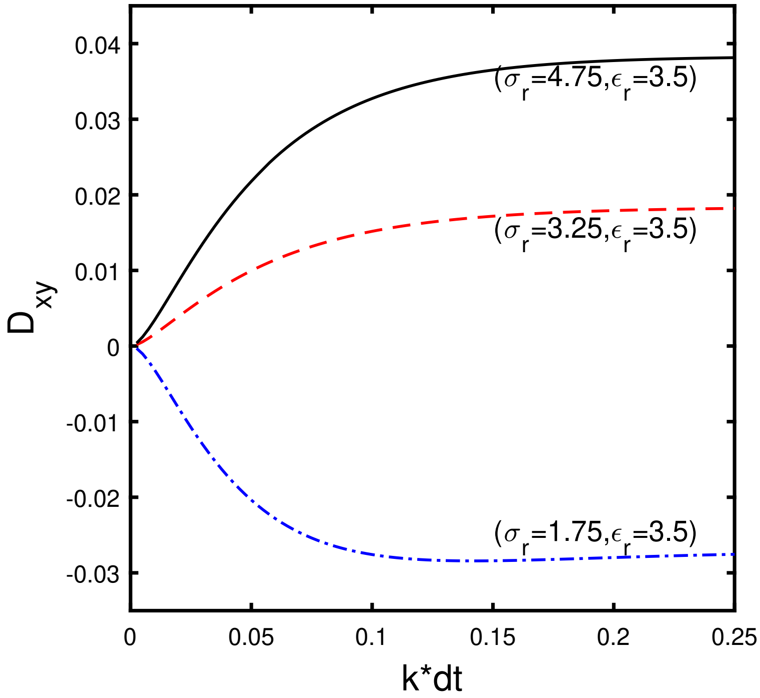

(b)

Figure. 21: (a) The plot of the deformation number D_{xy} versus the capillary number for Case A $(\square, \sigma_r = 1.75, \varepsilon_r = 3.5)$, Case B $(\bigcirc, \sigma_r = 3.25, \varepsilon_r = 3.5)$ and Case C $(\lozenge, \sigma_r = 4.75, \varepsilon_r = 3.5)$. (b) Deformation evolution of cases A, B and C for the same capillary number $Ca_E = 0.2$.

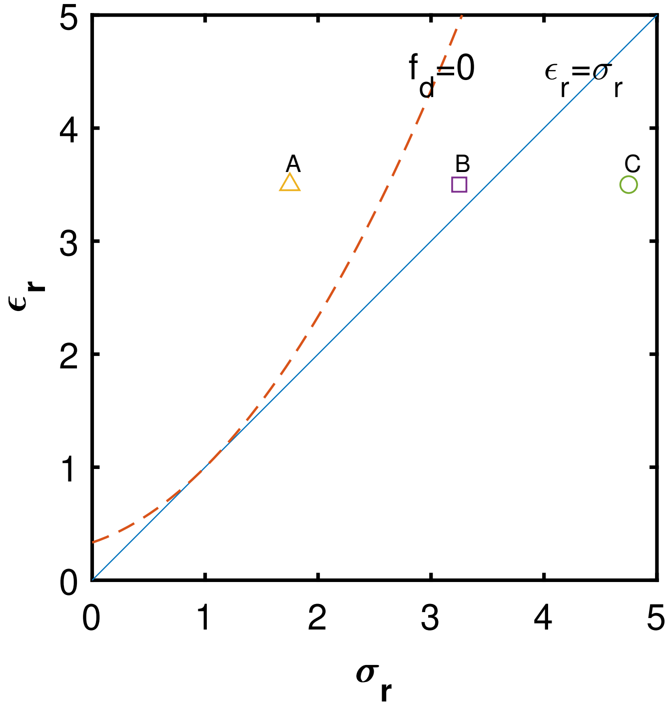

Figure. 22: The capsule deformation for different combinations of conductivity ratio σ_r and permittivity ratio ε_r.

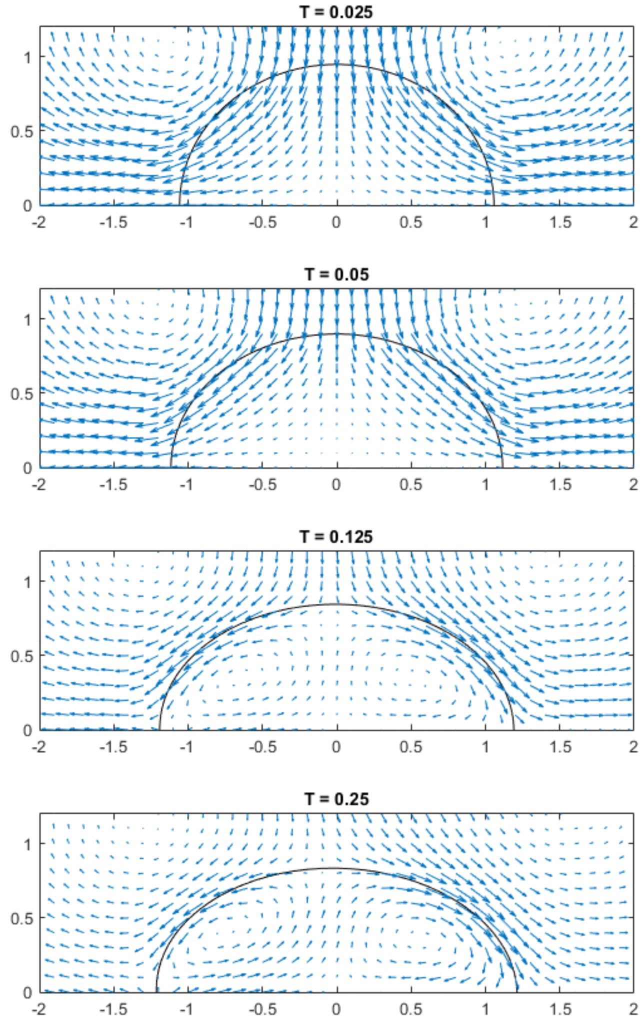

Figure. 23: Deformation and velocity field for the case A $(\sigma_r = 1.75, \varepsilon_r = 3.5)$ at different times with $Ca_E = 1$.

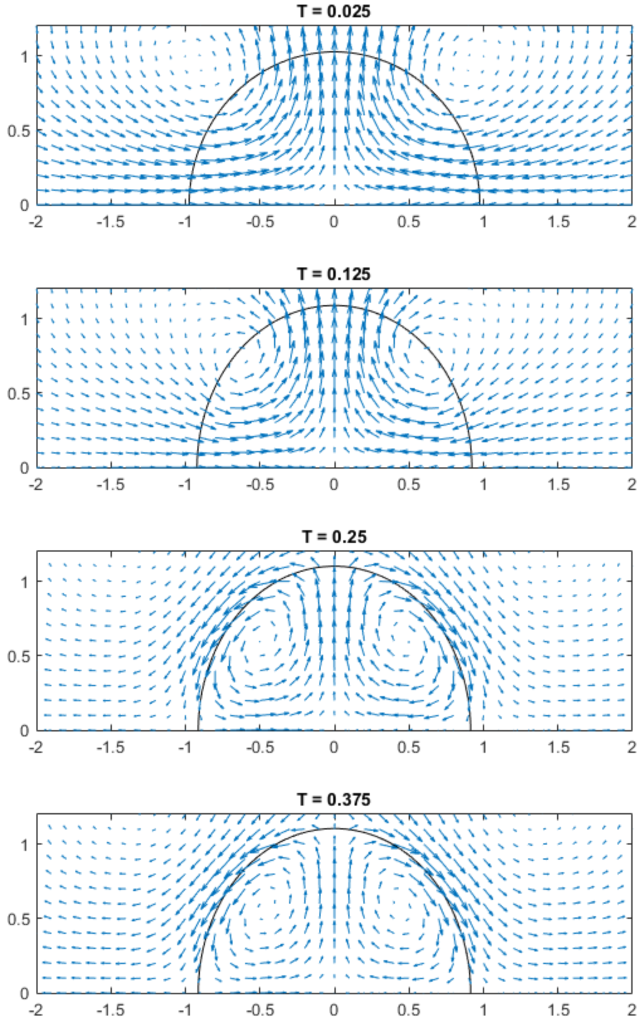

Figure. 24: Deformation and velocity field for the case B $(\sigma_r = 3.25, \varepsilon_r = 3.5)$ at different times with $Ca_E = 1$.

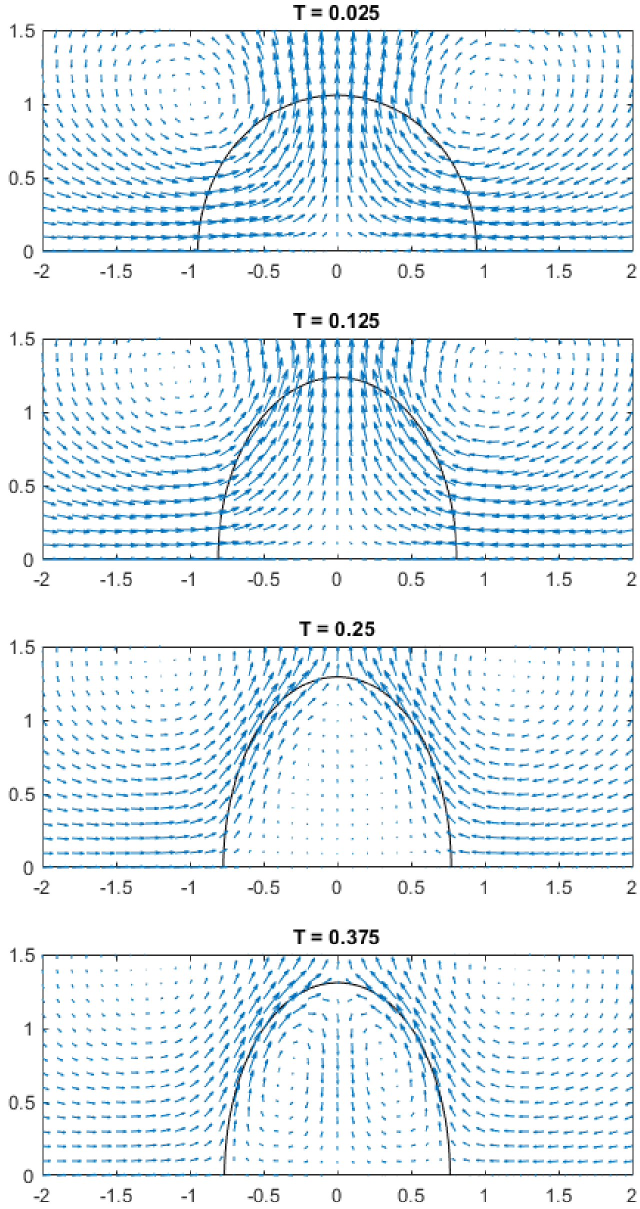

T = 0.025

T = 0.125

T = 0.25

T = 0.375

Figure. 25: Deformation and velocity field for the case C $(\sigma_r = 4.75, \varepsilon_r = 3.5)$ at different times with $Ca_E = 1$.

4.3 NUMERICAL SIMULATION ON THE DEFORMATION OF INTERFACIAL TENSION CIRCULAR CAPSULE UNDER SHEAR FLOW

In this section, we consider adding simple shear flow simultaneously to the interfacial tension droplet, and the deformation and orientation will be affected by the relative strength of the shear and electric stresses (Figure 26). The radius of initial undeformed drop is 1. It has been confirmed, an individual Newtonian fluid drop is oriented at 45° with respect to the flow direction at the leading order [50]; the orientation angle will change when the high-order impact is included. On the other hand, it has been validated that, the axis of symmetry of the deformed drop shape is aligned parallel to the electric field for either prolate or oblate deformation in the absence of the shear flow. One might have the thoughts when the drop is subject to the electric field and shear flow simultaneously, the orientation angle of the major axis of the drop varies from $\theta/\pi = 0$ to $\theta/\pi = 0.25$ aligned with the flow direction when the oblate-type deformation is generated. While the prolate type deformation is involved, the orientation angle should lie between $\theta/\pi = 0.25$ and $\theta/\pi = 0.5$. If the shear flow is dominant, the orientation angle should be close to $\theta/\pi = 0.25$ since the shear force is at leading order. We're interested in the case that, the electric force is competitive to the shear force. To this purpose, the initial shear flow is set to be $\vec{u} = (ky, 0)$ for the shear rate $k = 0.00125$.

Under the electric field with strength $Ca_E = 1$ and the shear flow, in Figure 27, the drop tends to tilt horizontally along the shear flow direction while it shows oblate shape (Case A) in the simulation in previous section. The shape deformation is slightly greater than in the absence of electric field. Orientation angle is between $\theta/\pi = 0$ and $\theta/\pi = 0.25$, which confirm the behavior for oblate-type deformation. In Figure 28, the drop tends to tilt vertically along the transverse direction against shear flow and confirm that orientation angle is initially between $\theta/\pi = 0.25$ and $\theta/\pi = 0.5$ for prolate deformation (Case B), and greater than the angle when $Ca_E = 0$. For Case C, it is aligned along the shear flow direction as Case B initially; when deformation proceed, it is observed the orientation angle is less than the angle for $Ca_E = 0$ (Figure 29). The main reason is that, the shear force is no longer dominant if compared with electric force. It can be seen from Figure 30, Case C generates a significantly deformed capsule than Case A and Case B, which also confirm that the electric force is more dominant than shear flow.

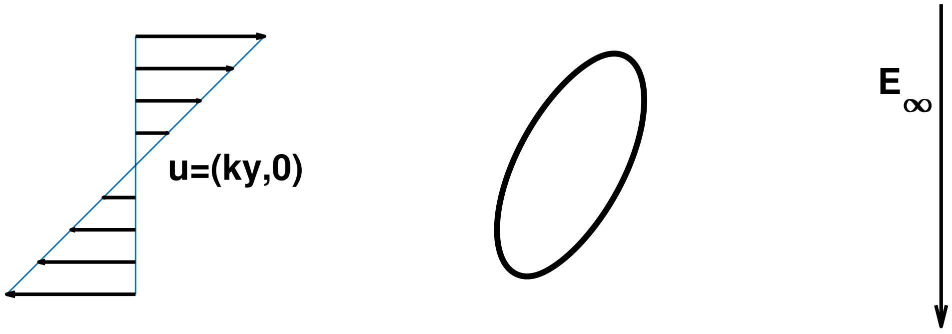

Figure. 26: Schematic illustration of a two-dimensional capsule in simple shear flow and DC electric field.

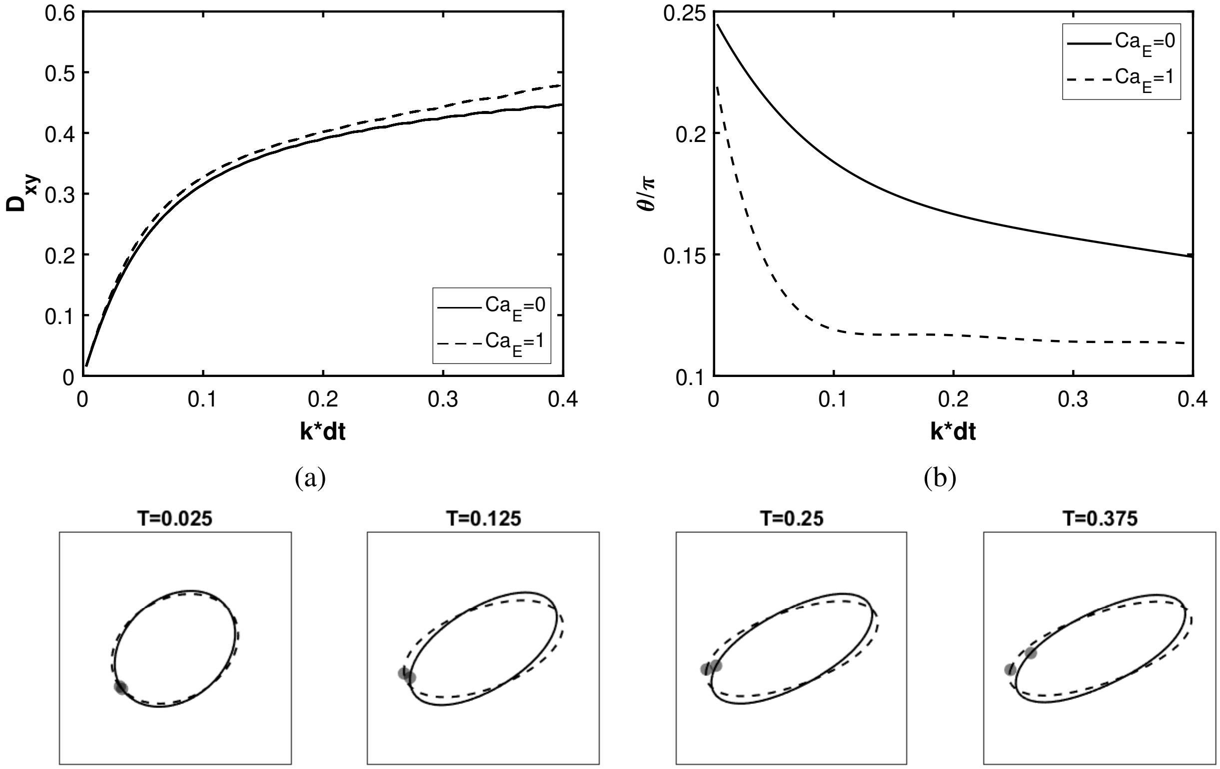

(a)

(b)

(c)

Figure. 27: The deformation behavior of interfacial tension drop, Case A: $\sigma_r = 1.75$, $\varepsilon_r = 3.5$. (a) Temporal evolution of Taylor deformation parameter. (b) Temporal evolution of inclination angle. (c) Shape evolution.

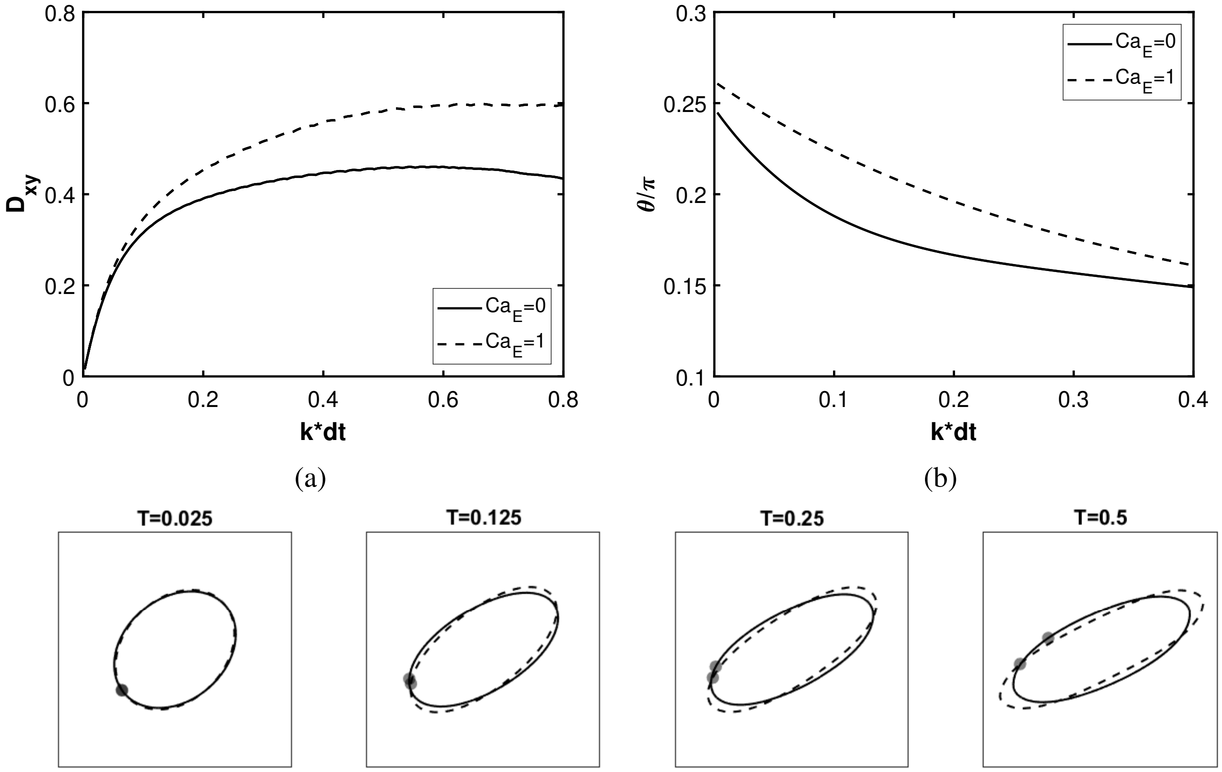

(a)

(b)

(c)

Figure. 28: The deformation behavior of interfacial tension drop, Case B: $\sigma_r = 3.25$, $\varepsilon_r = 3.5$. (a) Temporal evolution of Taylor deformation parameter. (b) Temporal evolution of inclination angle. (c) Shape evolution.

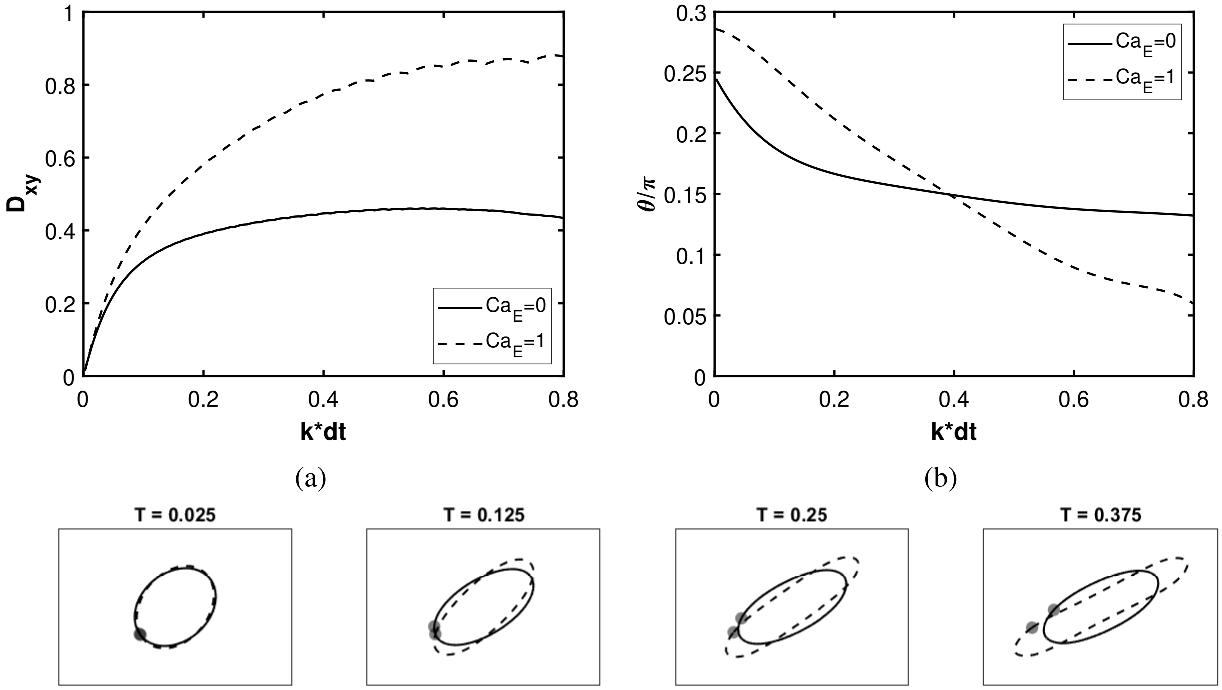

(a)

(b)

(c)

Figure. 29: The deformation behavior of interfacial tension drop, Case A: $\sigma_r = 4.75$, $\varepsilon_r = 3.5$. (a) Temporal evolution of Taylor deformation parameter. (b) Temporal evolution of inclination angle. (c) Shape evolution. (d) Shape deformation at $T = 0.6$.

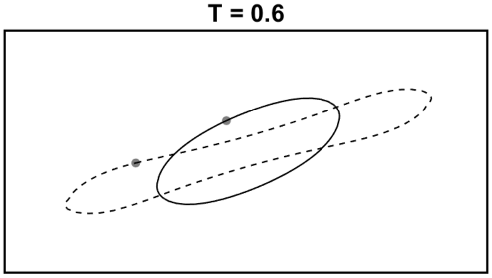

Figure. 30: Shape deformation at $T = 0.6$ for Case C: $\sigma_r = 4.75$, $\varepsilon_r = 3.5$.

CHAPTER 5

ELECTRIC EFFECT ON THE DEFORMATION OF IMMERSED CAPSULES

5.1 ELECTRIC EFFECT ON THE DEFORMATION OF VISCOELASTIC CIRCULAR CAPSULE UNDER SHEAR FLOW

In previous section, the numerical algorithms for the simulation of capsule under just shear flow and the deformation of capsule under DC electric field induced flow have been validated. In this section, we perform a series of numerical simulation to study the deformation of capsule under the effect of both shear flow and DC electric field. When an elastic capsule immersed in the shear flow, the flexible membrane rotates in the same direction of shear flow due to non-slip boundary condition. The capsule will start deforming until reach steady state. By coupling electric field, the capsule will be more deformed and achieve steady state more quickly. The capsule reaches steady state when shear force, electrical force and body force are balanced, but the membrane still rotate around the fluid filled in capsule; this is known as tank-treading motion.

The initial set up of numerical simulation is similar as in Chapter 4. As mentioned previously, when considering the elastic red blood cell type membrane, the electric capillary number is defined as $Ca_E = \varepsilon^+ R|E_\infty|^2/E_s$, where E_s is the elastic modules of the membrane; the fluid capillary number is $Ca = \mu_a ka/E_s$, in terms of ambient fluid viscosity μ_a, shear rate k, equivalent capsule radius a and E_s.

The simulations with the following combinations of permittivity and conductivity ratios are conducted: Case A ($\sigma_r = 1.75$, $\varepsilon_r = 3.5$), Case B ($\sigma_r = 3.25$, $\varepsilon_r = 3.5$) and Case C ($\sigma_r = 4.75$, $\varepsilon_r = 3.5$).

The discriminate function $f_d(\sigma, \varepsilon_r) = \sigma_r^2 + \sigma_r + 1 - 3\varepsilon_r$, indicates that, under $\sigma_r = 1.75$, $\varepsilon_r = 3.5$, the prolate shape and induced counterclockwise flow are obtained when the capsule achieves equilibrium state under a DC electric field $\mathbf{E}_\infty$. By adding the shear flow $\vec{u} = (ky, 0)$, we perform the simulation by considering different electric capillary number Ca_E on the evolution of the capsule. The results demonstrate that the deformation is monotonically increasing with increased Ca_E and yield more deformed equilibrium shape. In addition, the time to achieve equilibrium state decreases with increased Ca_E, and they are shorter than without electric field (under shear flow only). In Figure 31a, for the Case A ($\sigma_r = 1.75$, $\varepsilon_r = 3.5$), while capsule deforms to an ellipsoidal equilibrium shape in the absence of electric field under $Ca = 0.04$, the capsule continues to elongate by adding electric field and gradually increases with increased Ca_E. We observe the same phenomenon in Case B ($\sigma_r = 3.25$, $\varepsilon_r = 3.5$) (Figure 33a) and Case C ($\sigma_r = 4.75$, $\varepsilon_r = 3.5$) (Figure 35a). Under weaker shear flow ($Ca = 0.0125$), the capsule is less deformed (Figure 37a,Figure 39a,Figure 41a). Also, it can be seen that the capsule tends to tilt horizontally along the shear flow in Case A, while for Case B and Case C, the capsule tends to tilt vertically. In Figure 43, Figure 44 and Figure 45, a single clockwise vortical swirl flow is formed inside the capsule, and Case B and Case C show stronger swirl flow than Case A, since they both tend to tilt vertically against the shear flow.

As shown in Figure 46, 47 and 48, the capsule membrane starts rotating around its fluid inside with period T. The normalized tank treading frequency, $f = 4\pi/(kT)$, is presented in Figure 49, Figure 50 and Figure 51 for Case A, Case B and Case C, respectively. No significant difference can be seen from Case A and Case B; but for more deformed capsule in Case C, we can see higher frequency. The reason is, under stronger combined electric force and shear force, stronger flow are generated and speed up the tank treading phenomenon.

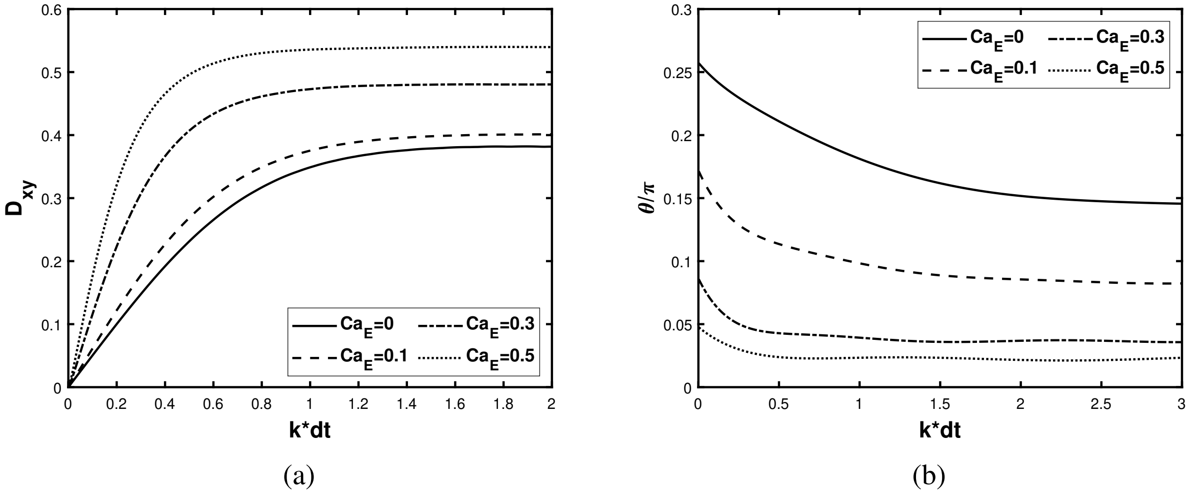

Figure. 31: $Ca = 0.04$, Case A: $\sigma_r = 1.75$, $\varepsilon_r = 3.5$. (a) Temporal evolution of Taylor deformation parameter. (b) Temporal evolution of inclination angle.

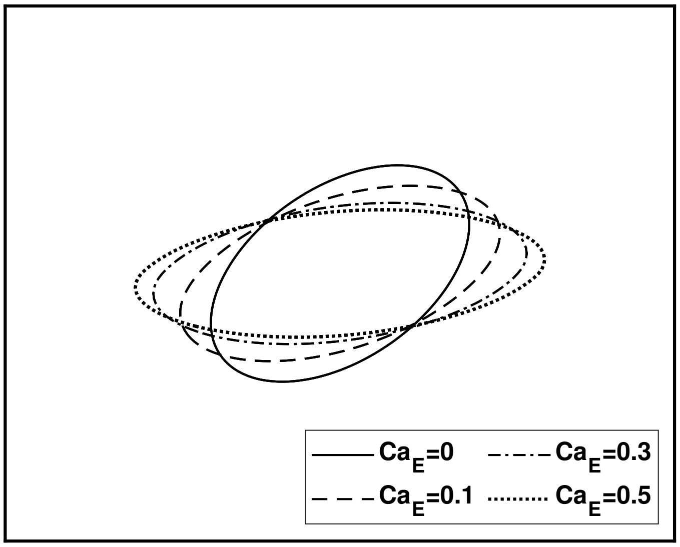

Figure. 32: Equilibrium shape of deformed capsule for Case A: $\sigma_r = 1.75$, $\varepsilon_r = 3.5$ under shear flow $Ca = 0.04$ and various electric strengths.

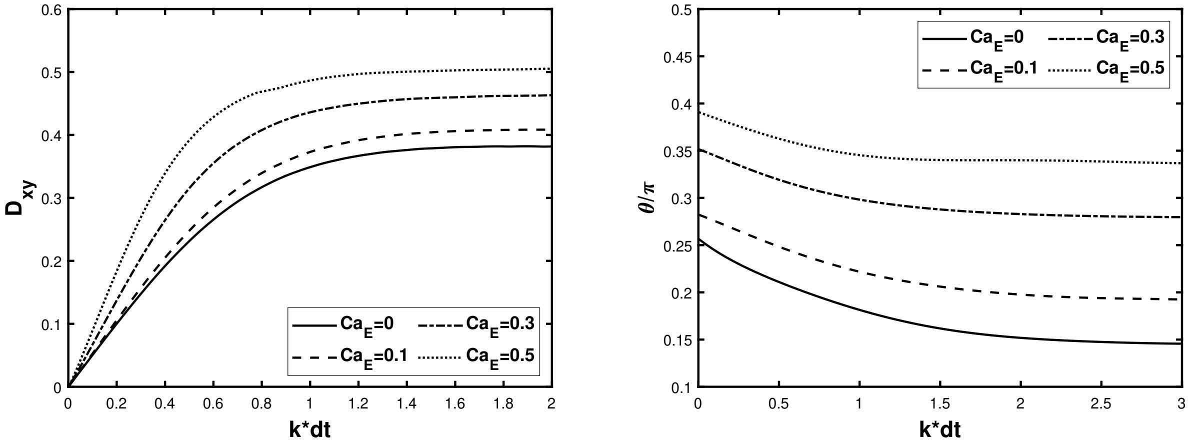

(a)

(b)

Figure. 33: $Ca = 0.04$, Case B: $\sigma_r = 3.25$, $\varepsilon_r = 3.5$. (a) Temporal evolution of Taylor deformation parameter. (b) Temporal evolution of inclination angle.

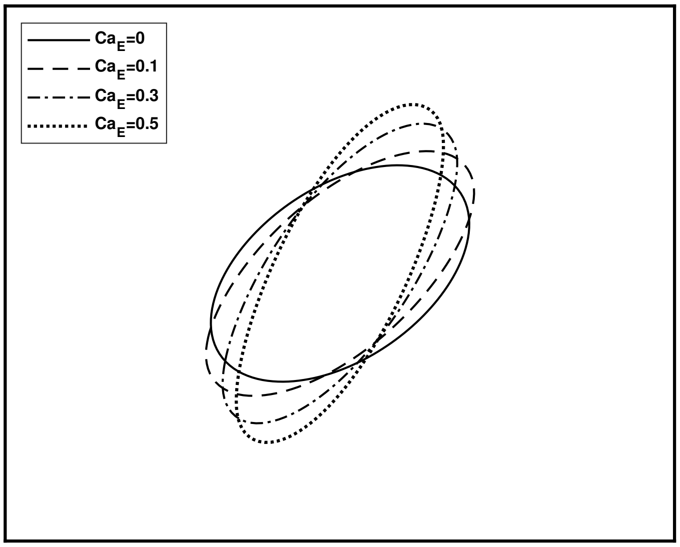

Figure. 34: Equilibrium shape of deformed capsule for Case B: $\sigma_r = 3.25$, $\varepsilon_r = 3.5$ under shear flow $Ca = 0.04$ and various electric strengths.

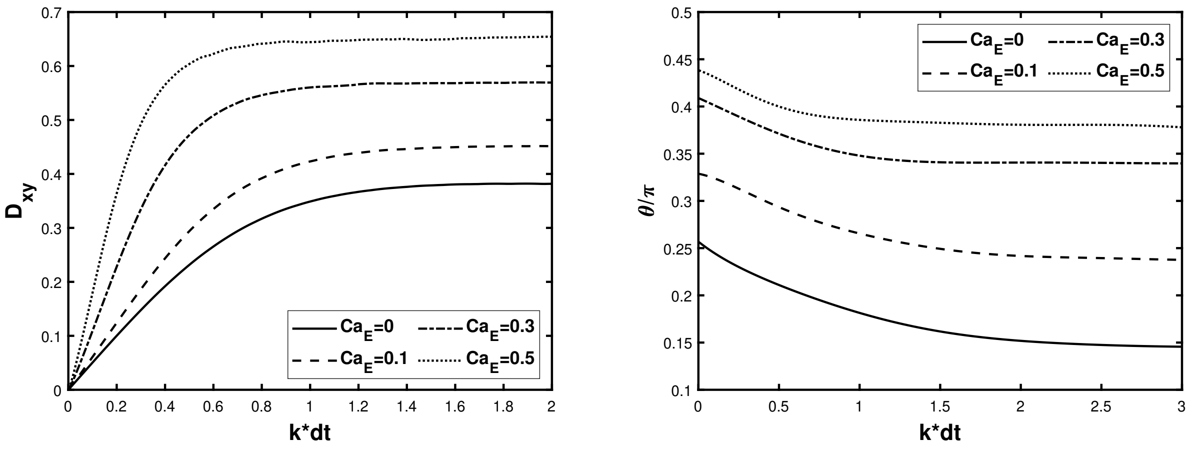

(a) (b)

Figure. 35: $Ca = 0.04$, Case C: $\sigma_r = 4.75$, $\varepsilon_r = 3.5$. (a) Temporal evolution of Taylor deformation parameter. (b) Temporal evolution of inclination angle.

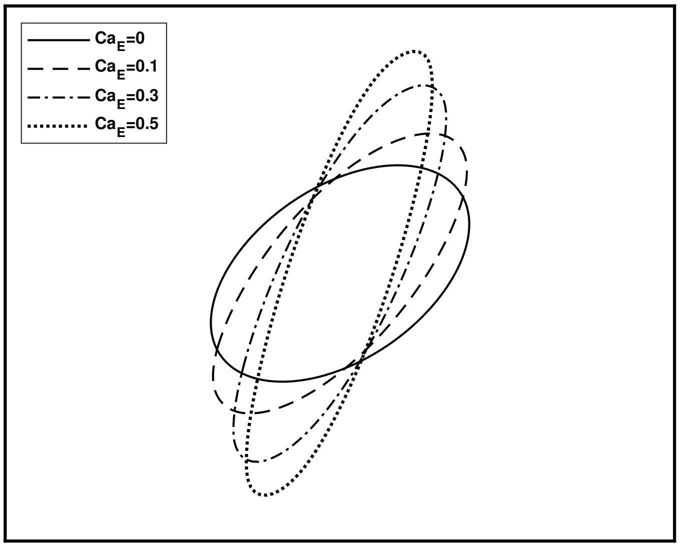

Figure. 36: Equilibrium shape of deformed capsule for Case C: $\sigma_r = 4.75$, $\varepsilon_r = 3.5$ under shear flow $Ca = 0.04$ and various electric strengths.

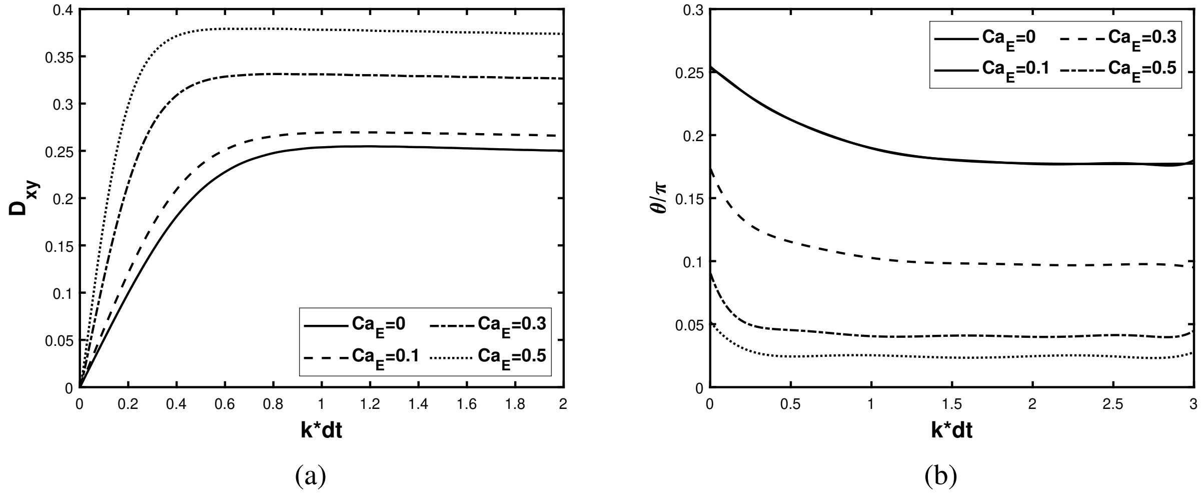

(a) (b)

Figure. 37: $Ca = 0.0125$, Case A: $\sigma_r = 1.75$, $\varepsilon_r = 3.5$. (a) Temporal evolution of Taylor deformation parameter. (b) Temporal evolution of inclination angle.

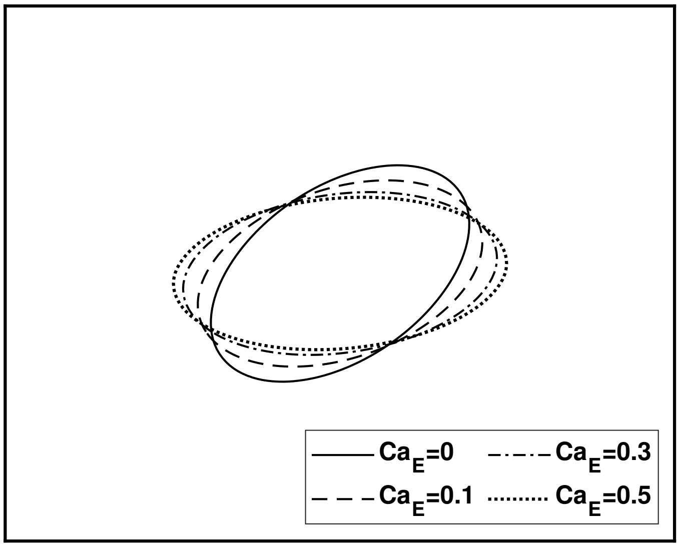

Figure. 38: Equilibrium shape of deformed capsule for Case A: $\sigma_r = 1.75$, $\varepsilon_r = 3.5$ under shear flow $Ca = 0.0125$ and various electric strengths.

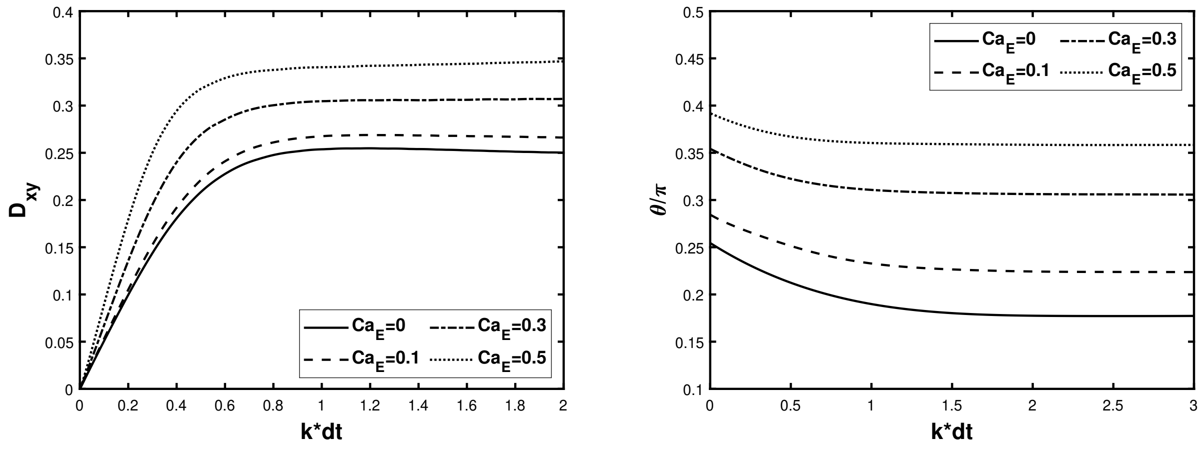

(a) (b)

Figure. 39: $Ca = 0.0125$, Case B: $\sigma_r = 3.25$, $\varepsilon_r = 3.5$. (a) Temporal evolution of Taylor deformation parameter. (b) Temporal evolution of inclination angle.

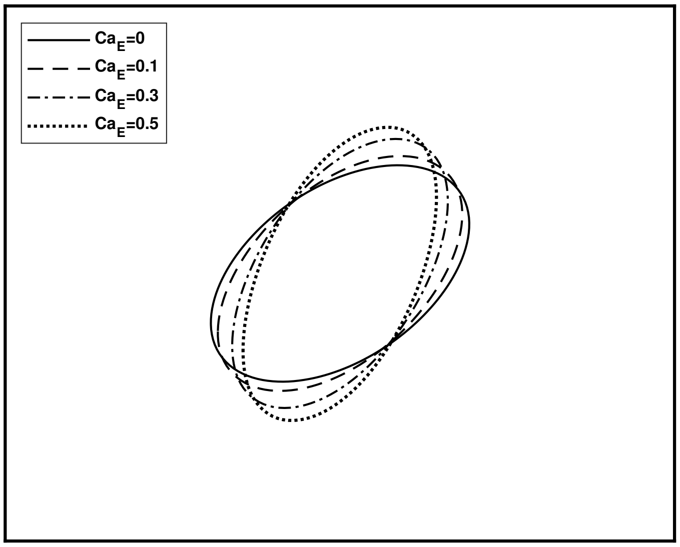

Figure. 40: Equilibrium shape of deformed capsule for Case B: $\sigma_r = 3.25$, $\varepsilon_r = 3.5$ under shear flow $Ca = 0.0125$ and various electric strengths.

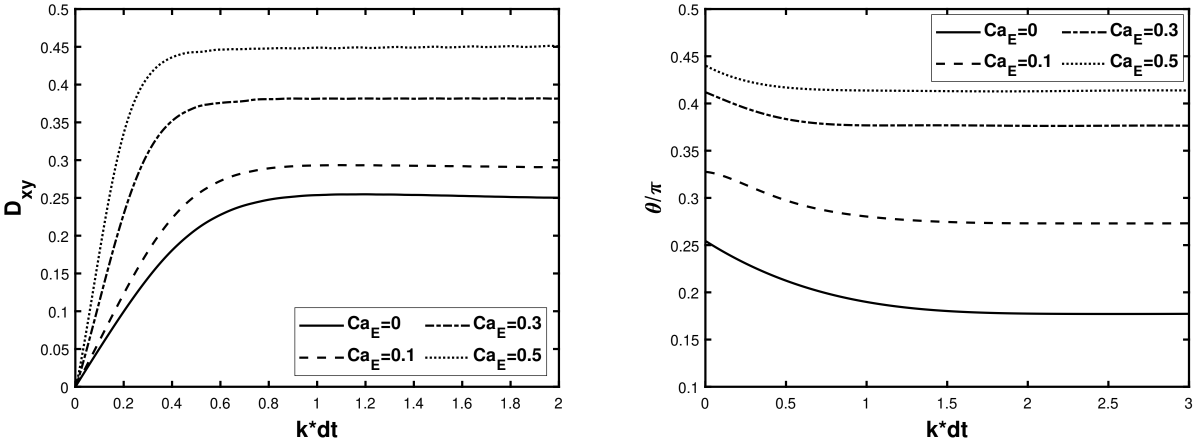

(a)

(b)

Figure. 41: $Ca = 0.0125$, Case C: $\sigma_r = 4.75$, $\varepsilon_r = 3.5$. (a) Temporal evolution of Taylor deformation parameter. (b) Temporal evolution of inclination angle.

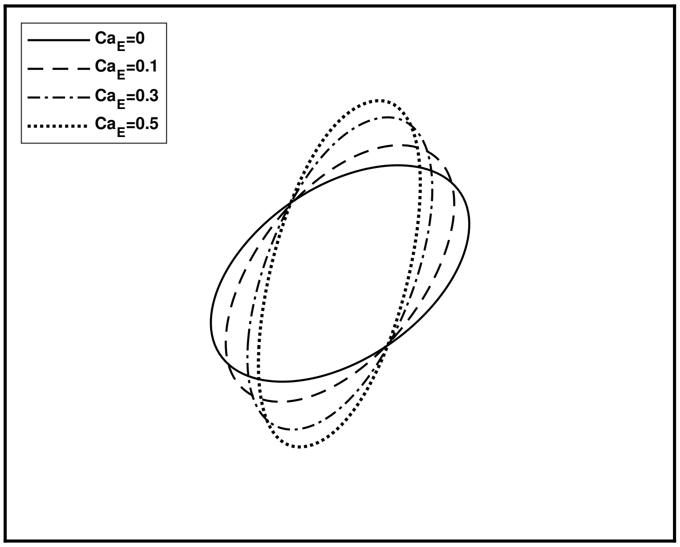

Figure. 42: Equilibrium shape of deformed capsule for Case C: $\sigma_r = 4.75$, $\varepsilon_r = 3.5$ under shear flow $Ca = 0.0125$ and various electric strengths.

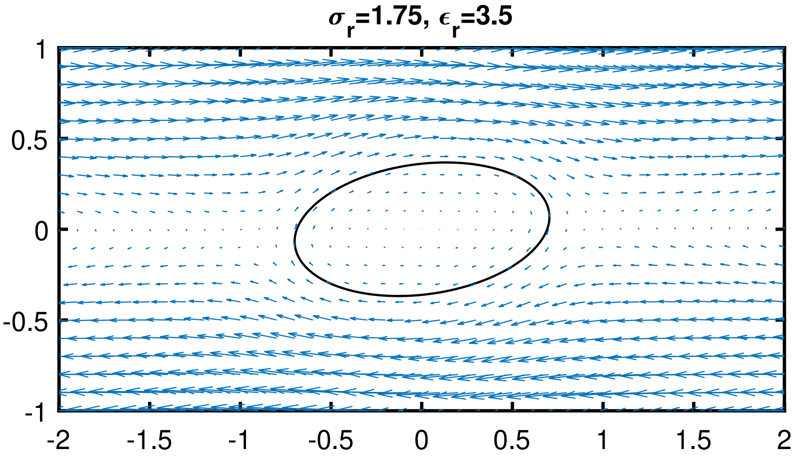

Figure. 43: Fluid field and the shape of deformed capsule for Case A ($\sigma_r = 1.75$, $\varepsilon_r = 3.5$), $Ca_E = 0.3$, $Ca = 0.0125$.

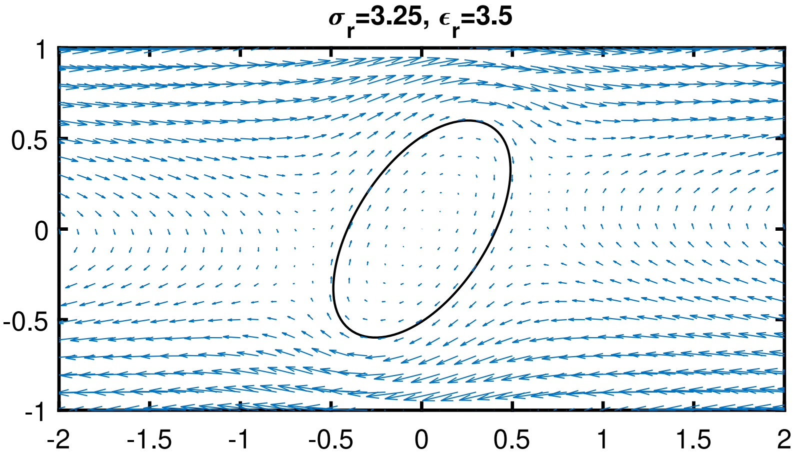

Figure. 44: Fluid field and the shape of deformed capsule for Case B ($\sigma_r = 3.25$, $\varepsilon_r = 3.5$), $Ca_E = 0.3$, $Ca = 0.0125$.

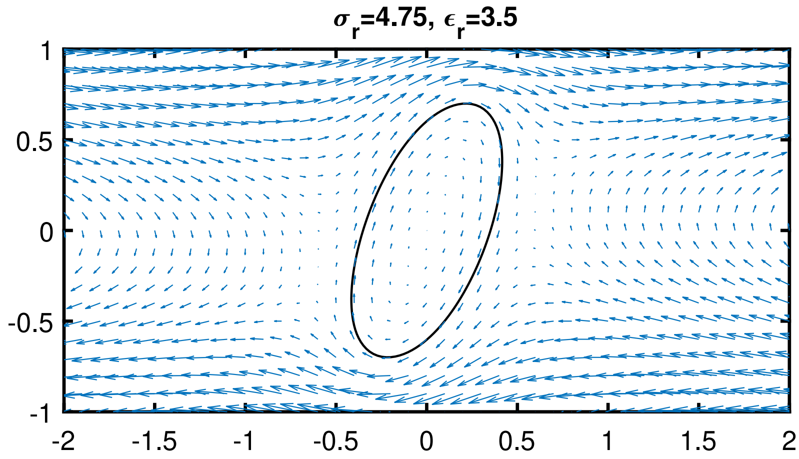

Figure. 45: Fluid field and the shape of deformed capsule for Case C ($\sigma_r = 4.75$, $\varepsilon_r = 3.5$), $Ca_E = 0.3$, $Ca = 0.0125$.

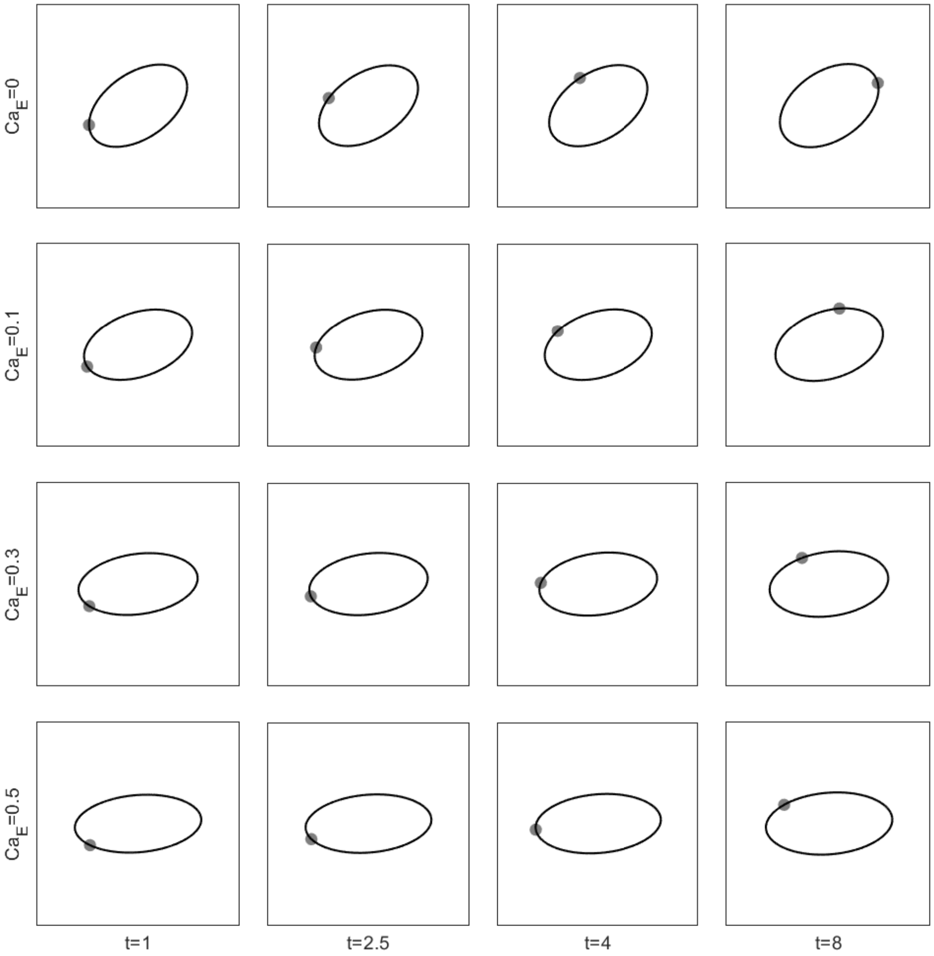

Figure. 46: Tank-treading phenomenon for Case A ($\sigma_r = 1.75$, $\varepsilon_r = 3.5$), $Ca = 0.0125$, under various strength of electric field.

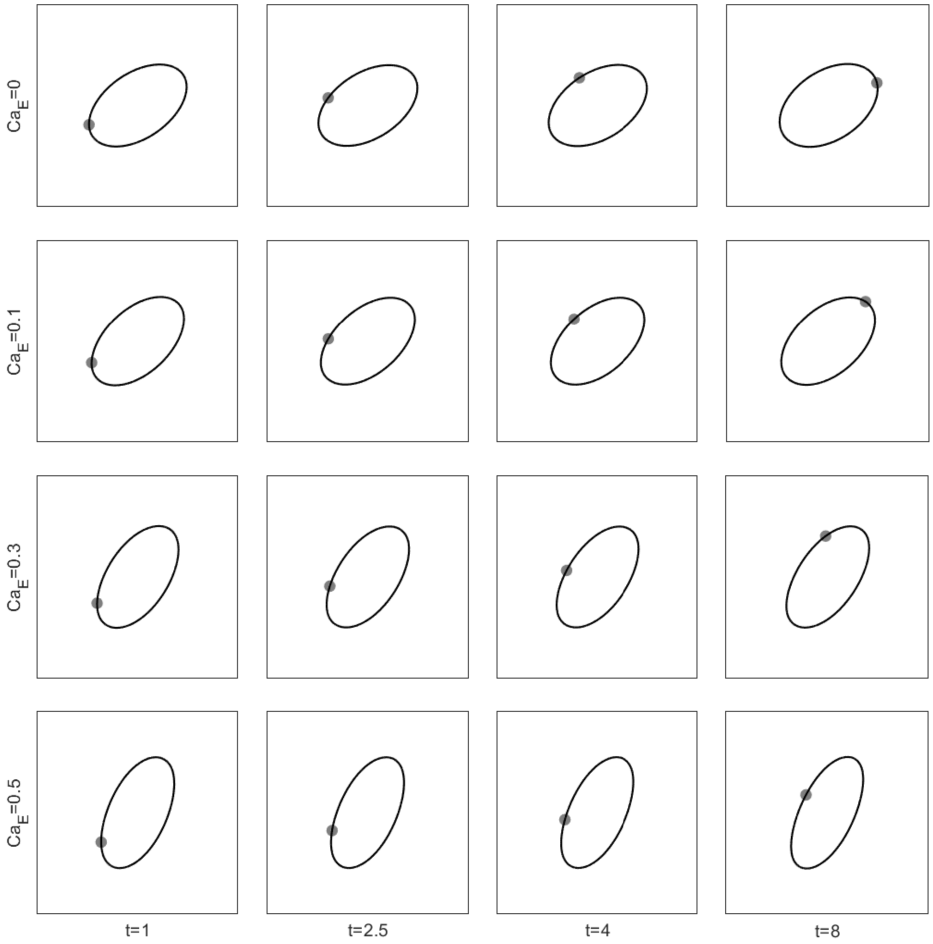

Figure. 47: Tank-treading phenomenon for Case B ($\sigma_r = 3.25$, $\varepsilon_r = 3.5$), $Ca = 0.0125$, under various strength of electric field.

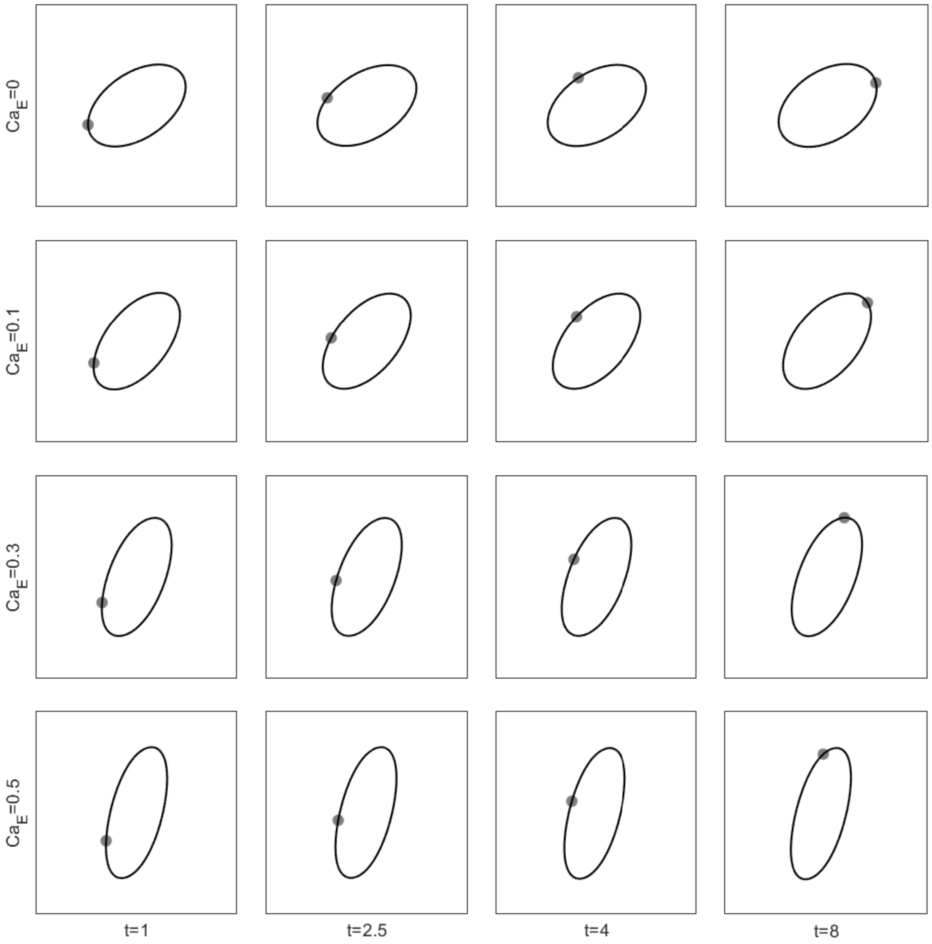

Figure. 48: Tank-treading phenomenon for Case C ($\sigma_r = 4.75$, $\varepsilon_r = 3.5$), $Ca = 0.0125$, under various strength of electric field.

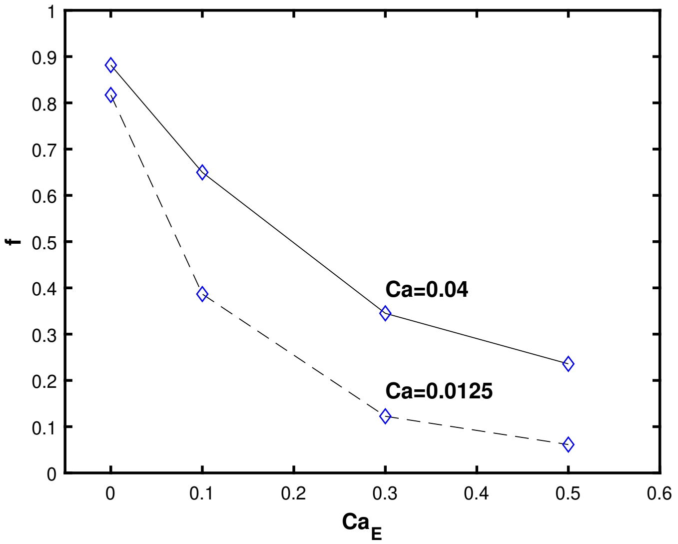

Figure. 49: The normalized tank treading frequency for Case A: $\sigma_r = 1.75$, $\varepsilon_r = 3.5$.

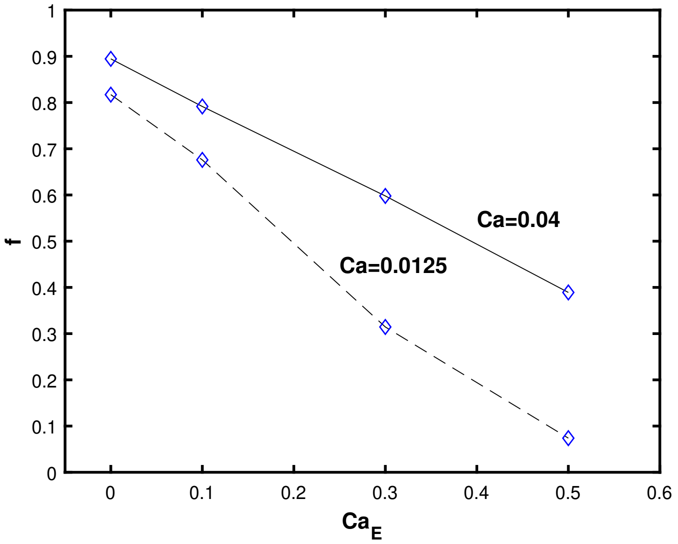

Figure. 50: The normalized tank treading frequency for Case B: $\sigma_r = 3.25$, $\varepsilon_r = 3.5$.

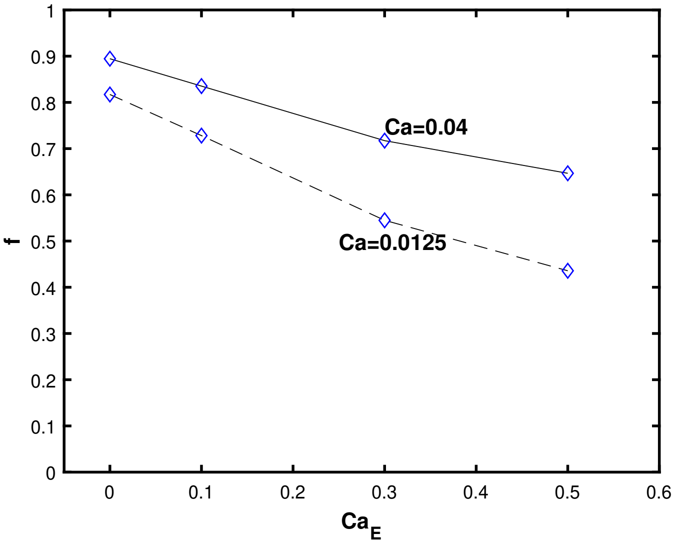

Figure. 51: The normalized tank treading frequency for Case C: $\sigma_r = 4.75$, $\varepsilon_r = 3.5$.

5.2 EFFECT OF MEMBRANE BENDING STIFFNESS

In this section, the effect of membrane bending stiffness are considered. The elastic force causes the development of in-plane tension and bending moments causes transverse shear tensions. Under certain conditions, microcapsules in a shear flow display membrane folding effect, and wrinkles are formed parallel to their orientation [51, 52]. The bending stiffness are found to be important resource in determining the equilibrium configuration and shape oscillations of capsules, and in avoiding the development of wrinkling and folding of capsules in shear flow. Pozrikidis' [41] numerical study shows that bending stiffness has significant effect on the steady configuration of elastic capsules in simple shear flow, a membrane that offers resistance to bending can suppress elastic instabilities.

Although the two-dimensional model is a large simplification, previous publications [53, 54, 55] show that two dimensional study maintains most common features of the three dimensional capsule's motion, such as the transition from tank treading mode to tumbling mode.

In the next two sections, the electric effect on the deformation of both circular and biconcave capsules is studied numerically under simple shear flow.

5.2.1 EFFECT OF MEMBRANE BENDING ON CIRCULAR CAPSULES

Due to the bending stiffness, the transverse shear tension is defined by $q = \frac{\partial m}{\partial \ell} = E_B \frac{\partial}{\partial \ell}(\kappa - \kappa_0)$, in which E_B is the bending stiffness modulus, κ is the current curvature, and κ_0 is the initial shape configured curvature.

An initially unstressed circular capsule was placed in the center of the shear flow domain. In the absence of DC electric field, the capsule was deformed by the flow until the system reached equilibrium. The Taylor deformation parameter D_{xy}, initially zero, increases to a constant during the process. The present results show that the capsule deforms to the steady shape and then the membrane rotates around the liquid inside, which is called tank-treading motion. This simulation was performed for a variety of two dimensionless parameters, capillary number of fluid Ca and bending modulus E_b. As shown in Figure 52a and 53a, a sequence of steady capsules with shear flow $Ca = 0.04$ and $Ca = 0.125$ are presented for various bending modulus E_b ranging from 0 to

0.5, respectively. The results agree well with Sui's method [42]. As expected, the shape deformation are significantly affected by bending stiffness. The bending stiffness restricts the global deformation of capsule and prevents the development of high curvature at the two tips. Seen from Figure 54 and 55, as the bending modulus increases, the deformed capsule get closer to a circle shape which indicates smaller deformation. It can be observed that the time taken to achieve steady shape is shorter under higher bending modulus. This is intuitively making sense because the capsule deform less under higher bending modulus and it is quicker to generate enough elastic force to balance the viscous shear force.

The temporal evolution of the inclination angle are presented in Figure 52b and Figure 53b for $Ca = 0.04$ and $Ca = 0.125$, respectively. The quantitative results confirm that increased bending stiffness reduces the capsule deformation and makes it tend to tilt less along the flow direction.

When the electric field is applied vertically as before, three cases are studied. For the case A, we studied the capsule deformation having different capillary number and different bending modulus when $Ca = 0.04$. From Figure 56, 57 and 59, we can see that when the bending stiffness increases, the deformation decreases with quicker tank-treading motion. With fixed bending stiffness, a comparison was made with electric capillary numbers of $Ca_E = 0$, $Ca_E = 0.1$ and $Ca_E = 0.3$. The results for cases B and C are shown in Figure 61-70, we observe the similar effects for the two cases. As shown in Figure 56-70, all three cases show the tank-treading phenomenon; for higher capillary number, the motion becomes slower.

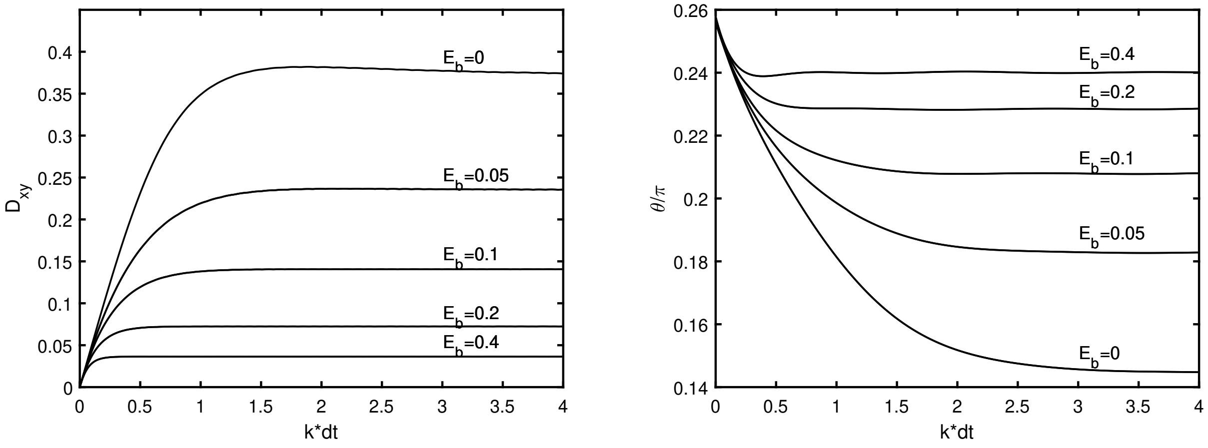

(a) (b)

Figure. 52: The Taylor deformation parameter and inclination angle evolution, $Ca = 0.04$.

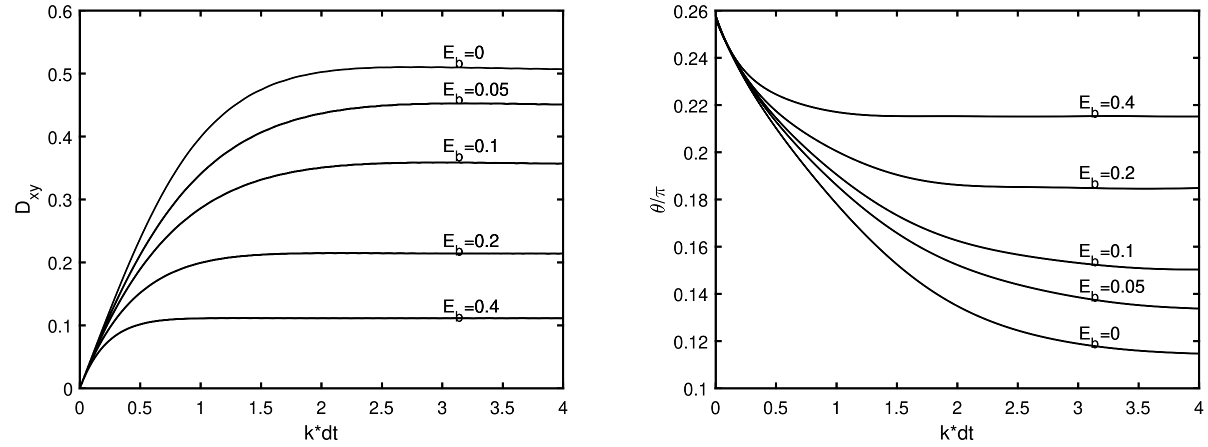

(a) (b)

Figure. 53: The Taylor deformation parameter and inclination angle evolution, $Ca = 0.125$.

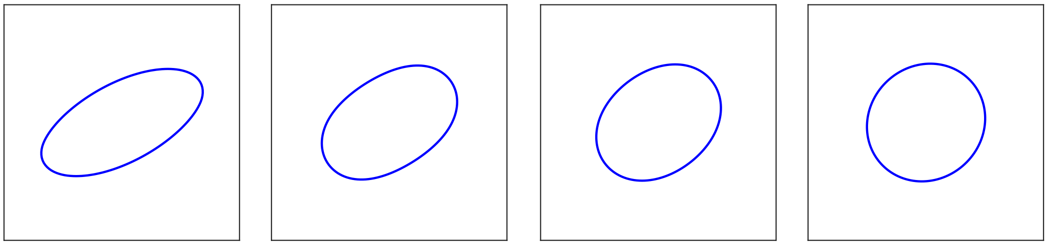

E_b=0 E_b=0.05 E_b=0.1 E_b=0.4

Figure. 54: Equilibrium shape of deformed capsule under various bending modulus under $Ca = 0.04$, $t = 2.5$.

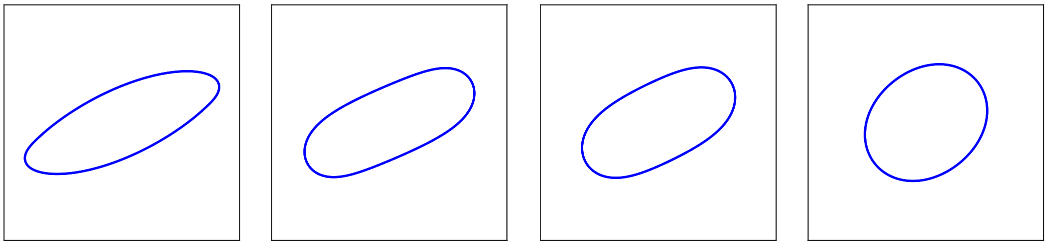

E_b=0 E_b=0.05 E_b=0.1 E_b=0.4

Figure. 55: Equilibrium shape of deformed capsule under various bending modulus under $Ca = 0.125$, $t = 2.5$.

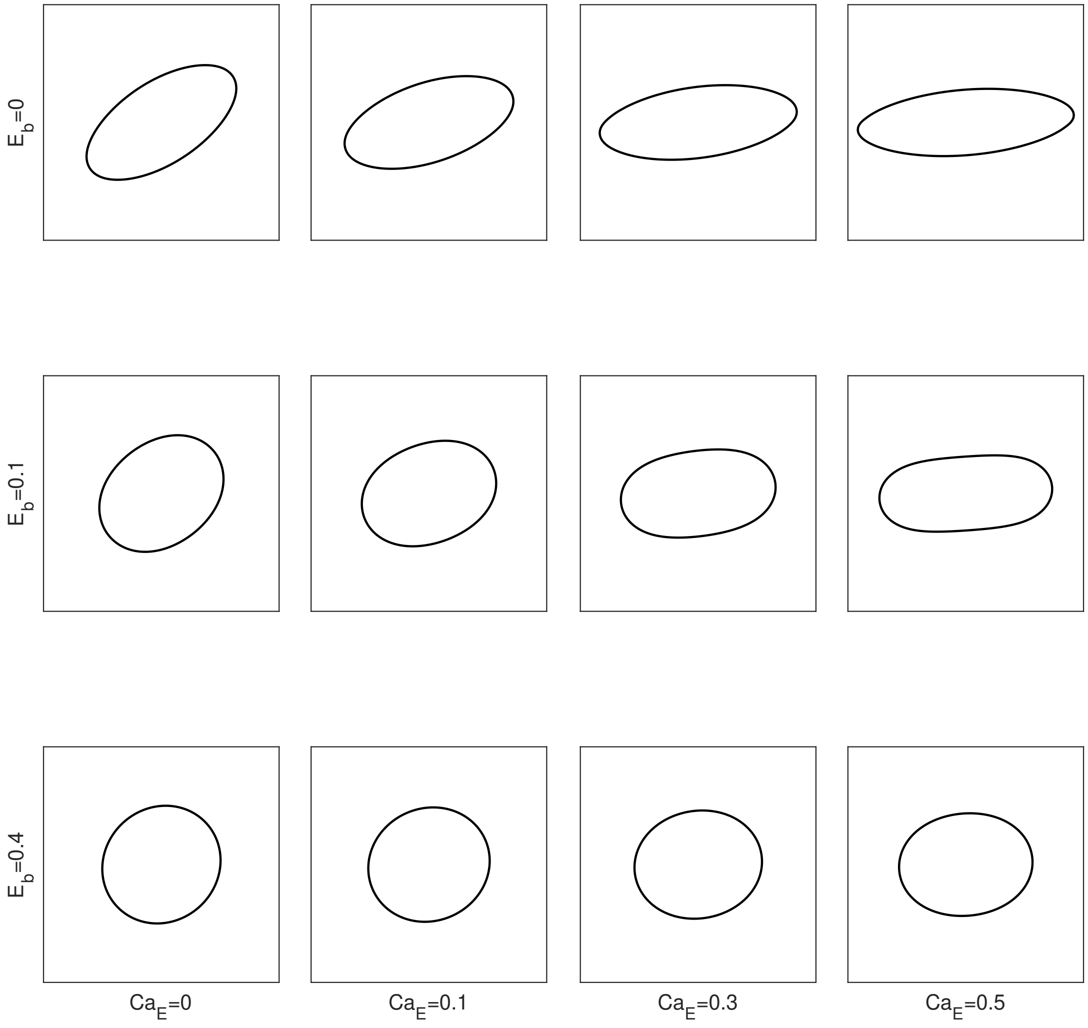

Figure. 56: Equilibrium shapes of circular capsule with $Ca = 0.04$ for case A $(\sigma_r = 1.75, \varepsilon_r = 3.5)$, $t = 1$.

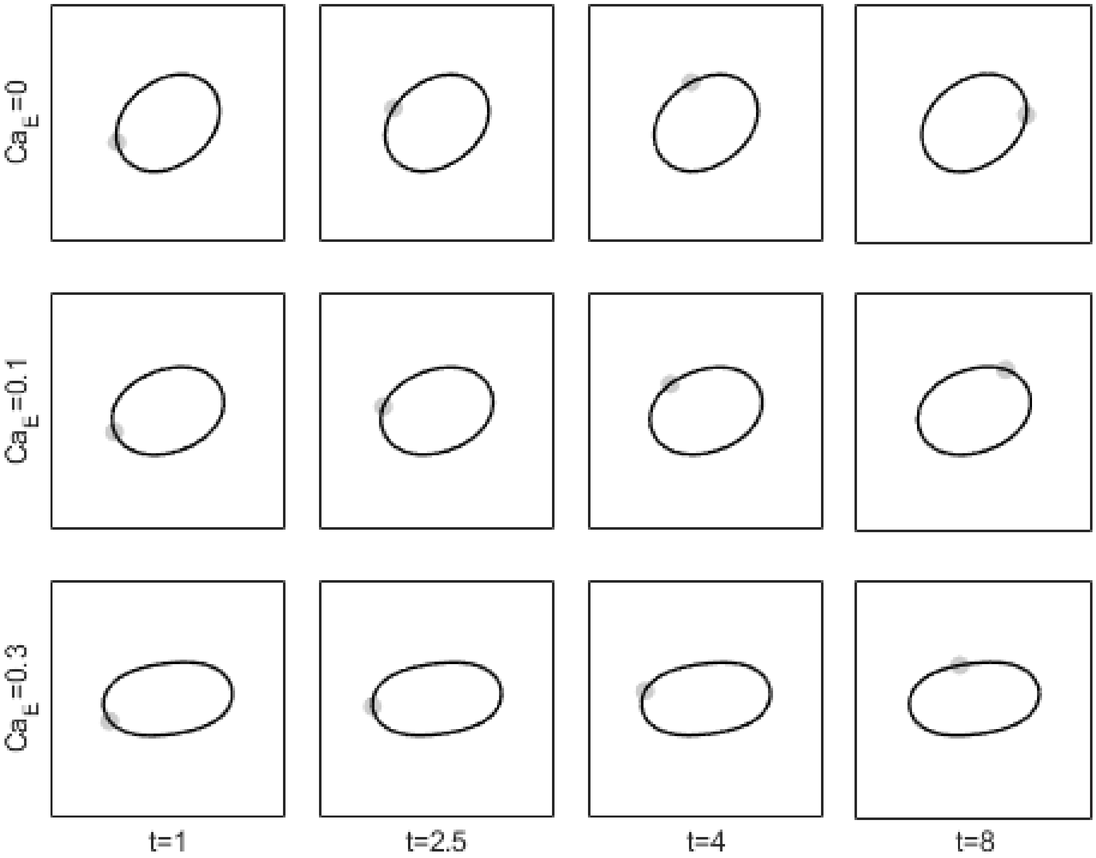

Figure. 57: Tank-treading phenomenon for circular capsule with bending stiffness $E_b = 0.1$ under various electric field for case A ($\sigma_r = 1.75, \varepsilon_r = 3.5$).

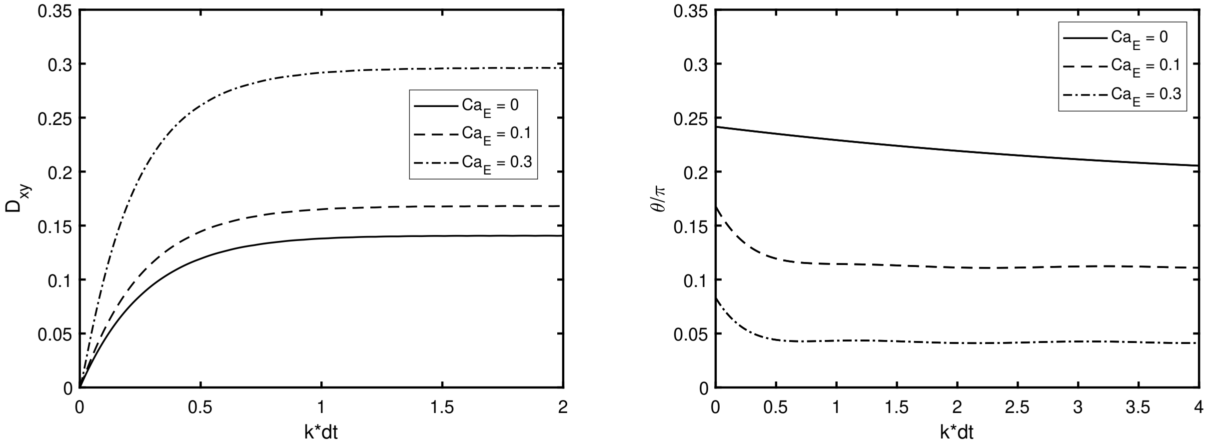

(a) (b)

Figure. 58: (a) Deformation parameter D_{xy}; (b) inclination angle θ/π for Case A, $E_b = 0.1$

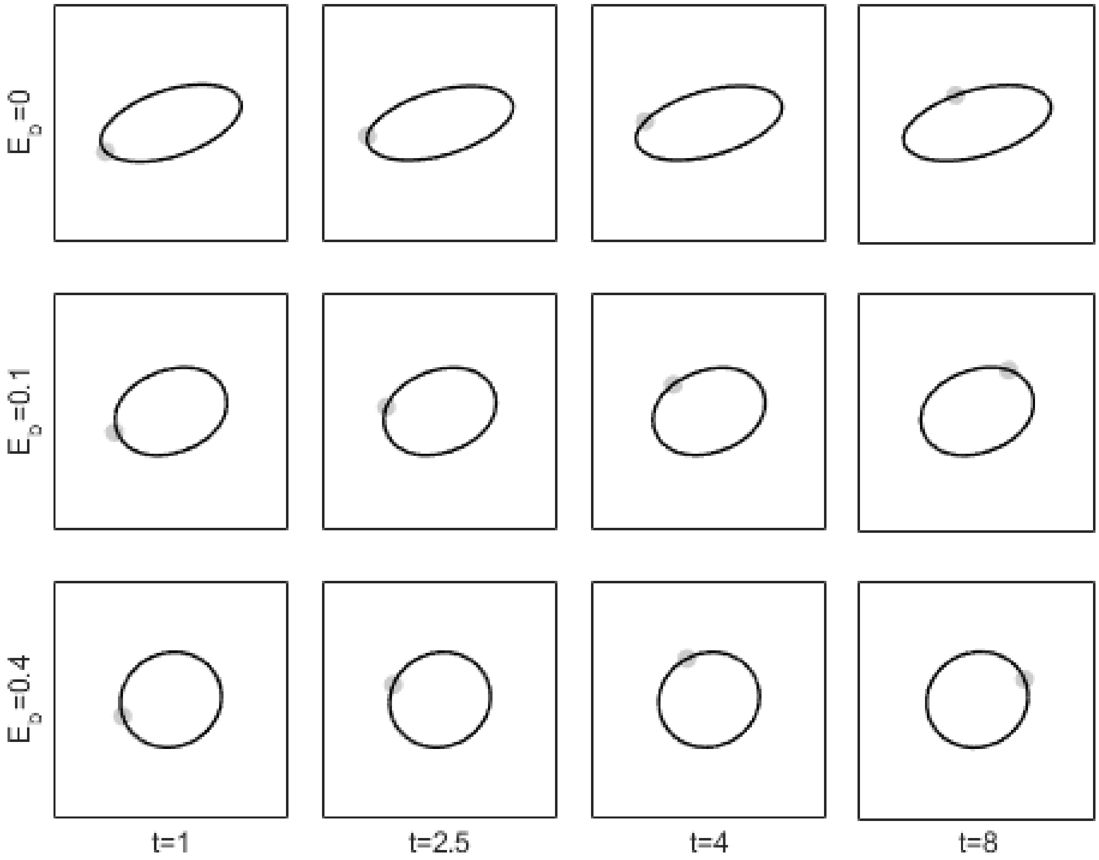

Figure. 59: Tank-treading phenomenon for circular capsule with various bending stiffness under electric field with $Ca_E = 0.1$ for case A $(\sigma_r = 1.75, \varepsilon_r = 3.5)$.

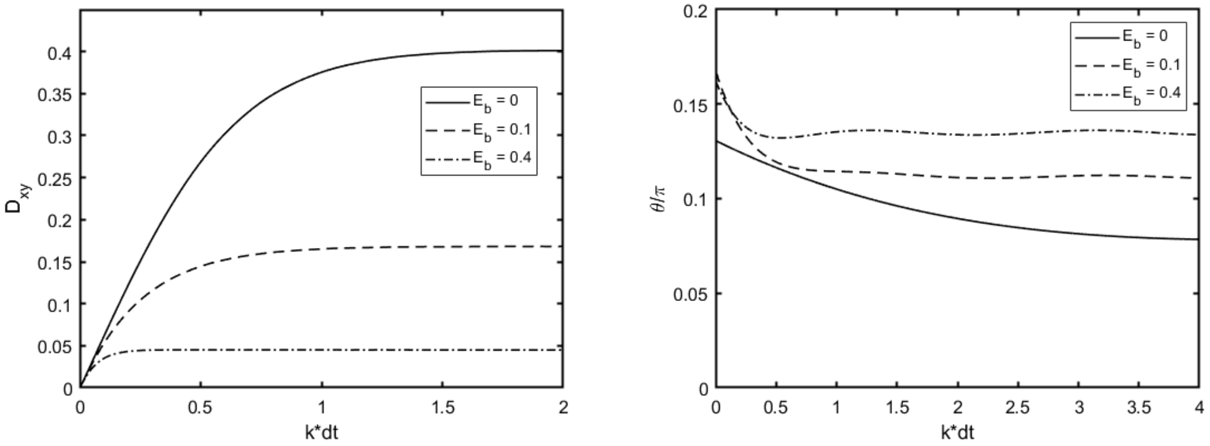

(a) (b)

Figure. 60: (a) Deformation parameter D_{xy}; (b) inclination angle θ/π for Case A, $Ca_E = 0.1$

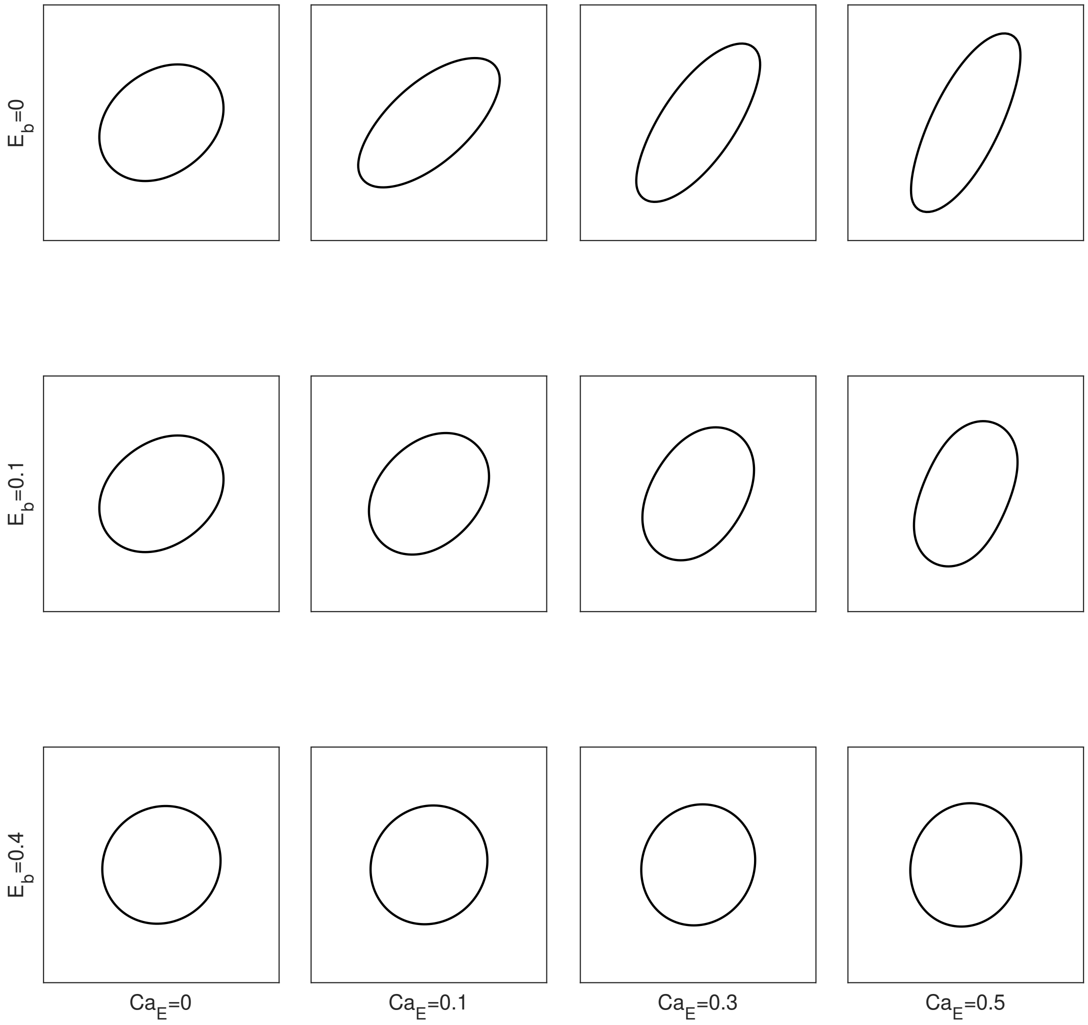

Figure. 61: Equilibrium shapes of circular capsule with $Ca = 0.04$ for case B $(\sigma_r = 3.25, \varepsilon_r = 3.5)$.

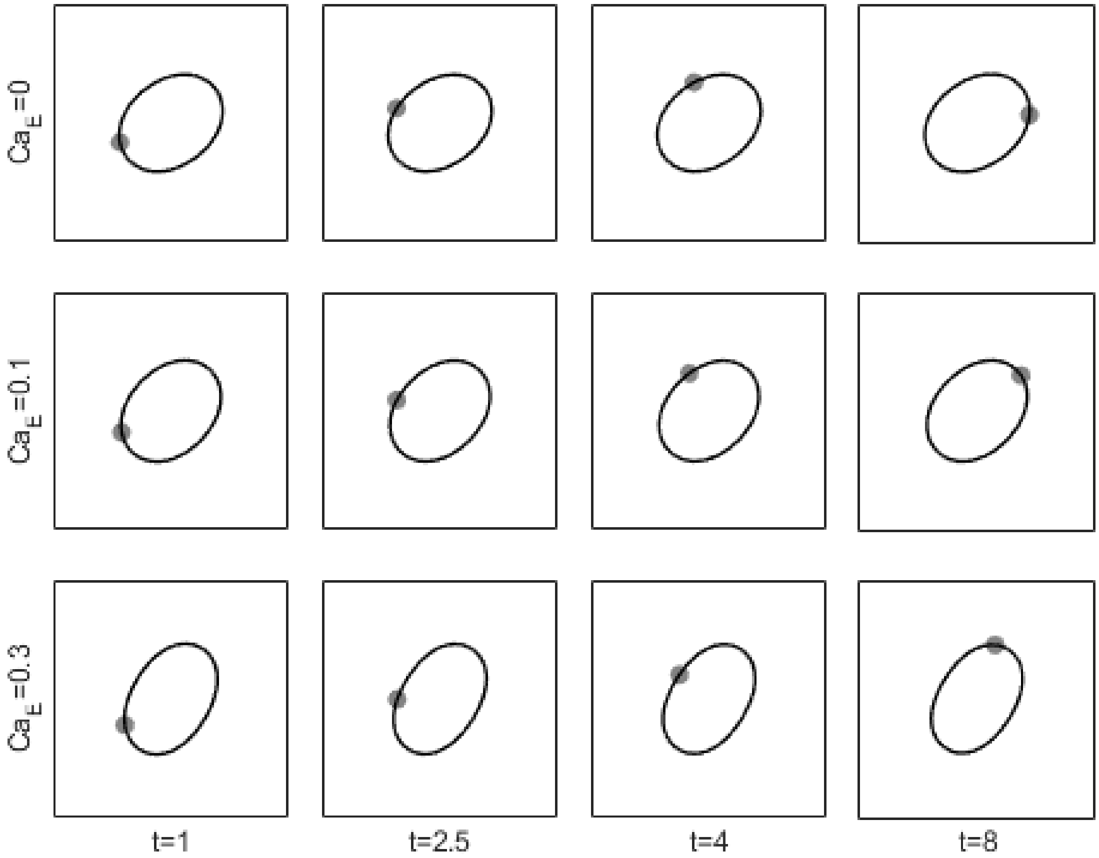

Figure. 62: Tank-treading phenomenon for circular capsule with bending stiffness $E_b = 0.1$ under various electric field for case B $(\sigma_r = 3.25, \varepsilon_r = 3.5)$.

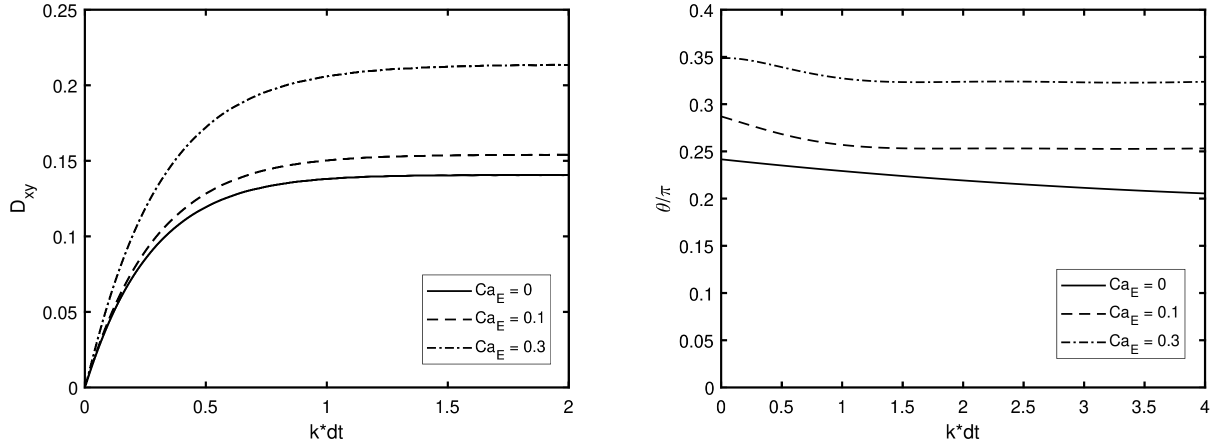

(a) (b)

Figure. 63: (a) Deformation parameter D_{xy}; (b) inclination angle θ/π for Case B, $E_b = 0.1$

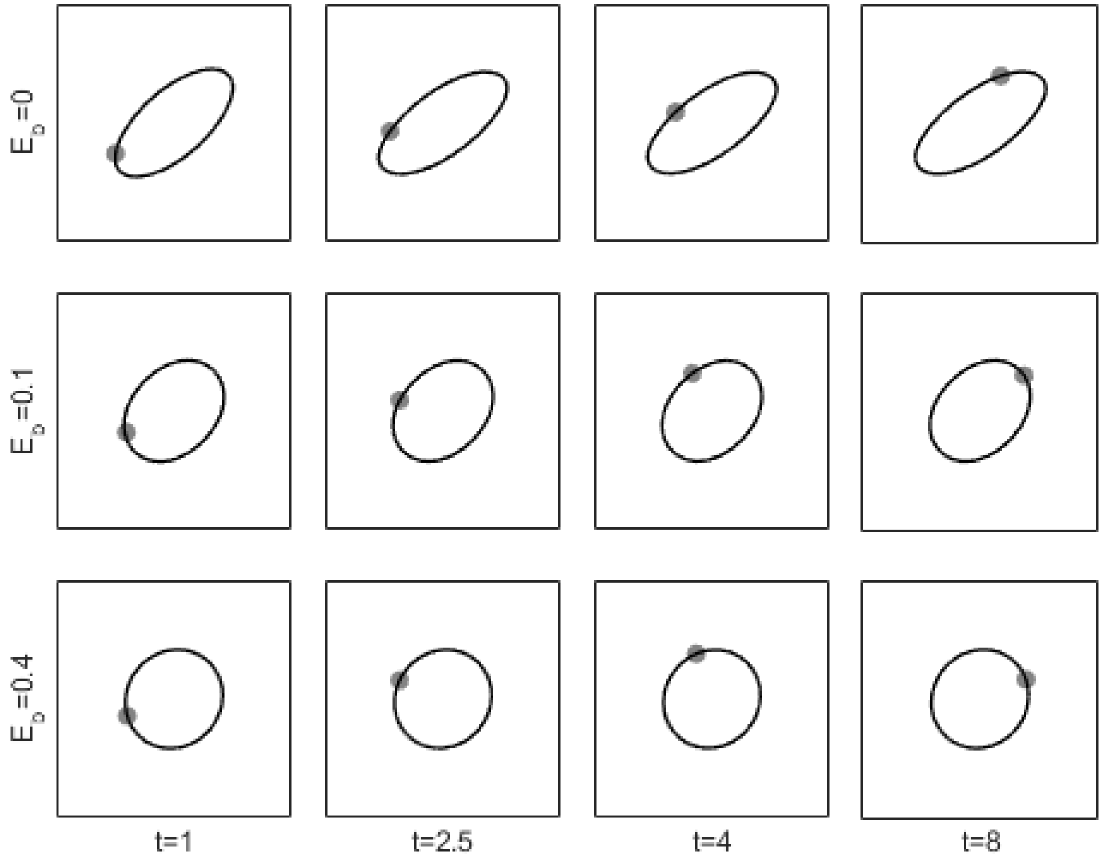

Figure. 64: Tank-treading phenomenon for circular capsule with various bending stiffness under electric field with $Ca_E = 0.1$ for case B $(\sigma_r = 3.25, \varepsilon_r = 3.5)$.

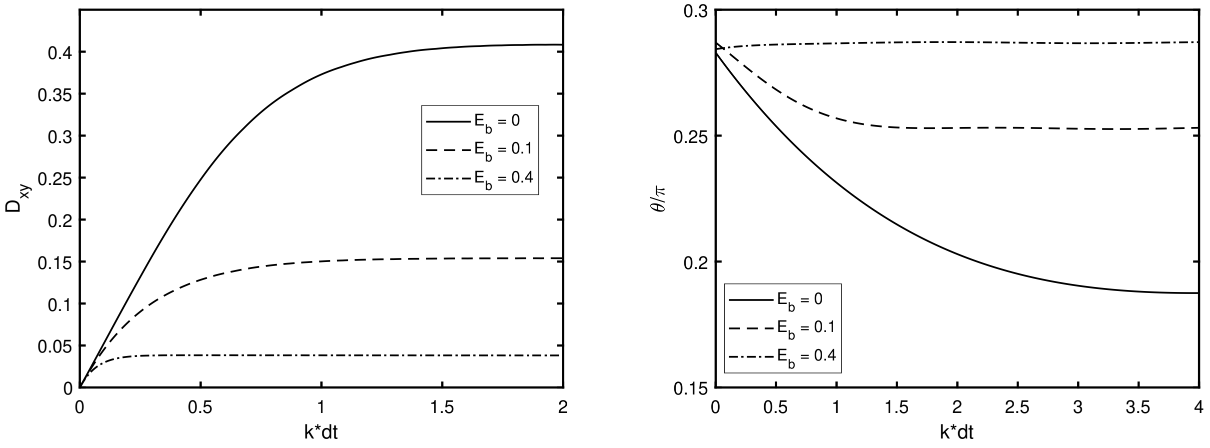

(a) (b)

Figure. 65: (a) Deformation parameter D_{xy}; (b) inclination angle θ/π for Case B, $Ca_E = 0.1$

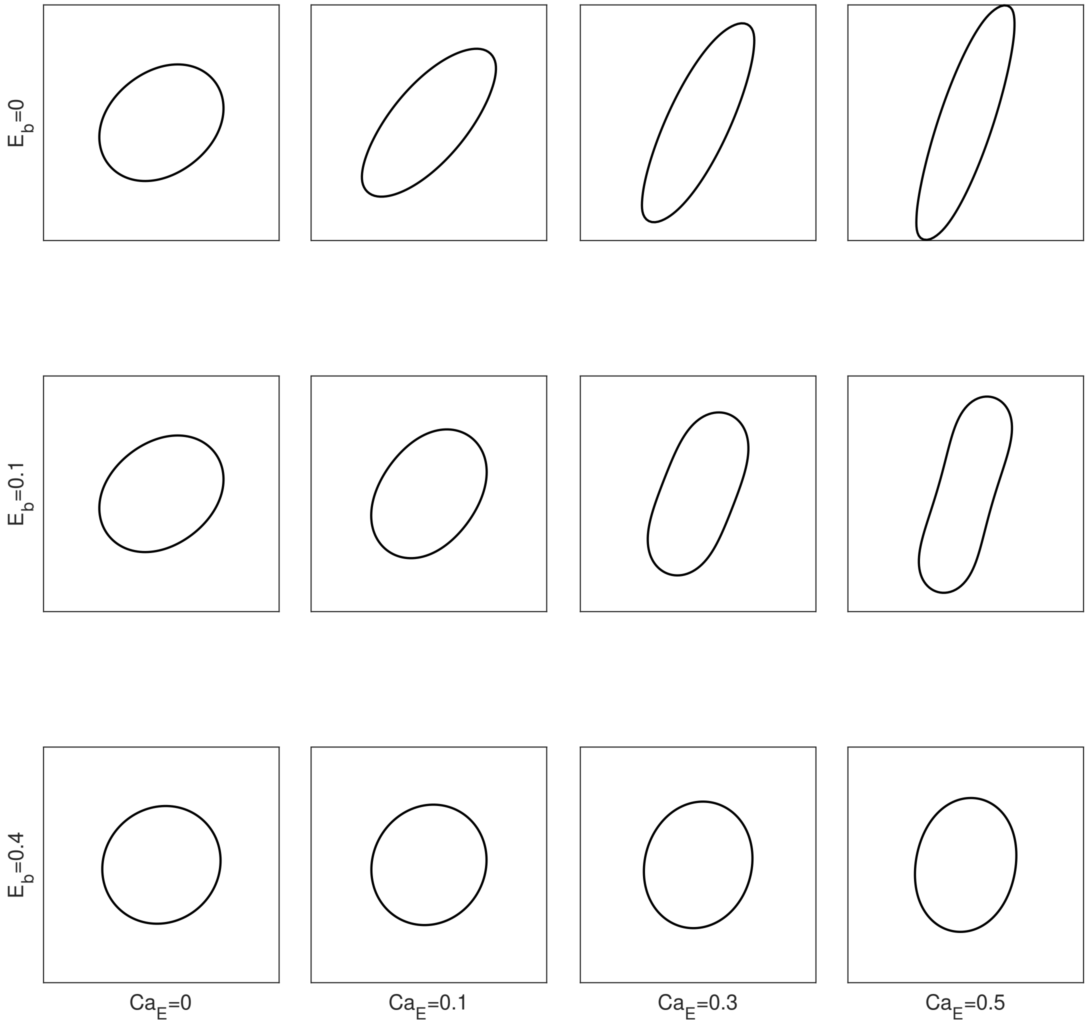

Figure. 66: Equilibrium shapes of circular capsule with $Ca = 0.04$ for case C $(\sigma_r = 4.75, \varepsilon_r = 3.5)$.

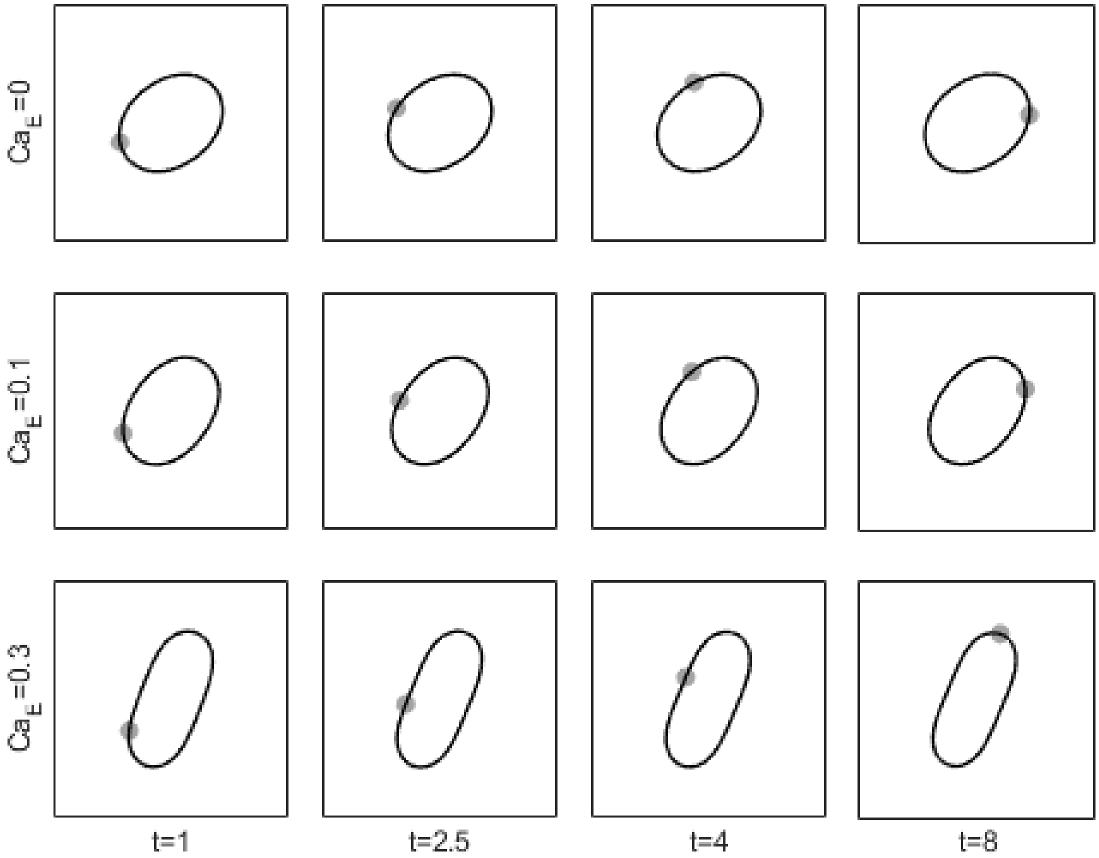

Figure. 67: Tank-treading phenomenon for circular capsule with bending stiffness $E_b = 0.1$ under various electric field for case C $(\sigma_r = 4.75, \varepsilon_r = 3.5)$.

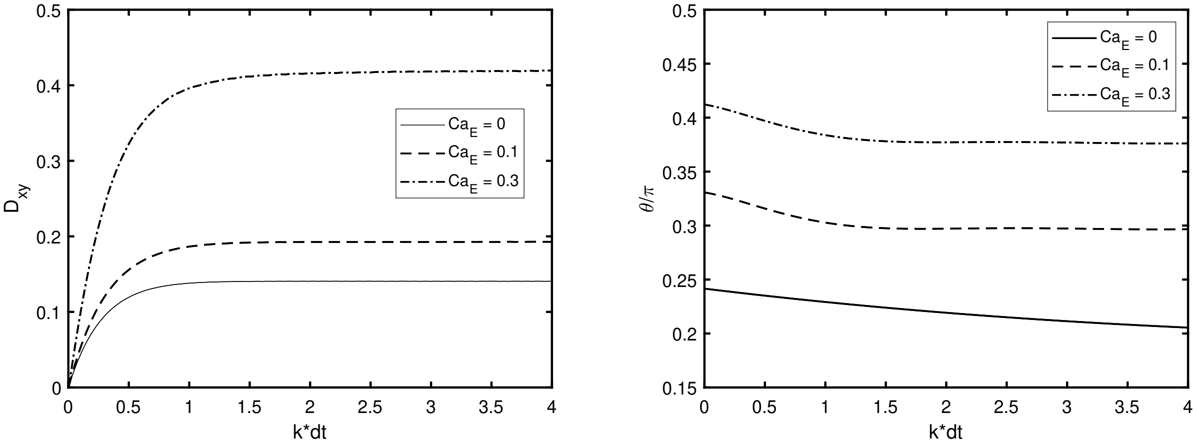

(a)

(b)

Figure. 68: (a) Deformation parameter D_{xy}; (b) inclination angle θ/π for Case C, $E_b = 0.1$

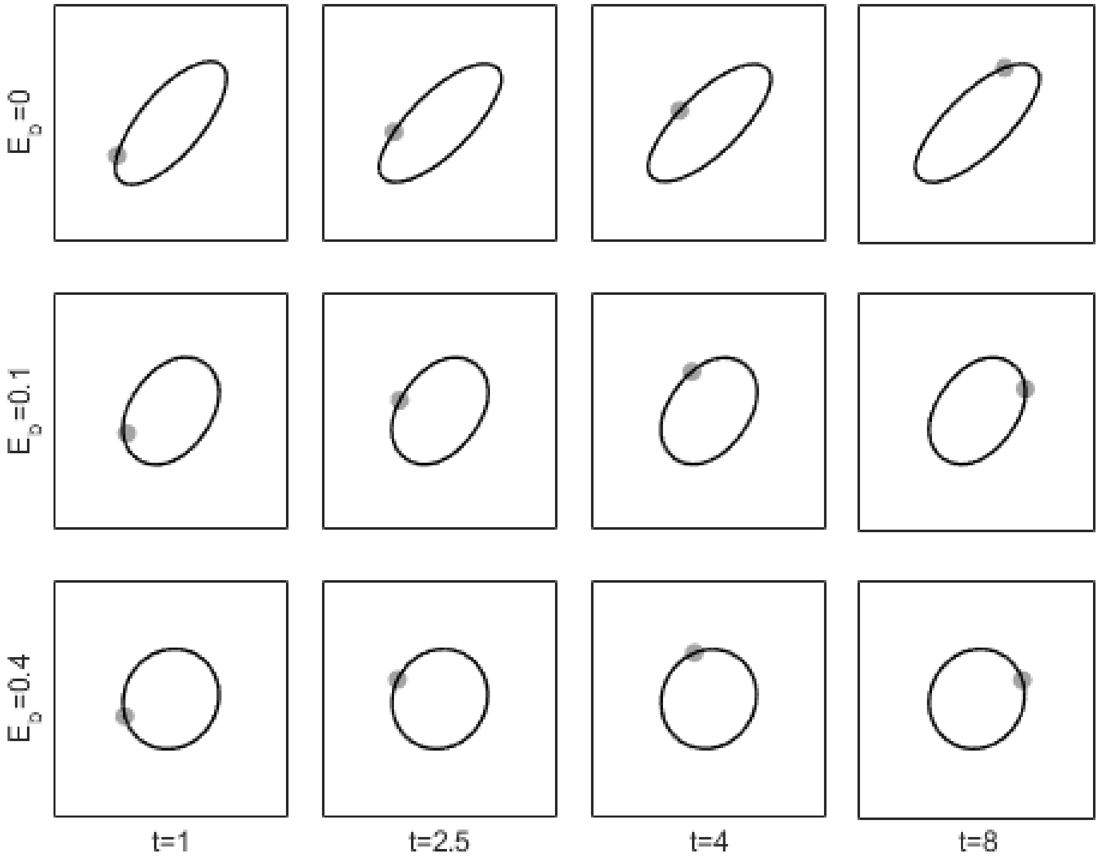

Figure. 69: Tank-treading phenomenon for circular capsule with various bending stiffness under electric field with $Ca_E = 0.1$ for case C $(\sigma_r = 4.75, \varepsilon_r = 3.5)$.

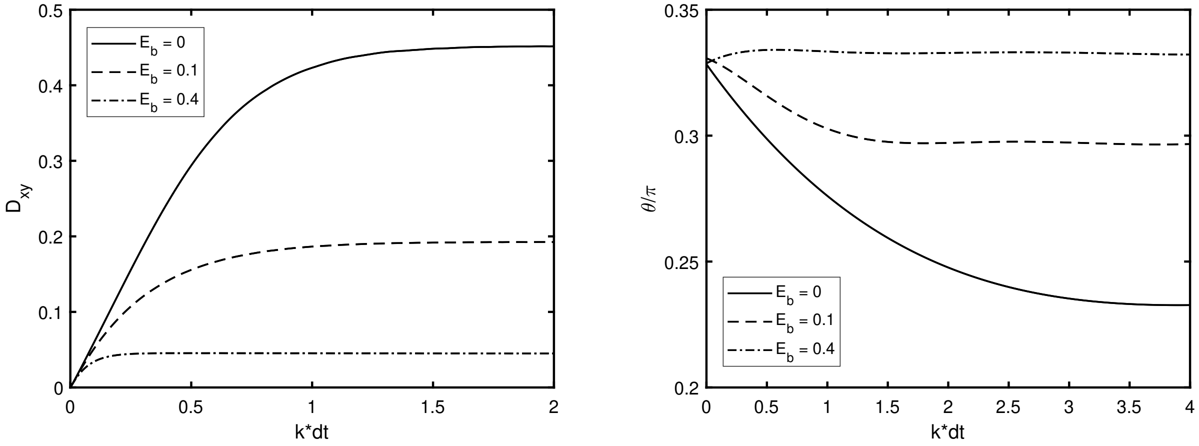

(a)

(b)

Figure. 70: (a) Deformation parameter D_{xy}; (b) inclination angle θ/π for Case C, $Ca_E = 0.1$

5.3 NUMERICAL RESULTS AND DISCUSSION: EFFECT OF ELECTRIC FIELD ON THE DEFORMATION OF BICONCAVE CAPSULES

The deformation of a biconcave capsule under shear flow has been studied extensively in the past by experimental observation, theoretical analysis and numerical simulation. The results show several types of steady-state behavior. Theoretical investigations of biconcave capsule dynamics in [56] exhibit three distinct behaviors, tumbling, tank-treading of the membrane about the viscous interior with periodic oscillations of the orientation angle, and intermittent behavior in which the two modes occur alternately. Researchers have shown that several factors including capsule's bending stiffness, membrane viscosity, fluid viscosity ratio and membrane viscosity all play important roles in determining the capsule's equilibrium behavior.

The biconcave capsule has an initial shape [41] given by

$$\begin{aligned} x &= a\alpha \sin\chi \\ y &= a\frac{\alpha}{2}(0.207 + 2.003\sin^2\chi - 1.123\sin^4\chi)\cos\chi \end{aligned} \tag{152}$$

for equivalent radius $a = 1$, $\alpha = 1.3858$, and angles χ ranges from $-3\pi/4$ to $5\pi/4$. The capsule is initially unstressed. The characteristic length is the equivalent diameter of the biconcave capsule equals $1.48a$.

Without electric field, the deformation of biconcave capsule is studied for various bending modulus under shear flow $Ca = 0.0125$ in Figure 71. The capsule carries out tank treading motion. As bending modulus increased, the motion changes to tumbling mode. The capsule is elongated or compressed depending on the position in shear flow. For higher bending stiffness, the capsule is similar to rigid body motion. It can be confirmed that by increasing the bending stiffness, the capsules' behavior changes from tank-treading to tumbling mode.

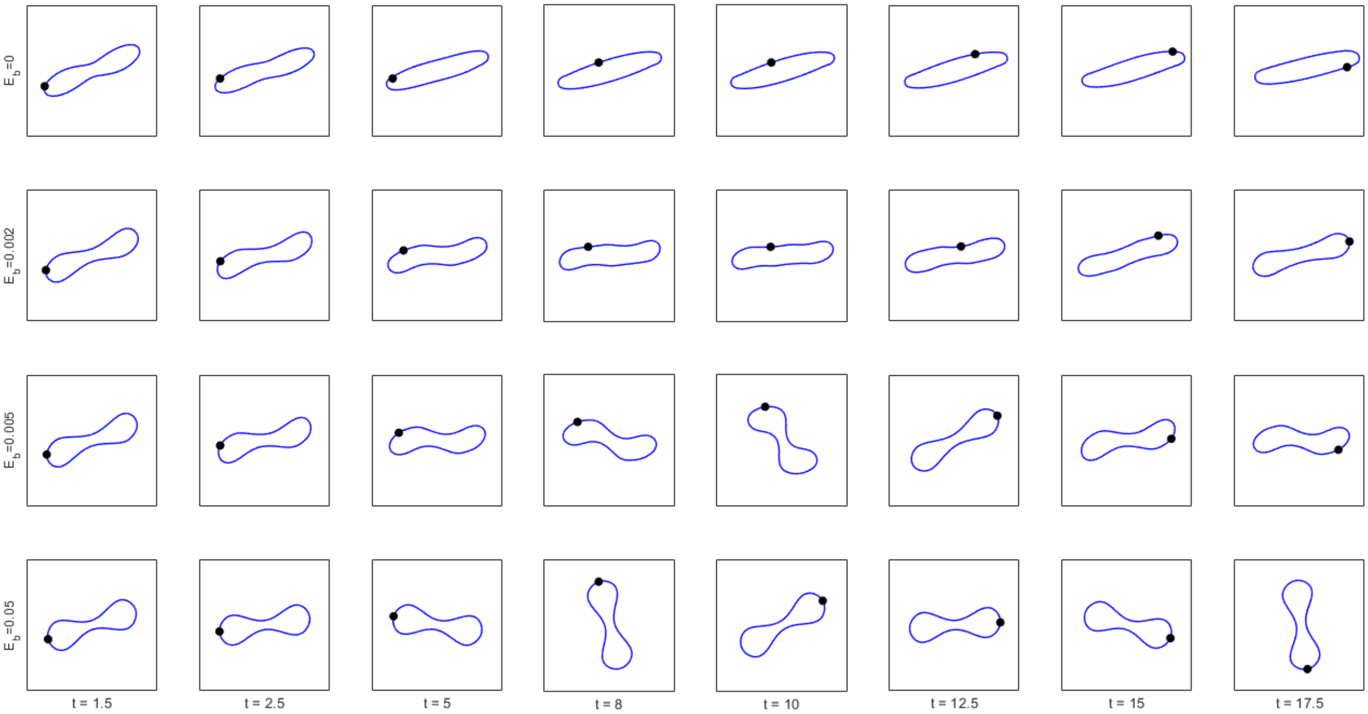

Figure. 71: Deformation of the biconcave capsule with $Ca = 0.0125$ with various bending modulus.

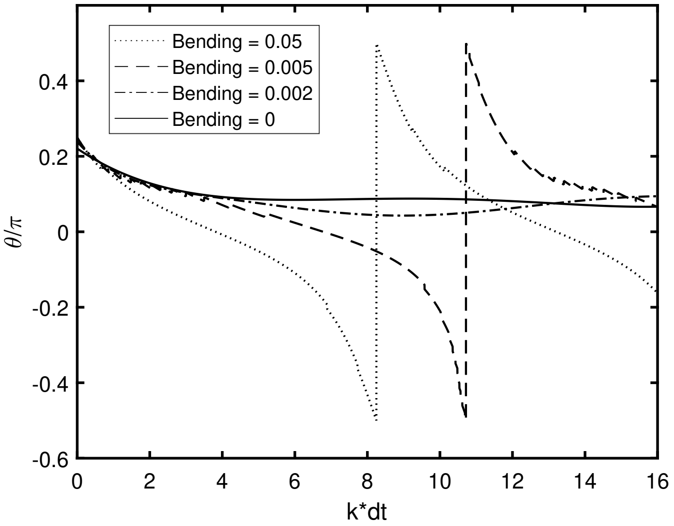

Figure. 72: Inclination angle of the biconcave capsule with $Ca = 0.0125$.

5.3.1 ELECTRIC EFFECT ON THE DEFORMATION OF BICONCAVE CAPSULE UNDER CASE A

The deformation of capsules is investigated for various electric capillary numbers $Ca_E = 0, Ca_E = 0.1, Ca_E = 0.3$ and $Ca_E = 0.5$ under shear flow $Ca = 0.0125$. The bending modulus is $E_b = 0$. Figure 74a presents the evolution of the deformation parameter D_{xy}. The deformed capsules are plotted in Figure 73 until achieved steady state. As the capillary number increases, the response time deformed to steady state decreases. The electric field elongates the capsule in the parallel direction for current combination of permittivity and conductivity ratios. The inclination angle decreases due to the effect of applied electric field.

Figure 75-77 presents the temporal evolution of the biconcave capsule's deformation for various electric capillary numbers with bending modulus $E_b = 0.05$ under shear flow $Ca = 0.0125$. For higher bending modulus, the capsule carries out rigid body like motion, only tumbling mode can be observed during the evolution of motion. The applied electric field does not change the transition between tank treading mode and tumbling mode.

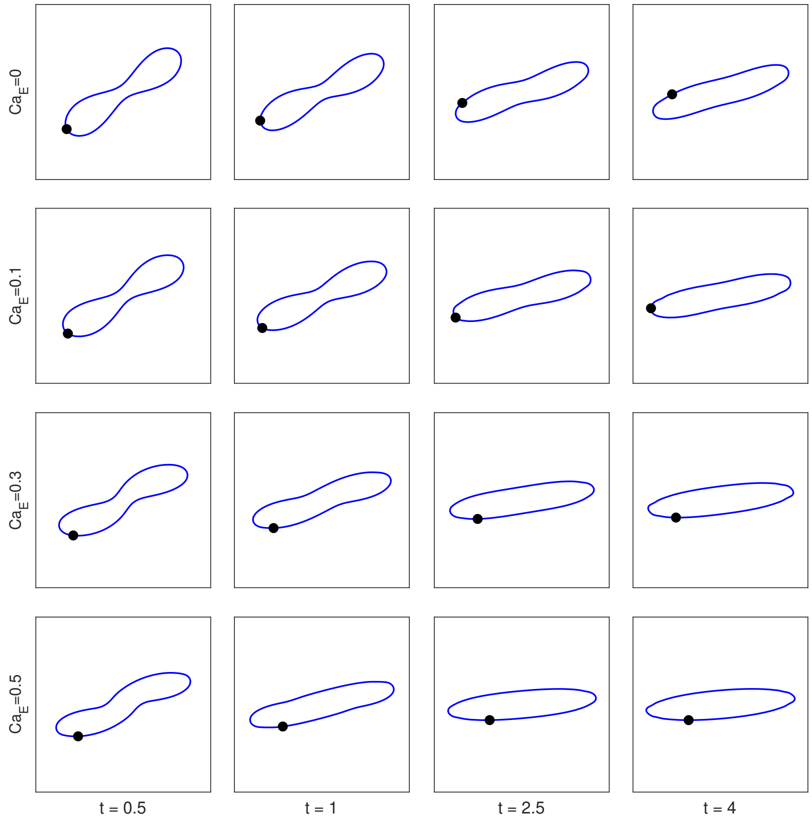

Figure. 73: Deformation of the biconcave capsule with $Ca = 0.0125$ under different strength of electric field for the case A $(\sigma_r = 1.75, \varepsilon_r = 3.5)$.

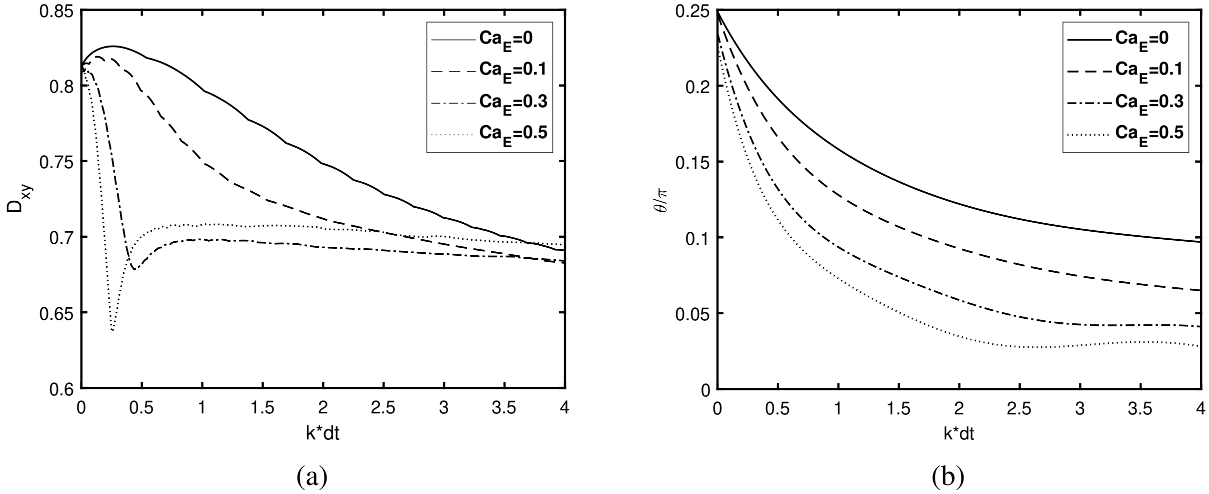

(a)

(b)

Figure. 74: (a) Deformation parameter D_{xy}; (b) inclination angle θ/π for Case A.

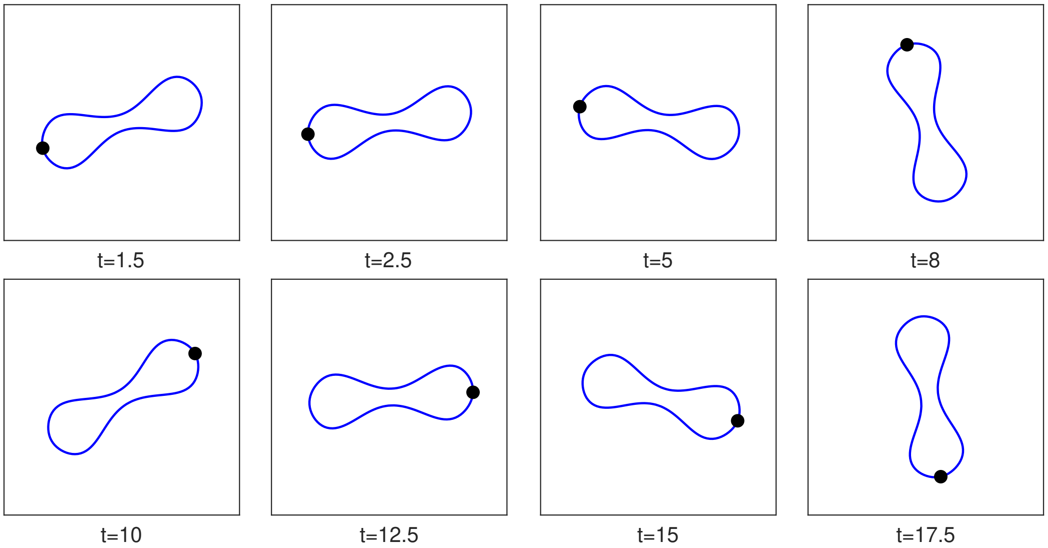

Figure. 75: Tank-treading and tumbling motion of the biconcave capsule with $Ca = 0.0125$ and $E_b = 0.05$.

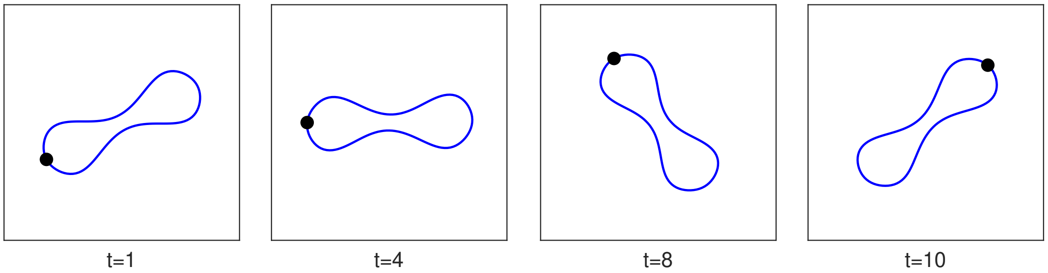

Figure. 76: Tank-treading and tumbling motion of the biconcave capsule with $Ca = 0.0125$ and $E_b = 0.05$ under electric field with $Ca_E = 0.1$ for case A $(\sigma_r = 1.75, \varepsilon_r = 3.5)$.

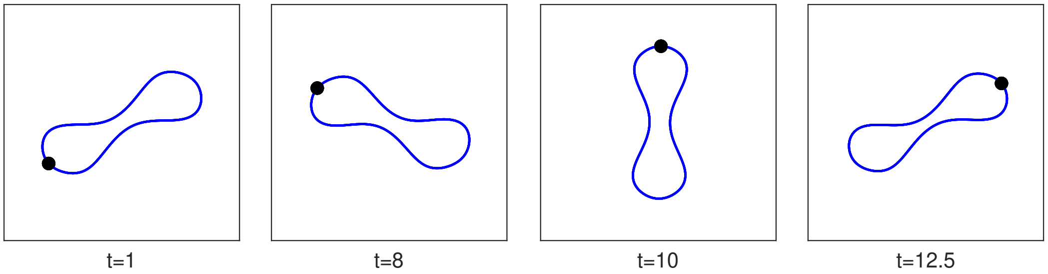

Figure. 77: Tank-treading and tumbling motion of the biconcave capsule with $Ca = 0.0125$ and $E_b = 0.05$ under electric field with $Ca_E = 0.3$ for case A $(\sigma_r = 1.75, \varepsilon_r = 3.5)$.

5.3.2 ELECTRIC EFFECT ON THE DEFORMATION OF BICONCAVE CAPSULE UNDER CASE B AND CASE C

As demonstrated in previous section for capsule under DC electric field, the circular capsule will deform to oblate shape in both Case B ($\sigma_r = 3.25, \varepsilon_r = 3.5$) and Case C ($\sigma_r = 4.75, \varepsilon_r = 3.5$), but induced circulatory flow inside the first quadrant is clockwise for Case B and counterclockwise for Case C.

The deformation of capsules is investigated for various electric capillary numbers $Ca_E = 0, Ca_E = 0.1, Ca_E = 0.3$ and $Ca_E = 0.5$ under shear flow $Ca = 0.0125$. The bending modulus is $E_b = 0$. The deformed capsules are plotted in Figure 78 and 79 for Case B and Case C until achieved steady state, respectively. As the capillary number increases, the response time deformed to steady state decreases. The electric field elongates the capsule in the parallel direction for current combination of permittivity and conductivity ratios. The inclination angle increases due to the effect of applied electric field.

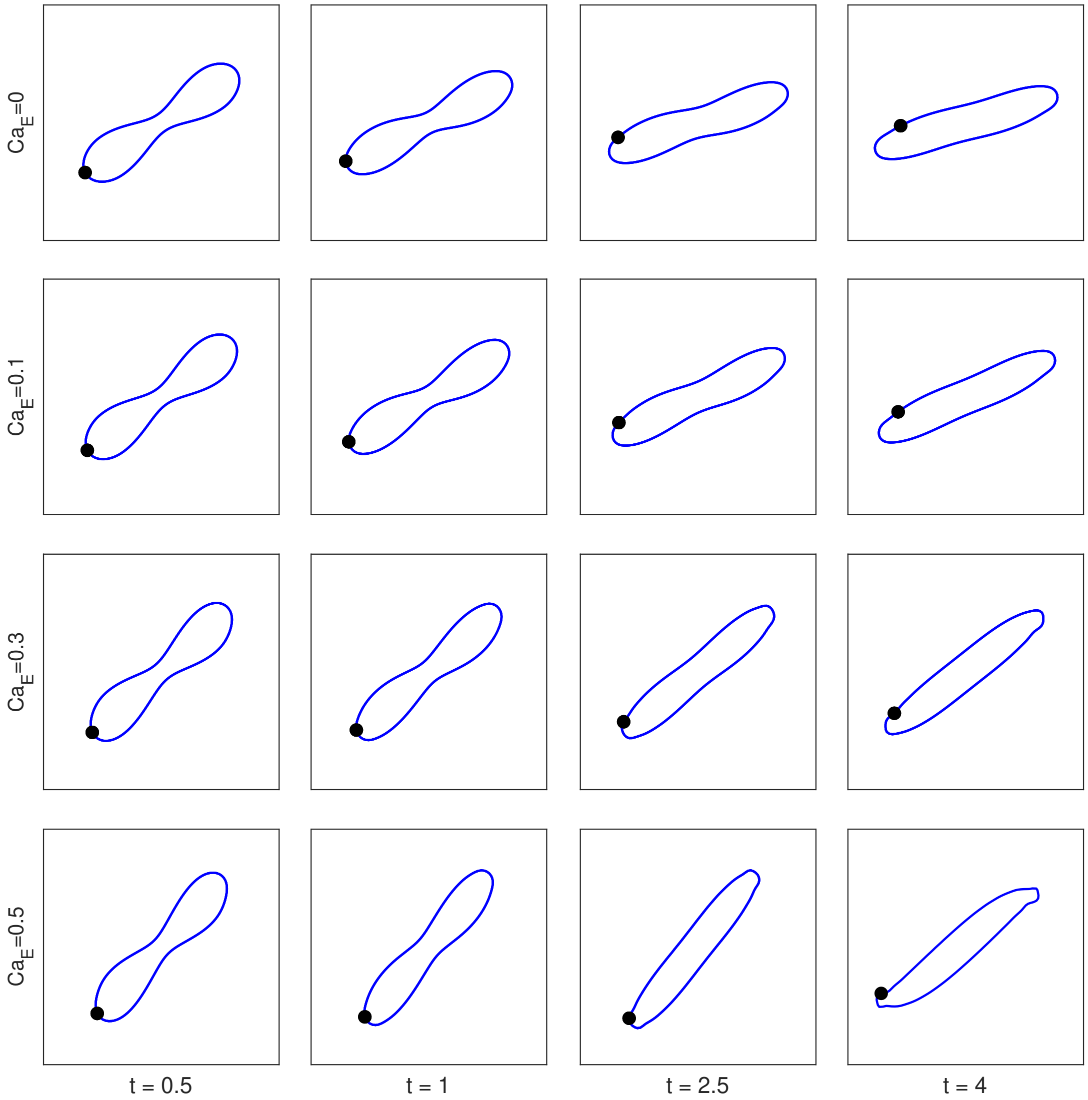

Figure. 78: Deformation of the biconcave capsule with $Ca = 0.0125$ under different strength of electric field for the case B $(\sigma_r = 3.25, \varepsilon_r = 3.5)$.

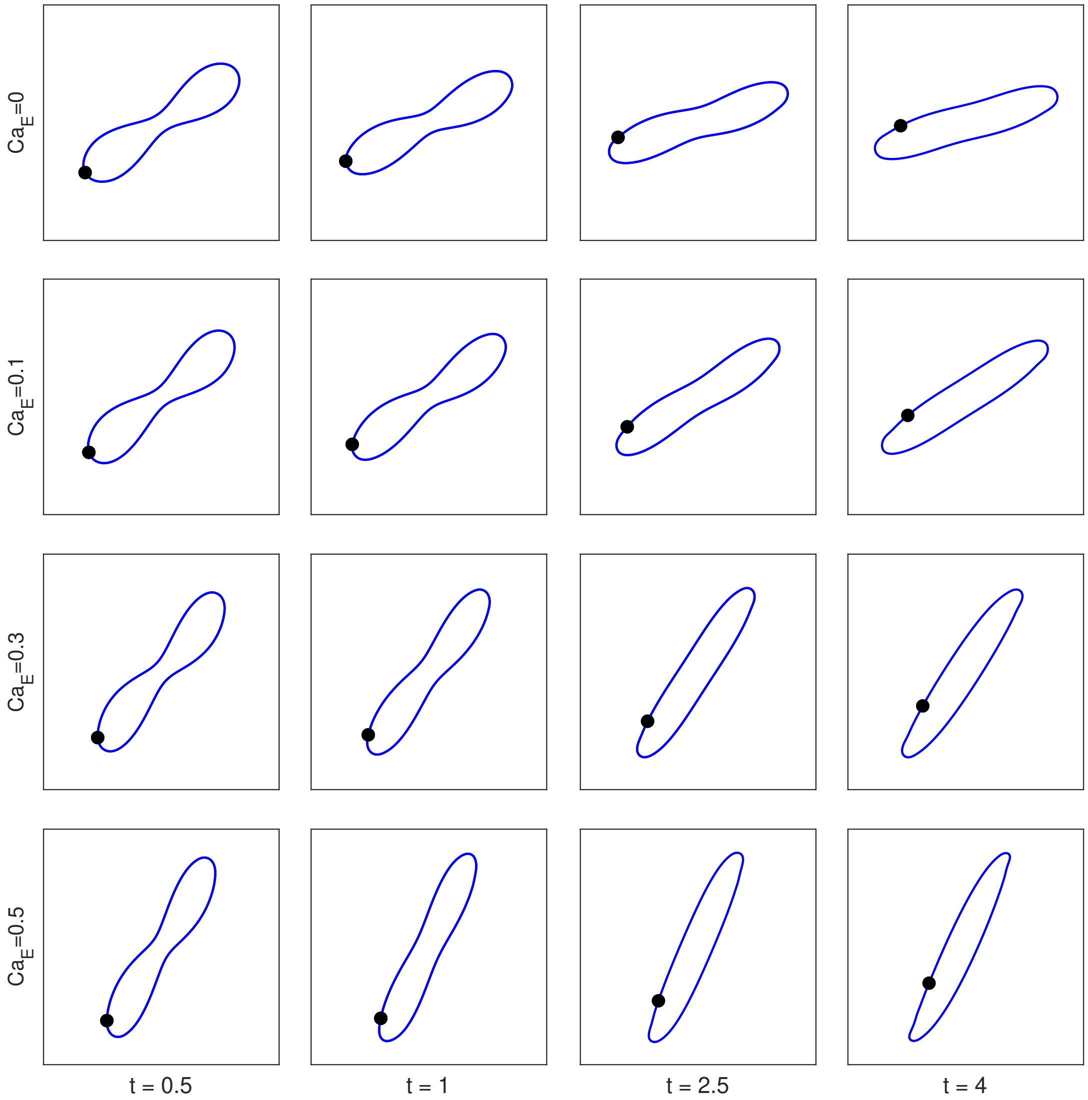

Figure. 79: Deformation of the biconcave capsule with $Ca = 0.0125$ under different strength of electric field for the case C ($\sigma_r = 4.75, \varepsilon_r = 3.5$).

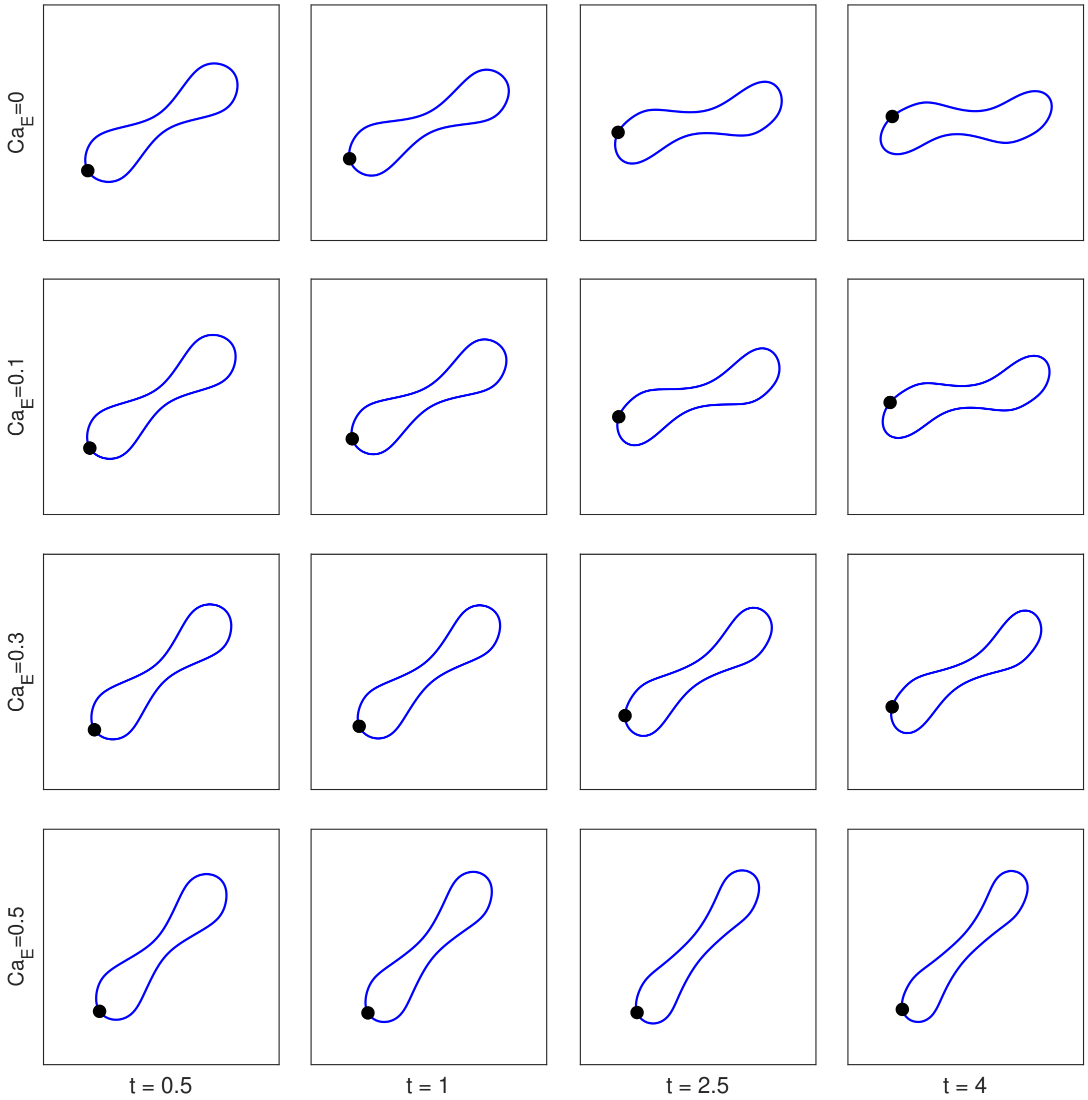

Figure. 80: Deformation of the biconcave capsule with $Ca = 0.0125$ under different strength of electric field with bending modulus $E_b = 0.005$ for the case B $(\sigma_r = 3.25, \varepsilon_r = 3.5)$.

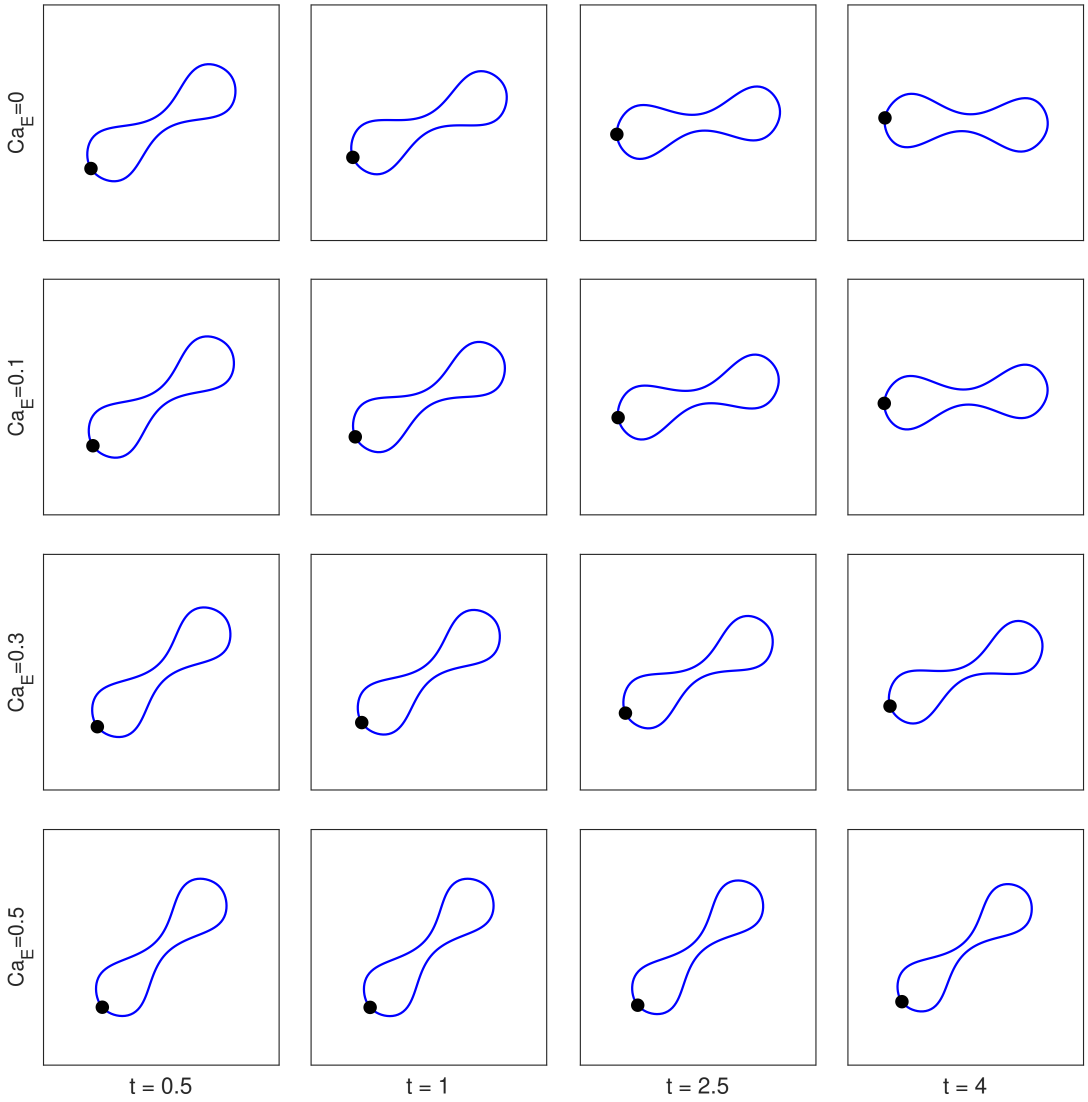

Figure. 81: Deformation of the biconcave capsule with $Ca = 0.0125$ under different strength of electric field with bending modulus $E_b = 0.05$ for the case B $(\sigma_r = 3.25, \varepsilon_r = 3.5)$.

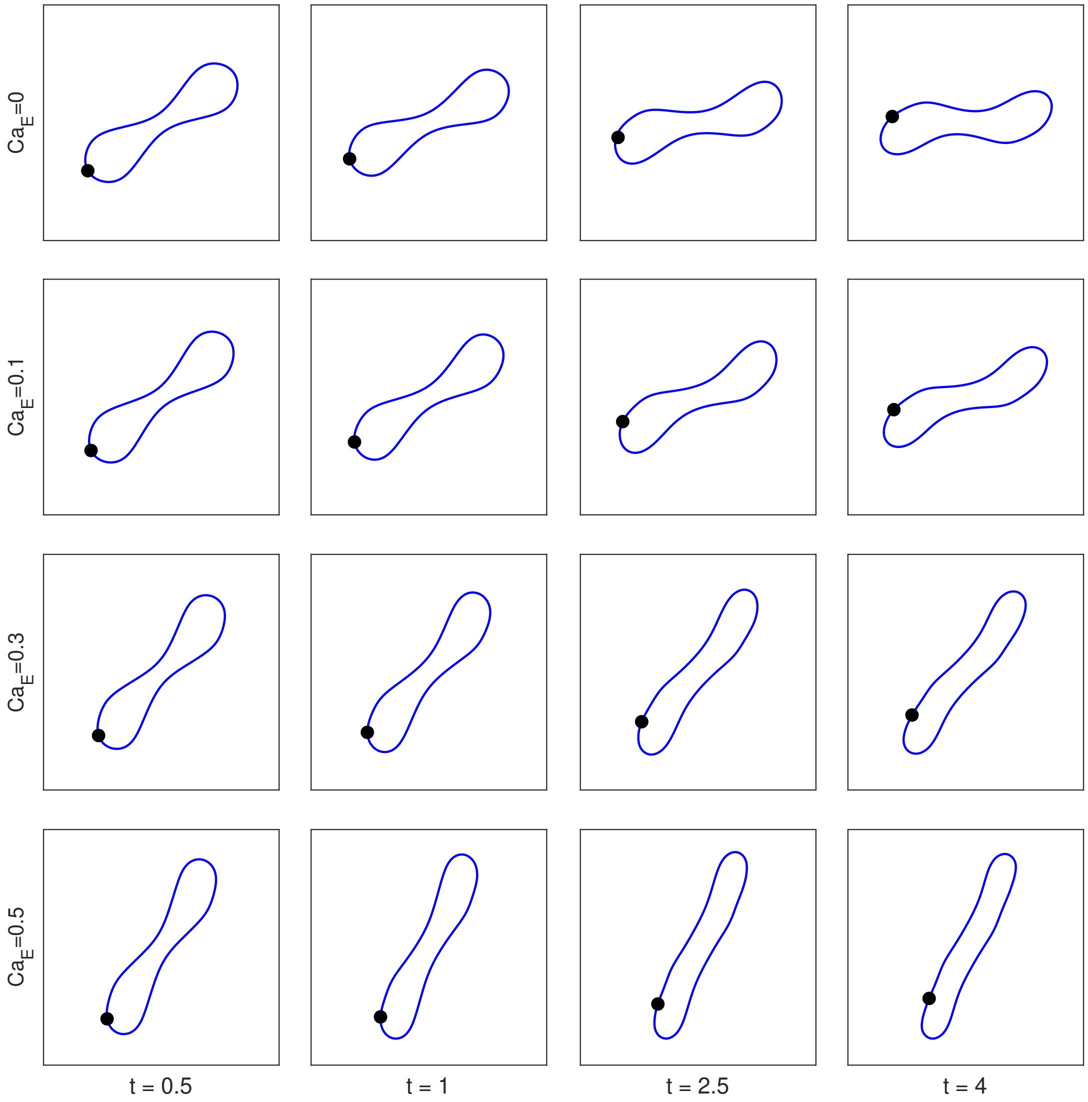

Figure. 82: Deformation of the biconcave capsule with $Ca = 0.0125$ under different strength of electric field with bending modulus $E_b = 0.005$ for the case C ($\sigma_r = 4.75, \varepsilon_r = 3.5$).

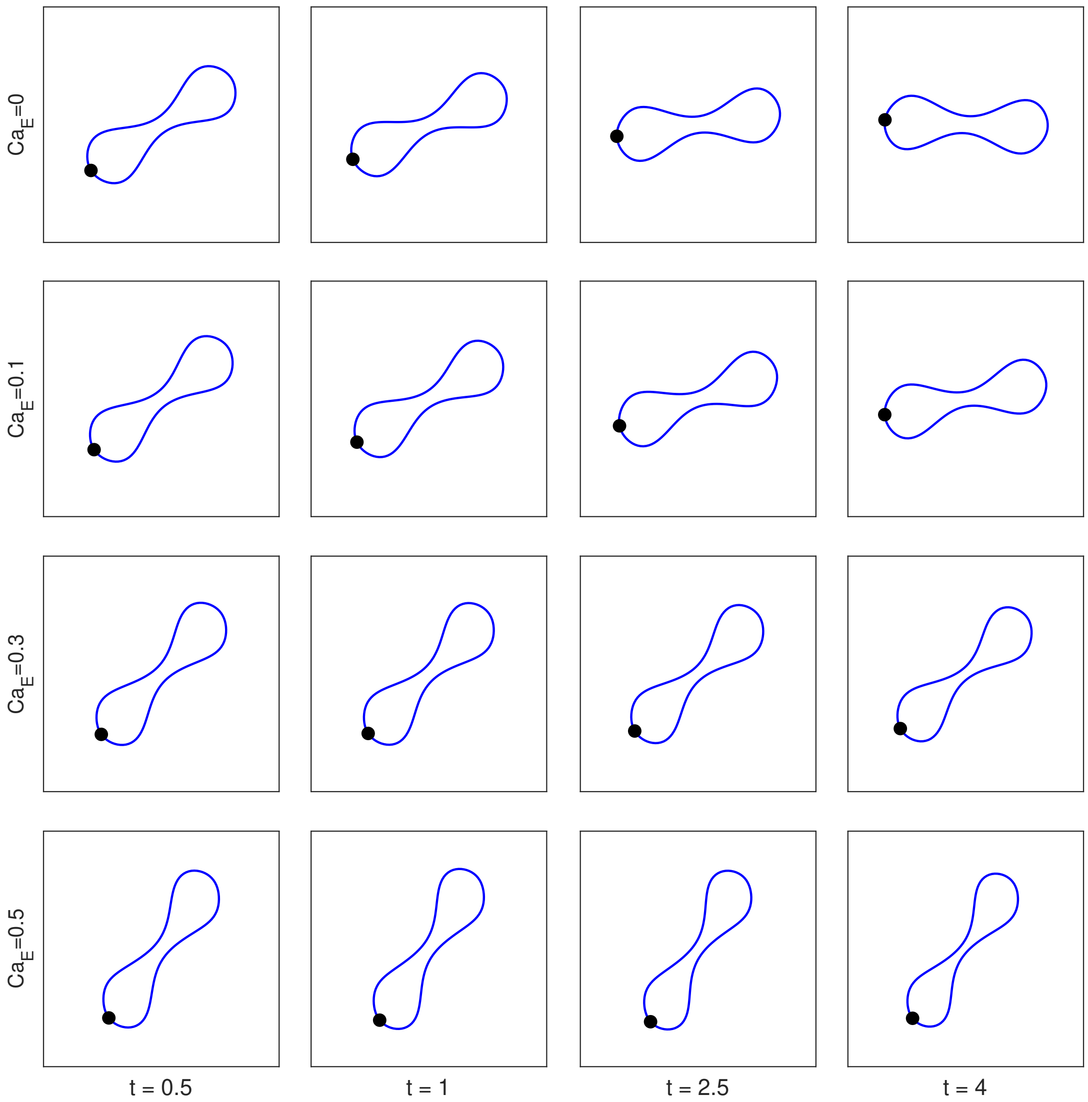

Figure. 83: Deformation of the biconcave capsule with $Ca = 0.0125$ under different strength of electric field with bending modulus $E_b = 0.05$ for the case C $(\sigma_r = 4.75, \varepsilon_r = 3.5)$.

5.3.3 DAMPED TUMBLING MOTION UNDER ELECTRIC EFFECT

The electric field could slow or damp tumbling motion on a biconcave red blood cell in shear flow [57, 58]. Even under a weak electric field which produce slightly effect on deformation of immersed capsule, we can still observe significant change on tumbling motion. The electric forces on the capsule against the viscous forces and align it either vertically or horizontally, depending on the combination of conductivity ratio σ_r and permittivity ratio ε_r.

In the absence of electric field, the deformation of biconcave capsules which subject to the shear flow $Ca = 0.0125$ is studied. Figure 84 presents the temporal evolution of inclination angle for capsules with various bending stiffness $E_b = 0.002$, $E_b = 0.005$ and $E_b = 0.05$. The unsteady tank treading motion is observed for $E_b = 0.002$. The capsule start tank-treading to tumbling transition when increasing bending stiffness from $E_b = 0.002$ to $E_b = 0.005$. Stronger bending stiffness ($E_b = 0.05$) significantly increase tumbling frequency.

When the capsule is subject to both shear flow and electric field, we first investigate the case A $(\sigma_r = 1.75, \varepsilon_r = 3.5)$, for which the electric force align the capsule horizontally. The inclination angles are plotted in Figure 85 and Figure 86, for different bending modulus $E_b = 0.05$ and $E_b = 0.005$, respectively. For larger bending stiffness (Fig. 85), the tumbling period is seen to lengthen with increased strength of electric field; the damped tumbling motion does not occur under current setting of parameters. When bending modulus reduced to $E_b = 0.005$, as seen from Figure 86, the tumbling motion still occur for $Ca_E = 0.1$, but completely damped out for $Ca_E = 0.3$ and $Ca_E = 0.5$. For Case B, the electric force align the capsule vertically, which against the shear flow in opposition. The slow down tumbling motion are presented in Figure 87 and Figure 88.

In general, the strength of the electric field has significant effect on the capsule's motion behavior in shear flow. A weaker electric field only cause slightly decreased tumbling motion while stronger electric field decrease the tumbling frequency substantially and even completely damp the tumbling behavior out.

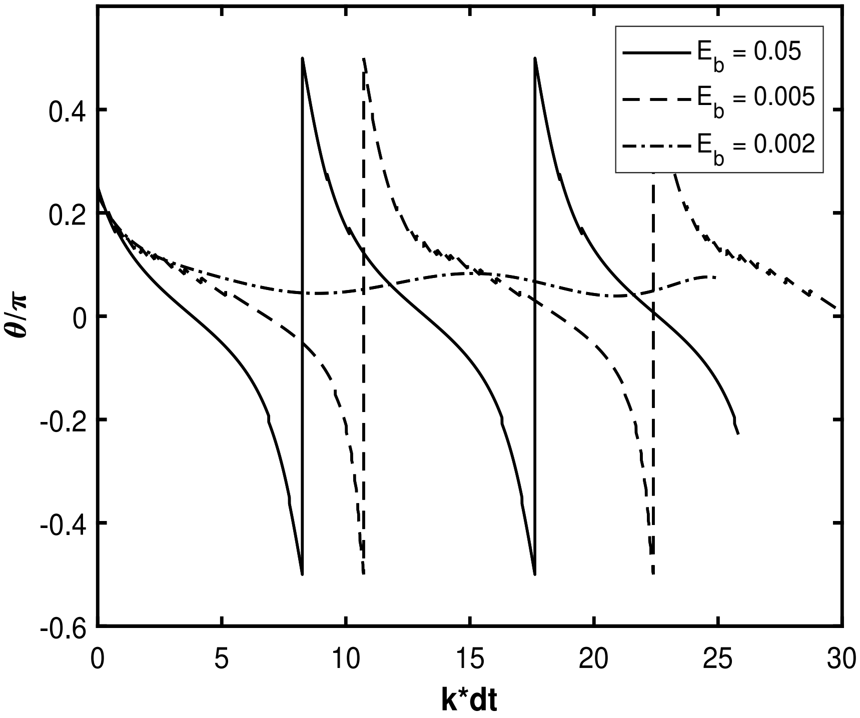

Figure. 84: Evolution of inclination angle of biconcave capsules with various bending modulus at $Ca = 0.0125$.

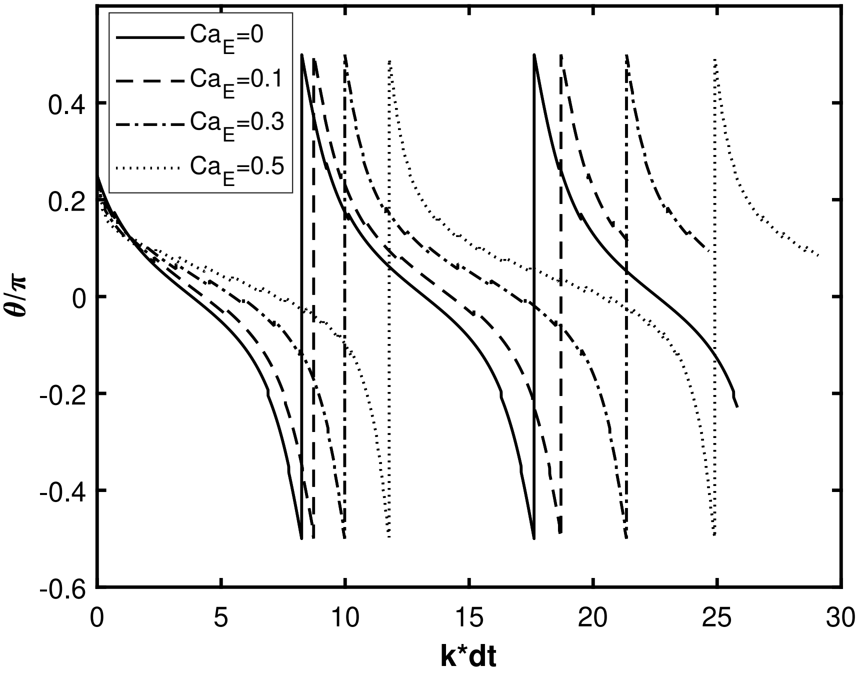

Figure. 85: Evolution of inclination angle of biconcave capsules with bending modulus $E_b = 0.05$ at $Ca = 0.0125$ for Case A ($\sigma_r = 1.75, \varepsilon_r = 3.5$).

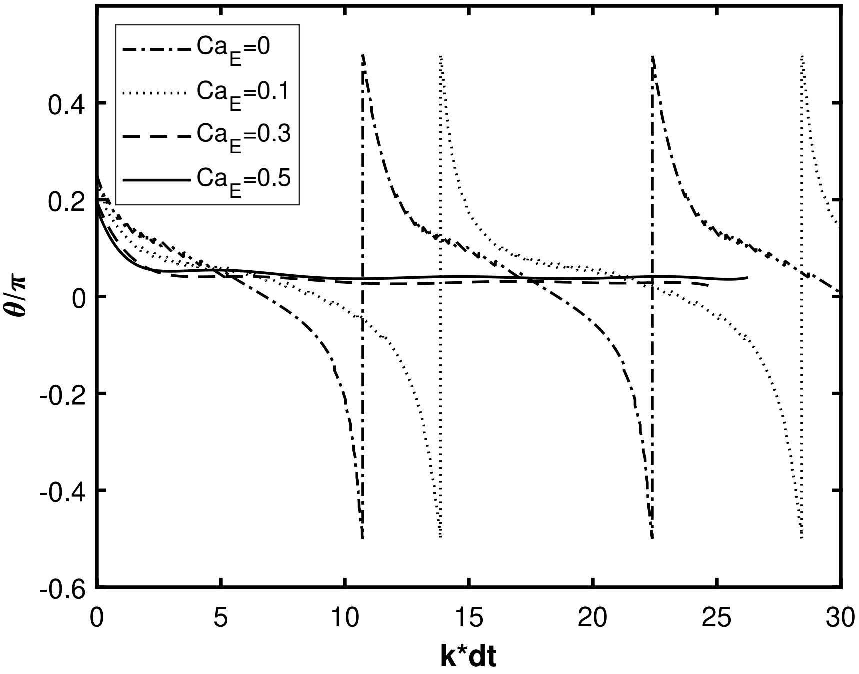

Figure. 86: Evolution of inclination angle of biconcave capsules with bending modulus $E_b = 0.005$ at $Ca = 0.0125$ for Case A ($\sigma_r = 1.75, \varepsilon_r = 3.5$).

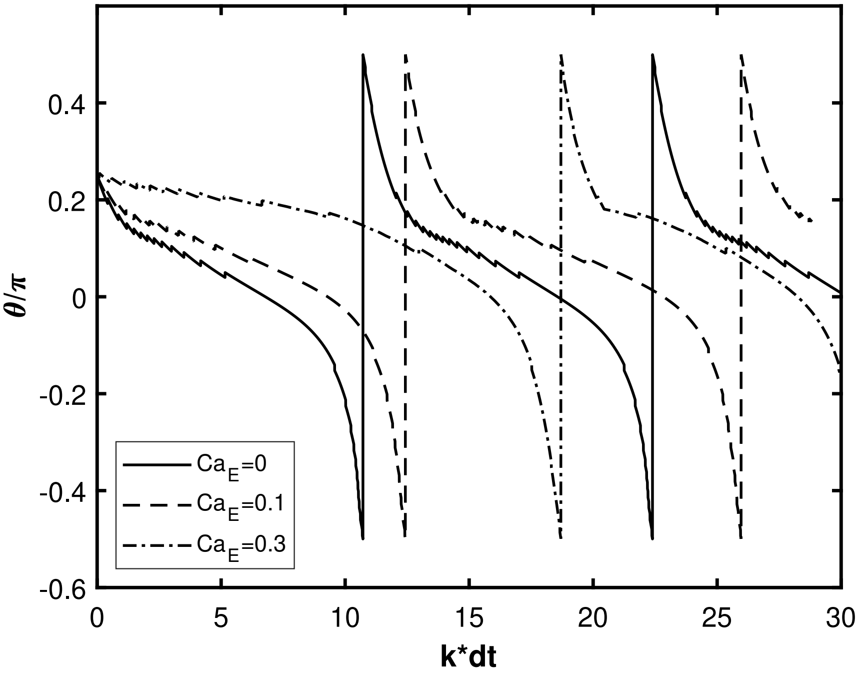

Figure. 87: Evolution of inclination angle of biconcave capsules with bending modulus $E_b = 0.05$ at $Ca = 0.0125$ for Case B ($\sigma_r = 3.25, \varepsilon_r = 3.5$).

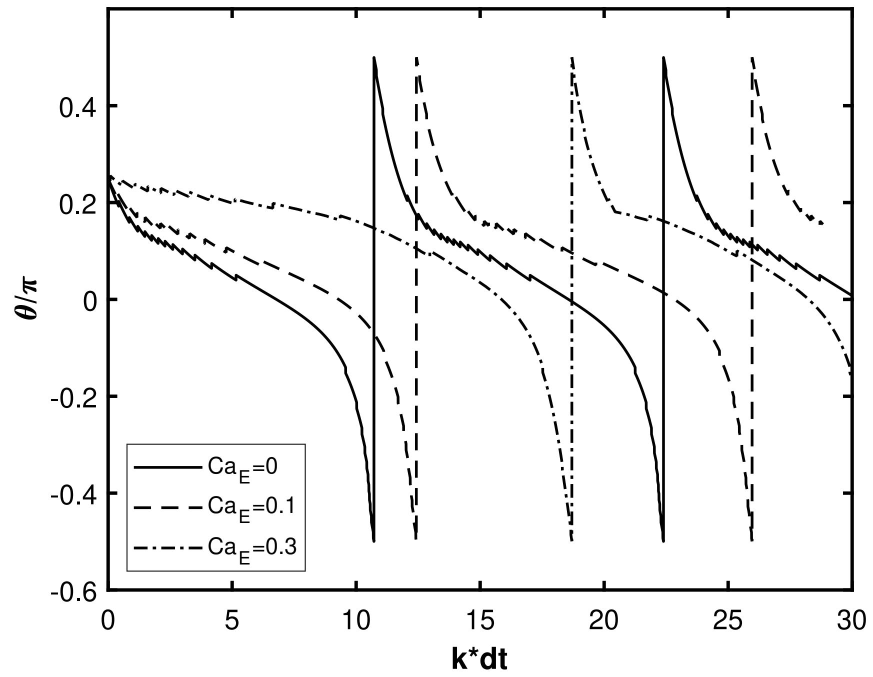

Figure. 88: Evolution of inclination angle of biconcave capsules with bending modulus $E_b = 0.005$ at $Ca = 0.0125$ for Case B ($\sigma_r = 3.25, \varepsilon_r = 3.5$).

5.4 EFFECT OF FLUID VISCOSITY RATIO ON THE DEFORMATION OF CAPSULE

In addition to membrane bending stiffness, the deformation of an elastic capsule is also determined by a few other factors such as inertia, membrane viscosity and the fluid viscosity ratio of internal and external fluids. In particular, when introduced to a simple linear shear flow, the elastic capsule exhibit a number of interesting physical dynamics, the nature of which is highly dependent on the ratio of the viscosity of the enclosed and external fluids. For large fluid viscosity contrasts or low shear rate, the non-spherical red blood cells undergo a tumbling motion which has been observed in experiments [59, 60, 61, 62]. For less deformed red blood cell or those with smaller viscosity contrasts, the capsules show a tank-treading motion characterized by a steady shape. Above phenomenon are also analytically [63, 64, 65, 66, 57, 56] and numerically studied [67, 68, 69, 70, 55].

Goldsmith and Marlow [71] were the first to experimentally observe the effect of viscosity ratio on red blood cells. Pfafferott [59] found that a red blood cell underwent tank-treading motion when the viscosity ratio was less than two, and tumbling motion for higher viscosity ratios when subjected to shear flow.

Keller and Skalak [63] theoretically analyzed the dynamic motion of an ellipsoidal capsule in simple shear flow. For a capsule with a given geometry, the transition from tank-treading mode to tumbling mode depends on the viscosity ratio between internal fluid and external fluid, and it is independent of shear rate. In Keller and Skalak's theory, the capsule was assumed to have a fixed shape. Rioual [64] predicted that viscosity ratio induced transition based on general considerations does not resort to the explicit computation of the full hydrodynamic field inside and outside the capsule.

Viscosity ratio dependent transition has also been recovered in numerical studies by Pozrikidis [41] using boundary element method, Misbah [54] and Beaucourt [55] using advected-field scheme and Salac & Miksis [69, 70] with level set methods.

The dimensionless fluid viscosity ratio V of a capsule is defined to be the ratio of the fluid viscosity inside the capsule μ_c, to the ambient fluid viscosity μ_a. To implement a non-unity fluid viscosity ratio over a time-dependent region, the fluid viscosity at each node is computed every timestep, so that the relaxation parameters for that node may be appropriately adjusted [72]. In practice, this is only necessary for nodes which are near the capsule boundary, as the others will not change from one timestep to the next. To compute the new viscosity at a node, not only whether the node lies inside or outside the capsule must be determined, but also the fluid viscosity contrast across the capsule interface must be smoothed, for the sake of the stability of the fluid solver. In the context of multiphase flows, Tryggvason et al. used a Poisson Equation to determine fluid density at grid points near the interface [73]. Alternatively, a Heaviside function [74] and hereafter refined in [3] based on the shortest normal distance from the fluid node to the membrane.

In current method, the strategy of [3] is employed to deal with the fluid viscosity jump across the capsule interface. To determine the viscosity of a fluid node at a given timestep, the Lagrangian node nearest to the fluid node is selected. The dot product of the vector between these two points and the unit outward normal from the Lagrangian node is calculated and the sign of this product indicate whether the fluid node is inside or outside of the capsule. The sign of d for a fluid node is set to be positive if the point is located outside of the interface or negative if it is inside the interface.

With the signed distance d having been determined, a smoothed Heaviside function of d from [3] is introduced, and defined as

$$H(d) = \begin{cases} 0, & d < -2h, \\ \frac{1}{2}(1 + \frac{d}{2h} + \frac{1}{\pi}\sin(\frac{\pi d}{2h})), & -2h \leq d \leq 2h \\ 1, & d > 2d \end{cases} \tag{153}$$

The viscosity μ at the node is determined using $H(d)$ by the equation

$$\mu(\mathbf{x}) = \mu_c + (\mu_a - \mu_c)H[d(\mathbf{x})] \tag{154}$$

in terms of the fluid viscosity μ_c inside the capsule and the ambient fluid viscosity μ_a.

The effect of fluid viscosity ratio on the deformation of circular capsules is investigated numerically in simple shear flow and DC electric field. Numerical simulations are performed in simple shear flow without applying DC electric field. The evolution of deformation for an elastic capsule at different capillary numbers under fluid viscosity ratio $V = 0.5$, $V = 1$ and $V = 5$ are plotted in

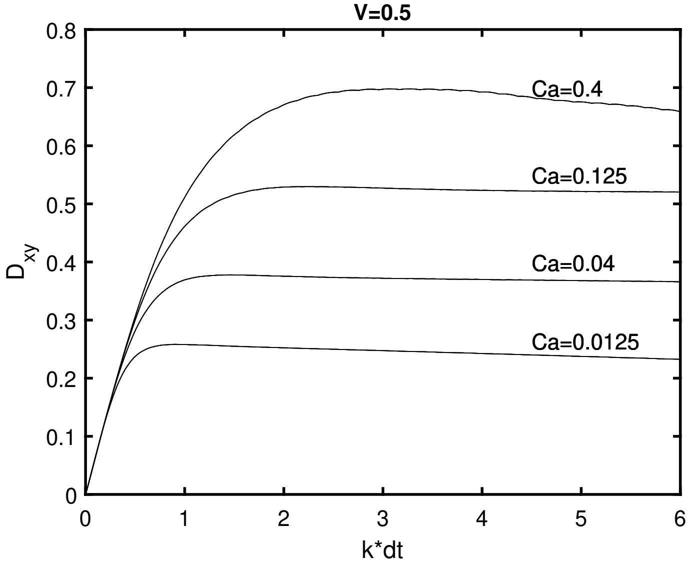

Figure. 89: Deformation of circular capsule for $V = 0.5$, $Re = 0.05$, $E_b = 0$ and $\eta = 0$.

Figure 89-91. We observe that the time required to achieve steady state increases with the fluid viscosity ratio, and also, the capsule with small viscosity ratio, is more deformed. The fluid viscosity ratio plays an opposite role to the shear rate. While subject to electric field (Figure 92), we observed the similar phenomenon without considering viscosity ratio. As the capillary number increases, the response time deformed to steady state decreases but the capsule deforms more. Comparing to electric field, fluid viscosity ratio plays more significant role in determining response time.

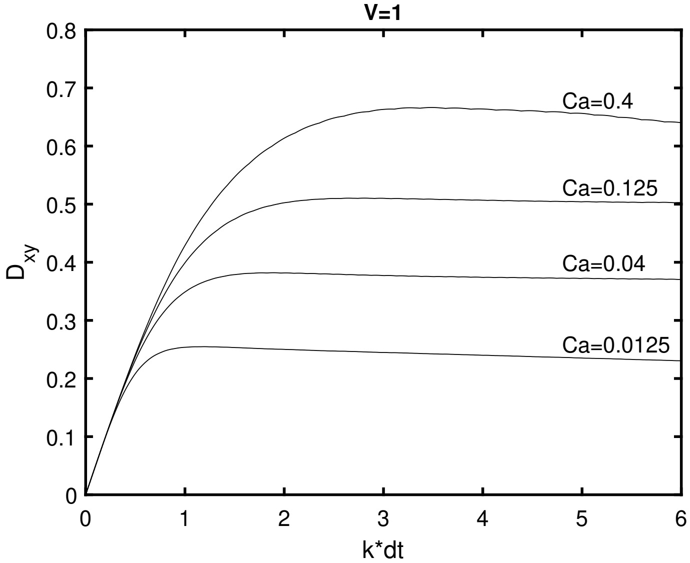

Figure. 90: Deformation of circular capsule for $V = 1$, $Re = 0.05$, $E_b = 0$ and $\eta = 0$.

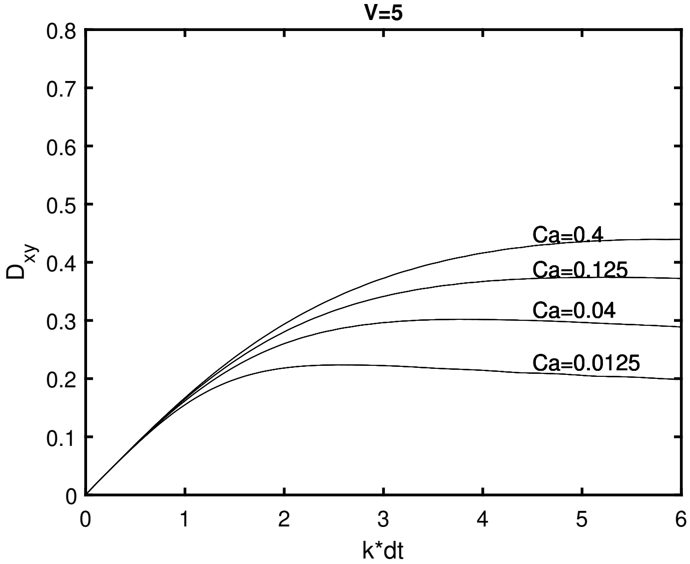

Figure. 91: Deformation of circular capsule for $V = 5$, $Re = 0.05$, $E_b = 0$ and $\eta = 0$.

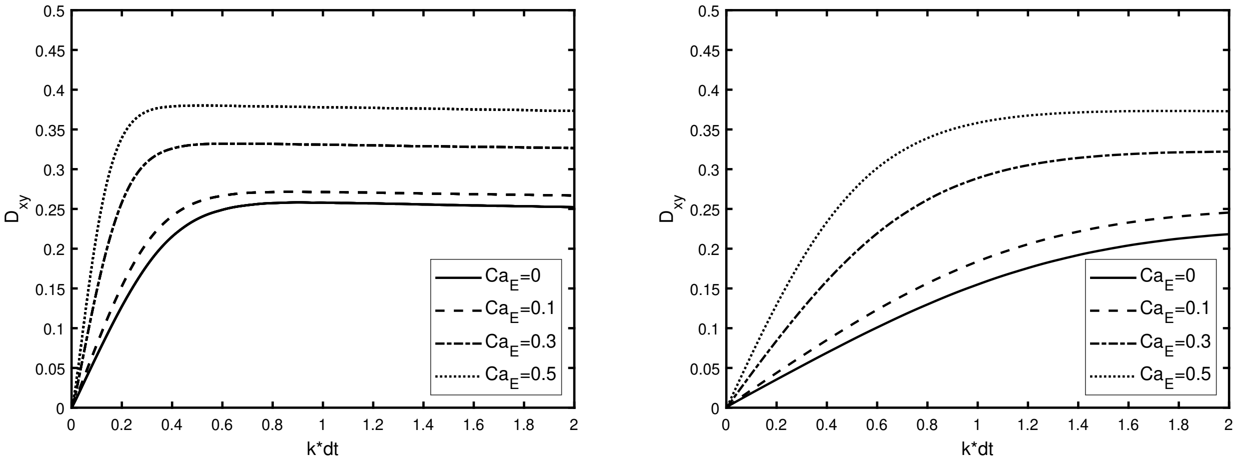

(a) $V = 0.5$, Case A: $\sigma_r = 1.75, \varepsilon_r = 3.5$.

(b) $V = 5$, Case A: $\sigma_r = 1.75, \varepsilon_r = 3.5$.

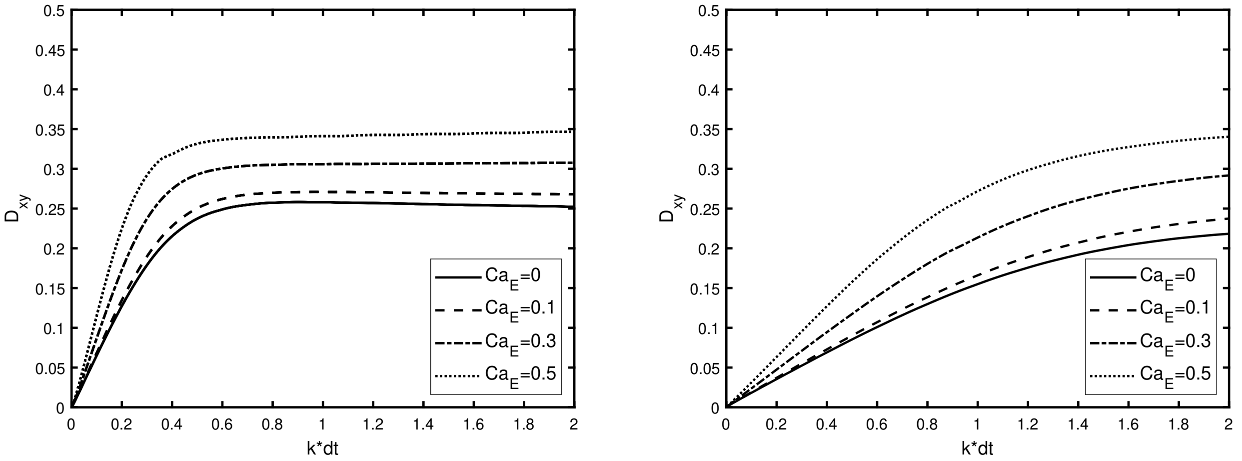

(c) $V = 0.5$, Case B: $\sigma_r = 3.25, \varepsilon_r = 3.5$.

(d) $V = 5$, Case B: $\sigma_r = 3.25, \varepsilon_r = 3.5$.

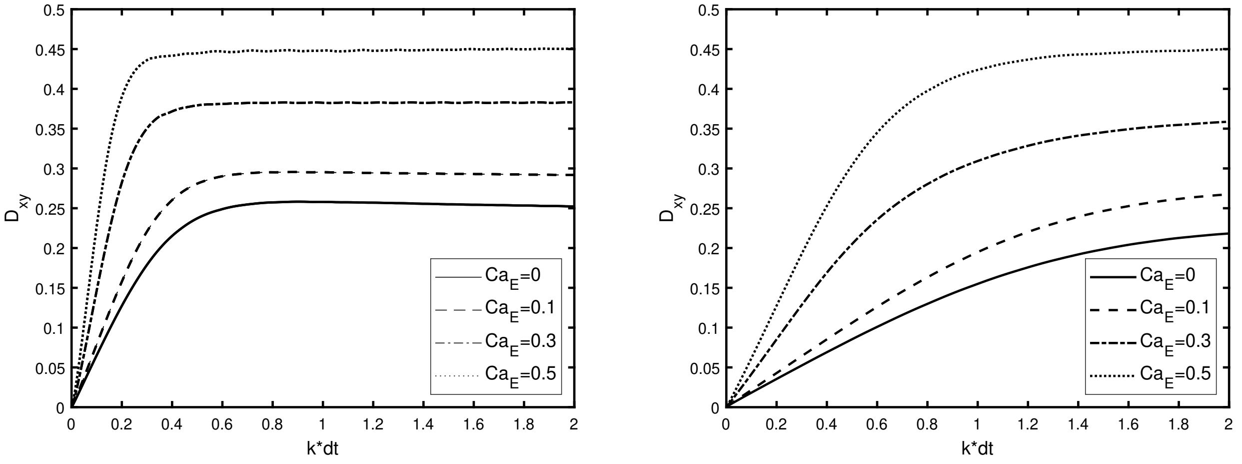

(e) $V = 0.5$, Case C: $\sigma_r = 4.75, \varepsilon_r = 3.5$.

(f) $V = 5$, Case C: $\sigma_r = 4.75, \varepsilon_r = 3.5$.

Figure. 92: Deformation parameters D_{xy} for $V = 0.5$ and $V = 5$ under shear flow $Ca = 0.0125$.

CHAPTER 6

THREE DIMENSIONAL SIMULATION

The hybrid immersed boundary method, lattice Boltzmann method and immersed interface method developed is used here to study the spherical capsule deformation in three dimensions. Although two-dimensional simulation represents some features of three dimensional study, it's still a large simplification and somehow miss a few other features. In the present simulation, a mesh with 2562 vertices and 5120 triangles is used.

A computational domain with size $[0,10] \times [0,10] \times [0,10]$ is selected, and an elastic spherical capsule of radius one is placed in the center of the computational domain, Neo-Hookean law is used. The internal and external fluids have the same property which indicates no viscosity jump cross the interface. Bending effect and membrane viscosity viscosity are not considered here. Reynolds number is set to be 0.05 and the inertia effect is negligible due to small Reynolds number.

Without electrical force, the simulation results at different capillary numbers ranging from 0.0125 to 0.2 are compared with Sui's results [42] in Figure 93, the results agree well. The shape evolution of cross section for $Ca = 0.025$ is depicted in Figure 97. The tank treading motion is observed. When capsule being deformed to equilibrium shape, the membrane rotates around internal liquid. The evolution of deformation parameter D_{xy} and tank-treading phenomenon confirm that 3D and 2D have similar common features. It takes longer to achieve equilibrium state for higher capillary number since the capsule needs to deform more to generate enough elastic force to balance the viscous shear force, which is considerably larger compared to elastic force for higher capillary number.

With electric field considered, similar results are obtained as in 2D simulations. We impose a constant voltage potential difference in z-direction by $\mathbf{E}_\infty = (0, 0, Ca_E(5-z))$, where Ca_E is dimensionless electric capillary number. The other boundary conditions for the potential ϕ are $\phi_{\partial x} = 0$ (Neumann) at $x = 0$ and $x = 10$, and $\phi_{\partial y} = 0$ (Neumann) at $y = 0$ and $y = 10$.

As stated in 2D simulation, under assumption of first-order small-deformation, the equilibrium steady shape of an elastic capsule is related to the discriminating function given by $f_d(\sigma_r, \varepsilon_r) =$

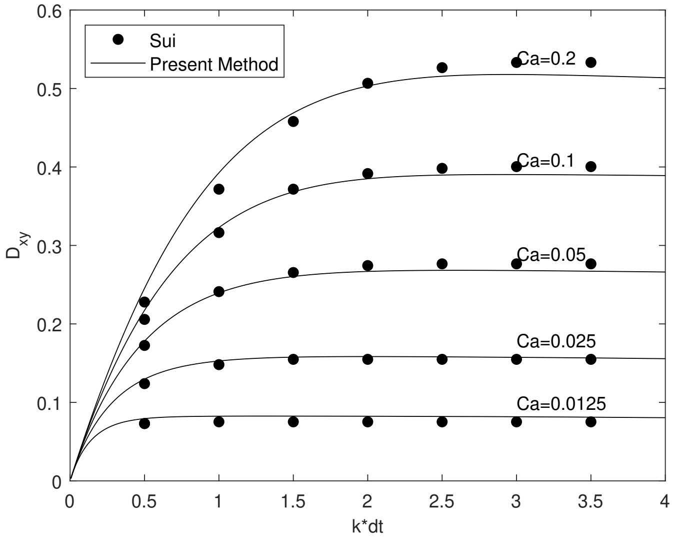

Figure. 93: Comparison for different capillary numbers Ca at $V = 1$, $E_b = 0$ and $\eta = 0$.

$\sigma_r^2 + \sigma_r + 1 - 3\varepsilon_r$. When $f_d < 0$, the capsule turns into an oblate shape; while $f_d > 0$, the capsule will deform into a prolate shape. The evolution of deformation parameters of the case with $\sigma_r = 1.75$ and $\varepsilon_r = 3.5$ is plotted in Figure 93 for a range of values of $Ca_E = 0, 0.1, 0.3, 0.5, 1$. It is seen the time taken to achieve steady shape is slightly shorter for higher electric capillary number Ca_E. Under stronger electric field, the capsule deforms to steady state quicker. The electric effect plays an significant role during the shape evolution. The tank treading motion for various strength electric field are depicted in Figure 97-101. For stronger electric field, the tank-treading motion is slightly slower. All above confirm the same features as in 2D simulation.

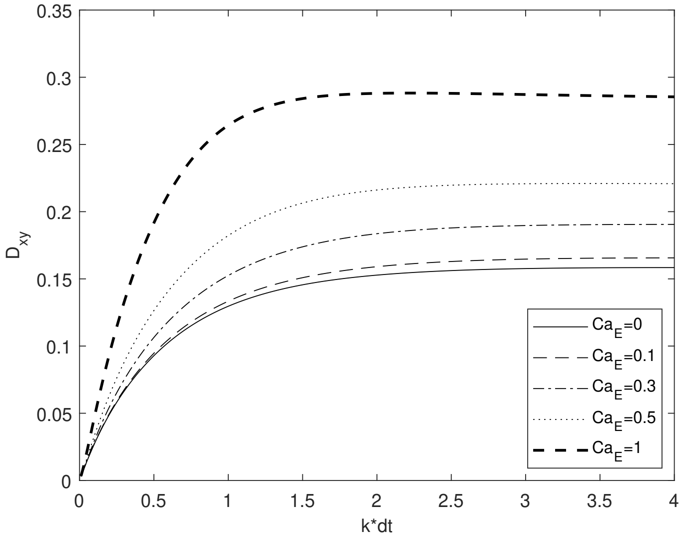

Figure. 94: Deformation for various electric strength with $Ca = 0.025$, $V = 1$ and $\eta = 0$. Case A: $\sigma_r = 1.75$, $\varepsilon_r = 3.5$.

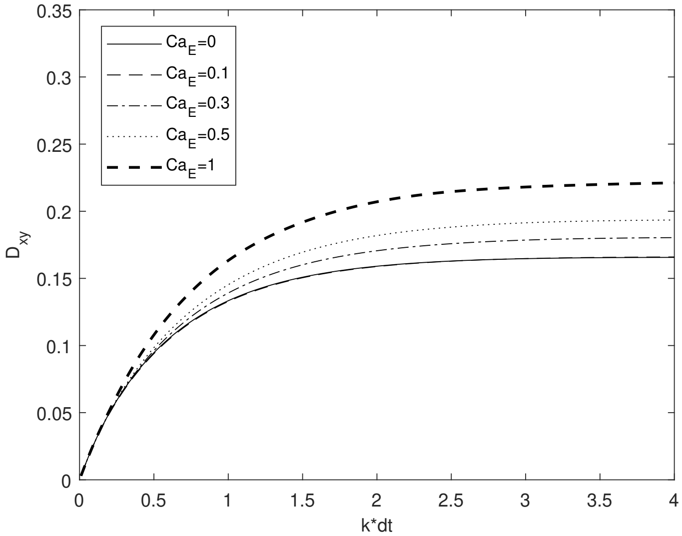

Figure. 95: Deformation for various electric strength with $Ca = 0.025$, $V = 1$ and $\eta = 0$. Case B: $\sigma_r = 3.25$, $\varepsilon_r = 3.5$.

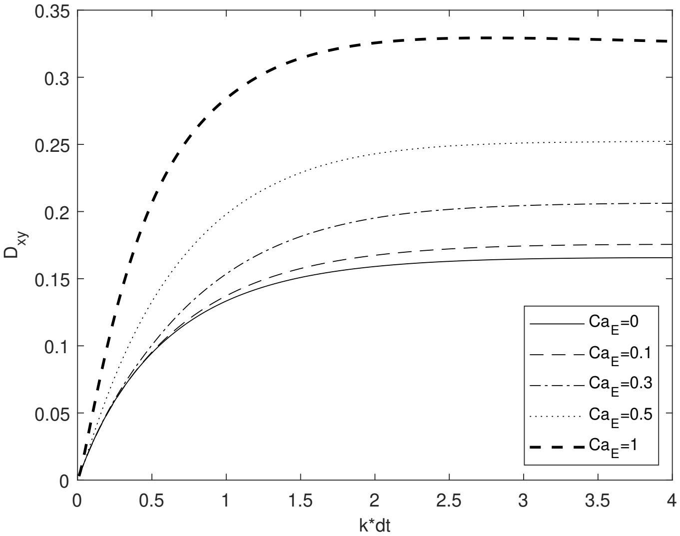

Figure. 96: Deformation for various electric strength with $Ca = 0.025$, $V = 1$ and $\eta = 0$. Case C: $\sigma_r = 4.75$, $\varepsilon_r = 3.5$.

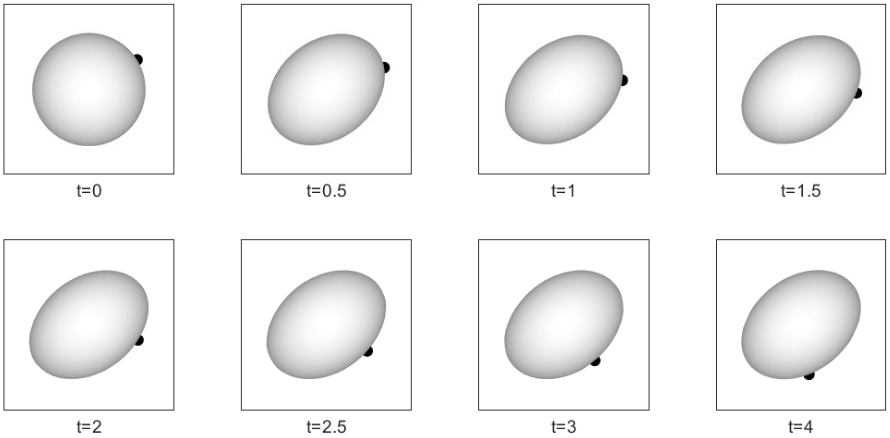

Figure. 97: Shape evolution for $Ca = 0.025$, $V = 1$ and $\eta = 0$.

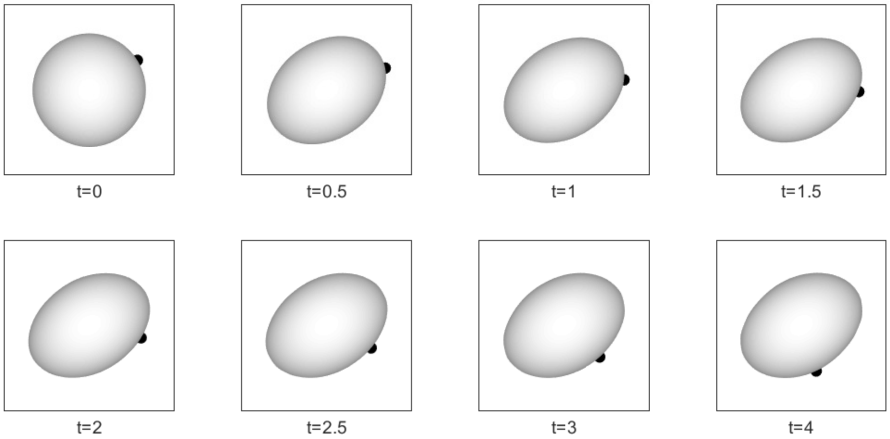

Figure. 98: Shape evolution for $Ca = 0.025$, $V = 1$ and $\eta = 0$, under electric field with strength $Ca_E = 0.1$. Case A: $\sigma_r = 1.75$, $\varepsilon_r = 3.5$.

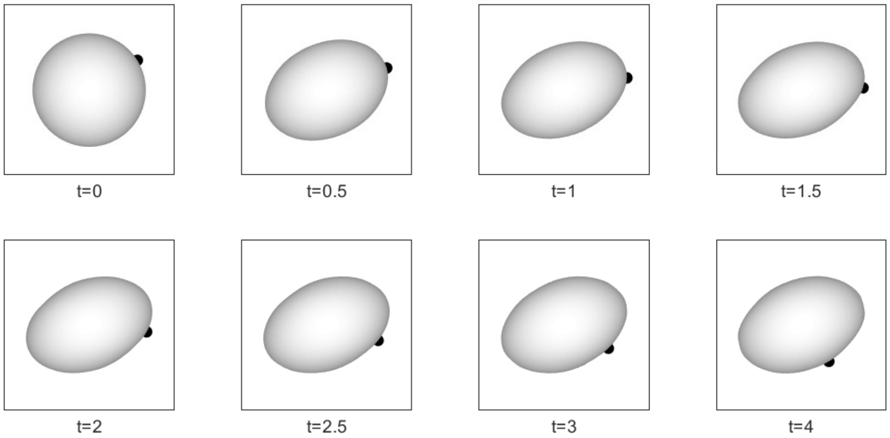

Figure. 99: Shape evolution for $Ca = 0.025$, $V = 1$ and $\eta = 0$, under electric field with strength $Ca_E = 0.3$. Case A: $\sigma_r = 1.75$, $\varepsilon_r = 3.5$.

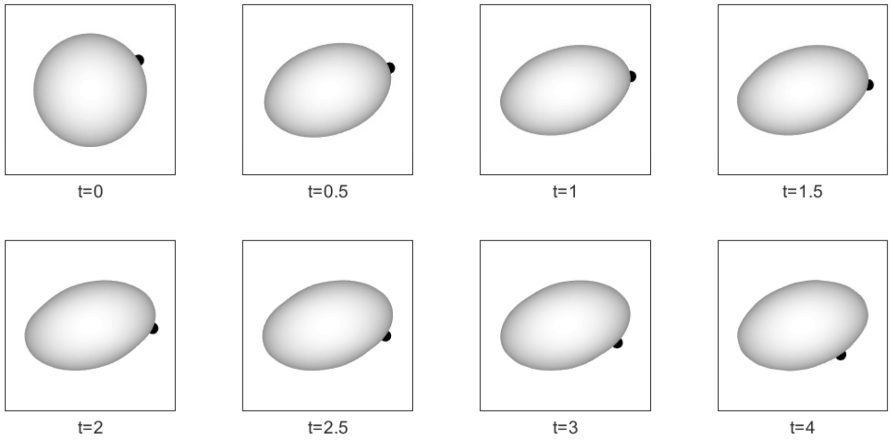

Figure. 100: Shape evolution for $Ca = 0.025$, $V = 1$ and $\eta = 0$, under electric field with strength $Ca_E = 0.5$. Case A: $\sigma_r = 1.75$, $\varepsilon_r = 3.5$.

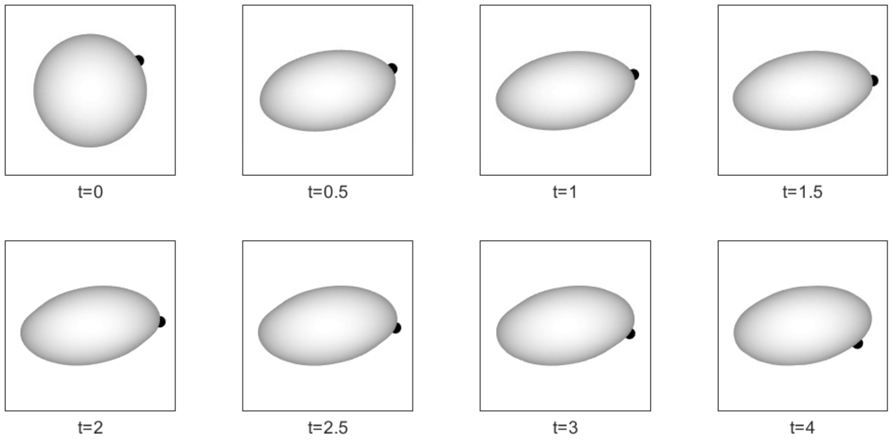

Figure. 101: Shape evolution for $Ca = 0.025$, $V = 1$ and $\eta = 0$, under electric field with strength $Ca_E = 1$. Case A: $\sigma_r = 1.75$, $\varepsilon_r = 3.5$.

CHAPTER 7

CONCLUSION

In this thesis, a hybrid method used to simulate electrohydrodynamics of the fluid-filled capsule under the shear flow with DC electric field is proposed. The lattice Boltzmann method combined with immersed boundary method is chosen to simulate the fluid-structure interaction. The electric field is solved by fast immersed interface method. The resulting electric stress tensor due to applied electric field is cast as an interfacial force in which the shear force and electric interfacial tension can be formulated in a unified immersed boundary framework. The present method also preserves the advantages of the immersed boundary method and lattice Boltzmann method.

A series of numerical tests for the present hybrid method were conducted to illustrate the accuracy and applicability of the method. Results were compared with Taylor's deformation theory and other numerical results in literature. In DC field, the circular capsules deform into ellipsoidal shapes and even drum-like shapes with high curvature edges under electric-induced flow. The initial transient behavior of deformation depends on the different properties between the inner and outer fluids of the capsule, the orientation of the capsules transitioning between prolate (major axis parallel to the applied electric field) or oblate (major axis perpendicular to applied electric field) shapes depending on the conductivity ratio and the permittivity ratio. The results agree well with published literature and show that the present numerical method could be an alternative approach for the simulation of electrohydrodynamics.

Based on present approach, the effect of electric effect on the deformation of two-dimensional viscoelastic capsule was investigated numerically in simple shear flow. The deformation of initially circular and biconcave shapes were studied. For circular capsule, when the membrane carries out tank-treading motion, the capsule shows larger deformation under electric effect. By increasing the strength of electric field, slower tank-treading phenomenon was observed. Bending suppress the deformation and the equilibrium capsule is less deformed if the bending stiffness is increased. For biconcave capsules, tumbling motion is obtained with relative high bending stiffness; the bending stiffness could be a factor that can lead to the transition of a capsule's motion from tank-treading to tumbling. When DC electric field is applied, the numerical results confirmed that be tumbling motion maybe dumped with relatively strong electric field. The damped phenomenon was observed for the case with $\sigma_r = 1.75, \varepsilon_r = 3.5$, though the tendency was noticed for the other two cases with different combination of conductivity ratio and permittivity ratio. Further improvement on numerical algorithm is undergoing in order to view the damped phenomenon for variety parameters.

Current algorithm is applicable for three dimensional computation. The membrane of three dimensional membrane was discretized into unstructured flat triangular elements and a finite element model was incorporated to obtain the forces acting on the membrane nodes. The present results agree well with published theoretical and numerical results. As expected, three-dimensional simulation showed some similar features as in two-dimensional simulation. The spherical capsule deform to stationary shapes and achieve steady tank-treading motion. Stronger electric field reduced tank treading frequency and enforced deformation parameter of the capsule.

Future work will consider vesicle membrane that is not only viscoelatic but also with an electric capacitance and an electric conductance within the leaky dielectric framework. The electric potential and transmembrane potential could be solved simultaneously based on present numerical method with sightly change on boundary conditions. The elliptic interface equation for the electric potential couples a time-varying transmembrane potential; the transmembrane potential is solved simultaneously with the electric potential.

REFERENCES

[1] A. Dondorp, B. Angus, K Chotivanich, K Silamut, R Ruangveerayuth, M. Hardeman, P. Kager, J Vreeken, and N. White, “Red blood cell deformability as a predictor of anemia in severe falciparum malaria.,” *The American journal of tropical medicine and hygiene*, vol. 60, no. 5, pp. 733–737, 1999.

[2] Z. Peng, X. Li, I. V. Pivkin, M. Dao, G. E. Karniadakis, and S. Suresh, “Lipid bilayer and cytoskeletal interactions in a red blood cell,” *Proceedings of the National Academy of Sciences*, vol. 110, no. 33, pp. 13 356–13 361, 2013.

[3] J. Zhang, P. C. Johnson, and A. S. Popel, “An immersed boundary lattice boltzmann approach to simulate deformable liquid capsules and its application to microscopic blood flows,” *Physical biology*, vol. 4, no. 4, p. 285, 2007.

[4] S. Usami, S. Chien, P. M. Scholtz, and J. F. Bertles, “Effect of deoxygenation on blood rheology in sickle cell disease,” *Microvascular research*, vol. 9, no. 3, pp. 324–334, 1975.

[5] T. M. Fischer, “Shape memory of human red blood cells,” *Biophysical journal*, vol. 86, no. 5, pp. 3304–3313, 2004.

[6] T. Secomb, T. Fischer, and R Skalak, “The motion of close-packed red blood cells in shear flow,” *Biorheology*, vol. 20, no. 3, pp. 283–294, 1983.

[7] R Skalak, A Tozeren, R. Zarda, and S Chien, “Strain energy function of red blood cell membranes,” *Biophysical Journal*, vol. 13, no. 3, pp. 245–264, 1973.

[8] N. Korin, A. Bransky, and U. Dinnar, “Theoretical model and experimental study of red blood cell (rbc) deformation in microchannels,” *Journal of biomechanics*, vol. 40, no. 9, pp. 2088–2095, 2007.

[9] G. Tomaiuolo, M. Simeone, V. Martinelli, B. Rotoli, and S. Guido, “Red blood cell deformation in microconfined flow,” *Soft Matter*, vol. 5, no. 19, pp. 3736–3740, 2009.

[10] G. Tomaiuolo, M. Barra, V. Preziosi, A. Cassinese, B. Rotoli, and S. Guido, “Microfluidics analysis of red blood cell membrane viscoelasticity,” *Lab on a Chip*, vol. 11, no. 3, pp. 449–454, 2011.

[11] J. Zhang, P. C. Johnson, and A. S. Popel, “Red blood cell aggregation and dissociation in shear flows simulated by lattice boltzmann method,” *Journal of biomechanics*, vol. 41, no. 1, pp. 47–55, 2008.

[12] M. M. Dupin, I. Halliday, C. M. Care, L. Alboul, and L. L. Munn, “Modeling the flow of dense suspensions of deformable particles in three dimensions,” *Physical Review E*, vol. 75, no. 6, p. 066 707, 2007.

[13] G. I. Taylor, “Studies in electrohydrodynamics. i. the circulation produced in a drop by an electric field,” *Proc. R. Soc. Lond. A*, vol. 291, no. 1425, pp. 159–166, 1966.

[14] J.-W. Ha and S.-M. Yang, “Electrohydrodynamic effects on the deformation and orientation of a liquid capsule in a linear flow,” *Physics of Fluids*, vol. 12, no. 7, pp. 1671–1684, 2000.

[15] J. Hua, L. K. Lim, and C.-H. Wang, “Numerical simulation of deformation/motion of a drop suspended in viscous liquids under influence of steady electric fields,” *Physics of Fluids*, vol. 20, no. 11, p. 113 302, 2008.

[16] E. Bjørklund, “The level-set method applied to droplet dynamics in the presence of an electric field,” *Computers & Fluids*, vol. 38, no. 2, pp. 358–369, 2009.

[17] K. E. Teigen and S. T. Munkejord, “Influence of surfactant on drop deformation in an electric field,” *Physics of Fluids*, vol. 22, no. 11, p. 112 104, 2010.

[18] J. Zhang and D. Y. Kwok, “A 2d lattice boltzmann study on electrohydrodynamic drop deformation with the leaky dielectric theory,” *Journal of Computational Physics*, vol. 206, no. 1, pp. 150–161, 2005.

[19] G. Tomar, D. Gerlach, G. Biswas, N. Alleborn, A. Sharma, F. Durst, S. W. Welch, and A. Delgado, “Two-phase electrohydrodynamic simulations using a volume-of-fluid approach,” *Journal of Computational Physics*, vol. 227, no. 2, pp. 1267–1285, 2007.

[20] W.-F. Hu, M.-C. Lai, and Y.-N. Young, “A hybrid immersed boundary and immersed interface method for electrohydrodynamic simulations,” *Journal of Computational Physics*, vol. 282, pp. 47–61, 2015.

[21] A. N. Marques, J.-C. Nave, and R. R. Rosales, “A correction function method for poisson problems with interface jump conditions,” *Journal of Computational Physics*, vol. 230, no. 20, pp. 7567–7597, 2011.

[22] Z. Li, K. Ito, and M.-C. Lai, “An augmented approach for stokes equations with a discontinuous viscosity and singular forces,” *Computers & Fluids*, vol. 36, no. 3, pp. 622–635, 2007.

[23] S. Xu, “An iterative two-fluid pressure solver based on the immersed interface method,” *Communications in Computational Physics*, vol. 12, no. 2, pp. 528–543, 2012.

[24] R. J. Leveque and Z. Li, “The immersed interface method for elliptic equations with discontinuous coefficients and singular sources,” *SIAM Journal on Numerical Analysis*, vol. 31, no. 4, pp. 1019–1044, 1994.

[25] Z. Li, “The immersed interface method: A numerical approach for partial differential equations with interfaces,” PhD thesis, 1994.

[26] ——, “A fast iterative algorithm for elliptic interface problems,” *SIAM Journal on Numerical Analysis*, vol. 35, no. 1, pp. 230–254, 1998.

[27] Y. Saad and M. H. Schultz, “Gmres: A generalized minimal residual algorithm for solving nonsymmetric linear systems,” *SIAM Journal on scientific and statistical computing*, vol. 7, no. 3, pp. 856–869, 1986.

[28] C. C. Paige and M. A. Saunders, “Solution of sparse indefinite systems of linear equations,” *SIAM journal on numerical analysis*, vol. 12, no. 4, pp. 617–629, 1975.

[29] P. Pulay, “Convergence acceleration of iterative sequences. the case of scf iteration,” *Chemical Physics Letters*, vol. 73, no. 2, pp. 393–398, 1980.

[30] W. E. Arnoldi, “The principle of minimized iterations in the solution of the matrix eigenvalue problem,” *Quarterly of applied mathematics*, vol. 9, no. 1, pp. 17–29, 1951.

[31] C. S. Peskin, “Numerical analysis of blood flow in the heart,” *Journal of computational physics*, vol. 25, no. 3, pp. 220–252, 1977.

[32] S. Deng, K. Ito, and Z. Li, “Three-dimensional elliptic solvers for interface problems and applications,” *Journal of Computational Physics*, vol. 184, no. 1, pp. 215–243, 2003.

[33] X.-D. Liu, R. P. Fedkiw, and M. Kang, “A boundary condition capturing method for poisson’s equation on irregular domains,” *Journal of computational Physics*, vol. 160, no. 1, pp. 151–178, 2000.

[34] P. Lallemand and L.-S. Luo, “Theory of the lattice boltzmann method: Dispersion, dissipation, isotropy, galilean invariance, and stability,” *Physical Review E*, vol. 61, no. 6, p. 6546, 2000.

[35] Y. Peng and L.-S. Luo, “A comparative study of immersed-boundary and interpolated bounce-back methods in lbe,” *Progress in Computational Fluid Dynamics, an International Journal*, vol. 8, no. 1-4, pp. 156–167, 2008.

[36] D. d’Humières, “Multiple–relaxation–time lattice boltzmann models in three dimensions,” *Philosophical Transactions of the Royal Society of London A: Mathematical, Physical and Engineering Sciences*, vol. 360, no. 1792, pp. 437–451, 2002.

[37] P. Lallemand and L.-S. Luo, “Theory of the lattice boltzmann method: Acoustic and thermal properties in two and three dimensions,” *Physical review E*, vol. 68, no. 3, p. 036 706, 2003.

[38] P. Lallemand, L.-S. Luo, and Y. Peng, “A lattice boltzmann front-tracking method for interface dynamics with surface tension in two dimensions,” *Journal of Computational Physics*, vol. 226, no. 2, pp. 1367–1384, 2007.

[39] E. A. Evans, “Bending elastic modulus of red blood cell membrane derived from buckling instability in micropipet aspiration tests,” *Biophysical Journal*, vol. 43, no. 1, pp. 27–30, 1983.

[40] E. Evans and R. Hochmuth, “Membrane viscoelasticity,” *Biophysical Journal*, vol. 16, no. 1, pp. 1–11, 1976.

[41] C Pozrikidis, “Numerical simulation of the flow-induced deformation of red blood cells,” *Annals of biomedical engineering*, vol. 31, no. 10, pp. 1194–1205, 2003.

[42] Y Sui, Y. Chew, P Roy, X. Chen, and H. Low, “Transient deformation of elastic capsules in shear flow: Effect of membrane bending stiffness,” *Physical Review E*, vol. 75, no. 6, p. 066 301, 2007.

[43] S Ramanujan and C Pozrikidis, “Deformation of liquid capsules enclosed by elastic membranes in simple shear flow: Large deformations and the effect of fluid viscosities,” *Journal of Fluid Mechanics*, vol. 361, pp. 117–143, 1998.

[44] A. Z. Yazdani and P. Bagchi, “Phase diagram and breathing dynamics of a single red blood cell and a biconcave capsule in dilute shear flow,” *Physical Review E*, vol. 84, no. 2, p. 026 314, 2011.

[45] O.-Y. Zhong-Can and W. Helfrich, “Bending energy of vesicle membranes: General expressions for the first, second, and third variation of the shape energy and applications to spheres and cylinders,” *Physical Review A*, vol. 39, no. 10, p. 5280, 1989.

[46] J. Melcher and G. Taylor, “Electrohydrodynamics: A review of the role of interfacial shear stresses,” *Annual review of fluid mechanics*, vol. 1, no. 1, pp. 111–146, 1969.

[47] D. Saville, “Electrohydrodynamics: The taylor-melcher leaky dielectric model,” *Annual review of fluid mechanics*, vol. 29, no. 1, pp. 27–64, 1997.

[48] G Breyiannis and C Pozrikidis, “Simple shear flow of suspensions of elastic capsules,” *Theoretical and Computational Fluid Dynamics*, vol. 13, no. 5, pp. 327–347, 2000.

[49] J. Q. Feng, “A 2d electrohydrodynamic model for electrorotation of fluid drops,” *Journal of colloid and interface science*, vol. 246, no. 1, pp. 112–121, 2002.

[50] S. J. Choi and W. Schowalter, “Rheological properties of nondilute suspensions of deformable particles,” *The Physics of Fluids*, vol. 18, no. 4, pp. 420–427, 1975.

[51] A. Walter, H. Rehage, and H. Leonhard, “Shear induced deformation of microcapsules: Shape oscillations and membrane folding,” *Colloids and Surfaces A: Physicochemical and Engineering Aspects*, vol. 183, pp. 123–132, 2001.

[52] I. Koleva and H. Rehage, “Deformation and orientation dynamics of polysiloxane microcapsules in linear shear flow,” *Soft Matter*, vol. 8, no. 13, pp. 3681–3693, 2012.

[53] H. Zhou and C Pozrikidis, “Deformation of liquid capsules with incompressible interfaces in simple shear flow,” *Journal of Fluid Mechanics*, vol. 283, pp. 175–200, 1995.

[54] T Biben and C Misbah, “Tumbling of vesicles under shear flow within an advected-field approach,” *Physical Review E*, vol. 67, no. 3, p. 031 908, 2003.

[55] J Beaucourt, F Rioual, T Séon, T Biben, and C Misbah, “Steady to unsteady dynamics of a vesicle in a flow,” *Physical Review E*, vol. 69, no. 1, p. 011 906, 2004.

[56] J. Skotheim and T. W. Secomb, “Red blood cells and other nonspherical capsules in shear flow: Oscillatory dynamics and the tank-treading-to-tumbling transition,” *Physical review letters*, vol. 98, no. 7, p. 078 301, 2007.

[57] J. T. Schwalbe, P. M. Vlahovska, and M. J. Miksis, “Lipid membrane instability driven by capacitive charging,” *Physics of Fluids*, vol. 23, no. 4, p. 041 701, 2011.

[58] L. C. McConnell, M. J. Miksis, and P. M. Vlahovska, “Vesicle electrohydrodynamics in dc electric fields,” *IMA Journal of Applied Mathematics*, vol. 78, no. 4, pp. 797–817, 2013.

[59] C. Pfafferott, G. B. Nash, and H. J. Meiselman, “Red blood cell deformation in shear flow. effects of internal and external phase viscosity and of in vivo aging,” *Biophysical journal*, vol. 47, no. 5, pp. 695–704, 1985.

[60] M. Abkarian, M. Faivre, and A. Viallat, “Swinging of red blood cells under shear flow,” *Physical review letters*, vol. 98, no. 18, p. 188 302, 2007.

[61] V. Kantsler and V. Steinberg, “Orientation and dynamics of a vesicle in tank-treading motion in shear flow,” *Physical review letters*, vol. 95, no. 25, p. 258 101, 2005.

[62] M.-A. Mader, V Vitkova, M Abkarian, A Viallat, and T Podgorski, “Dynamics of viscous vesicles in shear flow,” *The European Physical Journal E*, vol. 19, no. 4, pp. 389–397, 2006.

[63] S. R. Keller and R. Skalak, “Motion of a tank-treading ellipsoidal particle in a shear flow,” *Journal of Fluid Mechanics*, vol. 120, pp. 27–47, 1982.

[64] F Rioual, T Biben, and C Misbah, “Analytical analysis of a vesicle tumbling under a shear flow,” *Physical Review E*, vol. 69, no. 6, p. 061 914, 2004.

[65] V. Lebedev, K. Turitsyn, and S. Vergeles, “Nearly spherical vesicles in an external flow,” *New journal of Physics*, vol. 10, no. 4, p. 043 044, 2008.

[66] C. Misbah, “Vacillating breathing and tumbling of vesicles under shear flow,” *Physical review letters*, vol. 96, no. 2, p. 028 104, 2006.

[67] A. Rahimian, S. K. Veerapaneni, and G. Biros, “Dynamic simulation of locally inextensible vesicles suspended in an arbitrary two-dimensional domain, a boundary integral method,” *Journal of Computational Physics*, vol. 229, no. 18, pp. 6466–6484, 2010.

[68] M. Zhao, “Electrical fields in wound healing—an overriding signal that directs cell migration,” in *Seminars in cell & developmental biology*, Elsevier, vol. 20, 2009, pp. 674–682.

[69] D. Salac and M Miksis, “A level set projection model of lipid vesicles in general flows,” *Journal of Computational Physics*, vol. 230, no. 22, pp. 8192–8215, 2011.

[70] D. Salac and M. J. Miksis, “Reynolds number effects on lipid vesicles,” *Journal of Fluid Mechanics*, vol. 711, pp. 122–146, 2012.

[71] H. Goldsmith, J. Marlow, and F. C. MacIntosh, “Flow behaviour of erythrocytes-i. rotation and deformation in dilute suspensions,” *Proceedings of the Royal Society of London. Series B. Biological Sciences*, vol. 182, no. 1068, pp. 351–384, 1972.

[72] J. Gounley and Y. Peng, “Shape recovery of elastic capsules from shear flow induced deformation,” *Communications in Computational Physics*, vol. 16, no. 1, pp. 56–74, 2014.

[73] G. Tryggvason, B. Bunner, A. Esmaeeli, D. Juric, N Al-Rawahi, W Tauber, J Han, S Nas, and Y.-J. Jan, “A front-tracking method for the computations of multiphase flow,” *Journal of computational physics*, vol. 169, no. 2, pp. 708–759, 2001.

[74] N. N’dri, W Shyy, and R Tran-Son-Tay, “Computational modeling of cell adhesion and movement using a continuum-kinetics approach,” *Biophysical journal*, vol. 85, no. 4, pp. 2273–2286, 2003.

VITA

Pai Song
Department of Computational and Applied Mathematics
Old Dominion University
Norfolk, VA 23529

PREVIOUS DEGREES

M.A. Mathematics, Marshall University, Huntington, WV. (2011)

B.E. Aeronautical Engineering, Beihang University, China. (2006)

PUBLICATIONS

Weidong Li, Wei Li, Pai Song and Hao Ji. *A conservation moments based implicit finite volume lattice Boltzmann method for steady nearly incompressible fows*. Journal of Computational Physics, Available online 9 August 2019, 108882

Iordanka N. Panayotova, Pai Song and John P. Mchugh. *Spatial Stability of Horizontally Sheared Flow*. Special Issue 2013 of the Journal Discrete and Continuous Dynamical Systems (2013): 611 - 618.

Typeset using LaTeX.